2013

Role of contamination on the bondline integrity of composite structures

Xu Shang
Iowa State University

Role of contamination on the bondline integrity of composite structures

by

Xu Shang

A dissertation submitted to the graduate faculty

in partial fulfillment of the requirements for the degree of

DOCTOR OF PHILOSOPHY

Major: Engineering Mechanics

Program of Study Committee:

Ashraf F. Bastawros, Major Professor
Wei Hong
Thomas J. Rudolphi
Pranav Shrotriya
Stephen Holland

Iowa State University

Ames, Iowa

2013

TABLE OF CONTENTS

LIST OF FIGURES

LIST OF TABLES

ACKNOWLEDGEMENTS

This work has been conducted under support from Navair-ONR contract No.104728. The forensic work in Appendix is supported by [National Institute of Justices, contract No. 2011-DN-R-0230] through the U.S. Department of Energy under Contract No. DE-AC02-07CH11358.

First of all, I would like to express my sincere and most gratitude to my major professor, Dr. Ashraf Bastawros, for his patience and intelligence. Through my whole graduate studies, I have learned both academic and practical knowledge from him. The first day I came into graduate study, I was encouraged by his diligent and rigorous attitude. Throughout my whole graduate life, I was guided by him with his wisdom and distinctive perception. He helped me in revising this dissertation with great patience and encouragement. I want to thank him for all his supports and advices.

I would like to thank my committee members for their efforts and contributions to this work: Dr. Wei Hong, Dr. Thomas J. Rudolphi, Dr. Pranav Shrotriya, Dr. Abhijit Chandra and Dr. Stephen Holland. They provide me inspiration and guidance when I discuss with them.

Dr. Hui Wang helped me a lot both on experiments and programming when I first start my work. I want to thank her and wish her happy. Dr. Peter Sherman gave his deep insights on the forensic project. I would like to thank him for his collaboration. Dr. Barbara

Lograsso who provides her invaluable idea and advice on the forensic project is much appreciated.

ABSTRACT

Adhesively bonding composite structures have many applications in aerospace, automotive and submarine industries. The adhesive bonding joints have substantial advantage over the traditional metallic mechanical bonding joints, such as rivet and welding. However, the adhesive bonding joints require additional steps of surface preparation and cleaning to ensure consistent bond strength. In application, the adhesively bonded joints are exposed to environmental degradation and industrial solvent contaminates. Accordingly, the assurance of reliability of bonded composite structures requires detailed investigation of the role of contaminates on bondline integrity.

This dissertation focuses on assessing the contaminates effect on the adhesive bondline integrity. A combined experimental and numerical framework is developed to study the contamination effect on the adhesive mechanical properties and adhesive joint strength. The bondline integrity were examined for a system of adhesive (EA9394) and the carbon-fiber system (Hexply IM7/8552), after being subjected to different level of exposures to aviation hydraulic fluids and mold cleaning agents. A testing protocol based on nanoindentation for initial screening is used to predict the interfacial fracture characteristics after exposure to contamination. It is found the adhesive modulus and stiffness dropped by up to 10% for the hydraulic fluid contaminates, suggesting increase of the plastic dissipation within the bondline. However, the trend for the cleaning agent was not clear since the modulus drop while its hardness increased.

Detailed measurements of interfacial fracture toughness are carried out via standard tests of double cantilever beam specimens, exposed to varying level of contamination. The tests were carried out in a computer controlled Instron universal testing frame. An optical based crack propagation measurement technique is developed to in situ monitor the crack extensions with 5μm resolution. It is found that even at the trace level of 3 $\mu g/cm^2$, the interfacial fracture toughness is reduced by more than 35%. The surface topography of the fractured interfaces is further examined by surface profilometer. A clear transition from very rough fractured surface with fiber/matrix pull out, to very smooth fractured surface with interface failure is observed with the increased level of contamination. This transition of fracture surface topography testified the proposed cohesive model.

Finite element analysis with cohesive zone model is used to rationalize the experimental results and understanding the mechanism of contamination degradation. Double cantilever beam model with various adhesive bonding parameters were tested. The interfacial cohesive parameters, the adhesive properties and the thickness of the adhesive layer were examined. The results show the parameters effect on the process zone propagation and the adhesive bonding toughness. The relation of process zone size and the bondline parameters were examined and compared with the existing double cantilever beam results. The finite element work showed that the contamination-induced degradation of the interfacial adhesion strength is the primary effect in mode I fracture.

To fully understand the contaminations effect on adhesively bonded joints, mode II fracture test is conduced. Single shear lap test shows the contaminations has softening effect

could strengthen the adhesive bonding initiation force. Further simulation work shows the detailed process zone propagation. It is shown that the contaminates effect on the adhesive matrix hardness becomes the primary effect for the adhesive debonding.

CHAPTER 1 INTRODUCTION

1.1 Background: Adhesive Bonding of Composite Structures

1.1.1 Adhesive Bonding of Composite Structures

In the last 4-decades, fiber reinforced polymer composite structures have been wildly used for primary and secondary structures in both commercial and military aircrafts, because they can offer substantial advantages over traditional metallic structures. These benefits lead to improve performance, significant weight reduction, and reduced manufacturing and maintenance costs (Cantor, 2005). Adhesive bonding is the preferred joining method for composite structures to reduce machining induced defects and localized contact stress arising in riveted or bolted assembly. The adhesively bonded joints can offer excellent fatigue strength, good sealing and excellent performance in high temperature (Banea, 2009). Adhesively bonded joints are comprised of adhesive-adherend pair. The proper adherend surface treatment is critical to ensure reliability of the adhesive joints. The interface of the bonded joint has been considered as the weak point for adhesively bonded composite structures. Around 70% of the adhesively bonded structure failures were reported to initiate at the bondline (Her, 1999; Abdul Razar, 2011). It is essential to have a fundamental understanding of the interaction between each of the components of adhesively bonded joints and the response to the history of applied load and the role of environmental degradation. These correlations are unique to adhesive-adherend pair. To ensure in-service composite structure reliability, it is essential to study these correlations and the role of environmental exposure.

1.1.2 Type of Adhesive Joints Failure Mode

The adhesively bonded joints typically fail in one of three different modes. Figure 1.1 shows the three failure modes, i.e. substrate, cohesive and interfacial failure. In practice, the failure of adhesive bonding may have a combination of these three modes of failures. Stress driven or energy driven failure criteria have been proposed for each failure mode. For example, the substrate failure is a typical failure for interlaminar shear or peel stress with weak composite adherend. A simple maximum stress theory was proposed by Adams (1984). The failure in the composite adherend is assumed to occur when the normal tensile stress reaches the ultimate strength. This theory regards the interfacial peel stress as the major driving force to the failure. Other focused on the substrate failure mechanisms with different layup orientation (Hoyt, 2000; Tong, 1997). For adhesively bonded joints, interfacial failure is more prevalent. Several phenomenological models were proposed to describe the crack growth of interfacial failure (Suo, 1993; Tvergaard, 1994; Jacobsen et al, 1998). It remains a fact that interfacial failure is more complex due to the concurrent interfacial and substrate failure (i.e. local fiber pull out from the substrate).

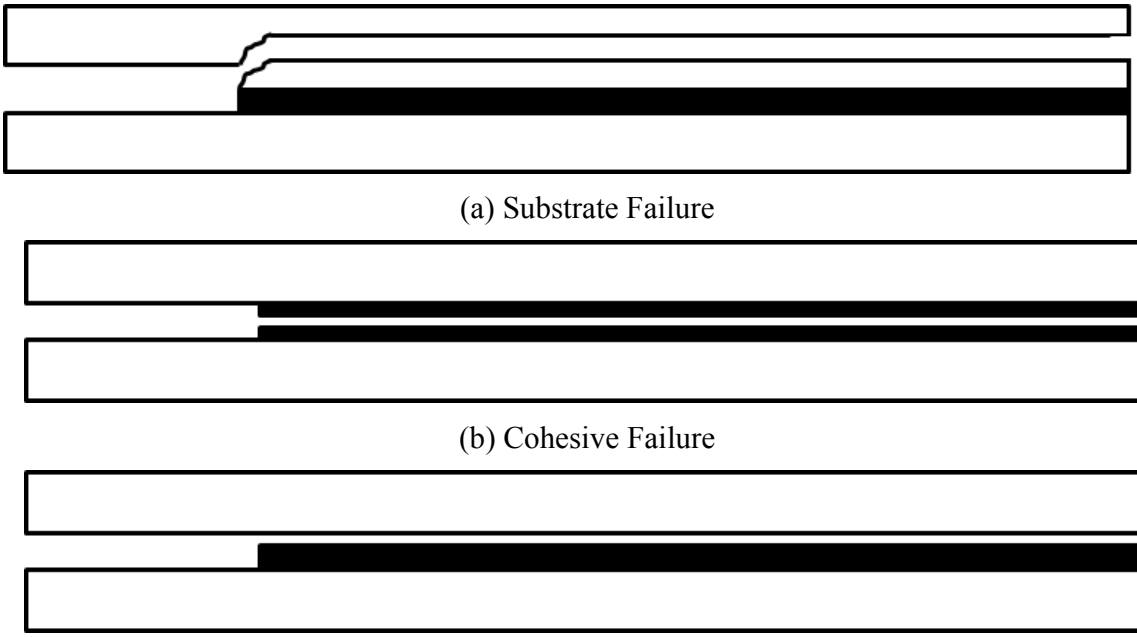

(a) Substrate Failure

(b) Cohesive Failure

(c) Interfacial Failure

Figure 1.1 Failure modes of adhesively bonded joints.

1.1.3 Contaminates and Surface Treatments

The adhesively bonded joints degradation has been studied extensively by brute-force testing under many service environments, including (i) service temperature (Ashcroft et al, 2001; Kalarikkal et al, 2006), (ii) moisture (Banea et al, 2009; Zhang et al, 1999), (iii) loading history (i.e. amplitude and frequency of dynamic loads), (iii) thermal cycling (Mandil et al, 1990; Lee et al, 1996), (iv) exposure to contaminates (Pribanic et al, 2013), and (v) exposure to radiation (Paulauskas et al, 1996). The complex interplay between these factors may result in accelerated or delayed failure of the bondline. The challenge remains in detecting the interfacial progressive damage of bonded structures, and the associated weakening of interfacial fracture toughness, which may lead to catastrophic failure. For example, the interface between the matrix and fibers can be weakened by moisture and

temperature (Kinloch, 1983). But the degradation rates are different for different composite system. This means that the failure mechanism of adhesive bonded joints degradation depends on the composite system, which is quite different from the well-studied cases like metal deterioration. There is a lack in both experimental and theoretical study on the contaminations degradation of the adhesively bonded composite structure.

Surface treatment is another complex and important issue for the adhesively bonded joints. For general composite, the molded surface is smooth, and the surface energy is low, which result to weak bonding with adhesives. Contaminates as discussed above is another damaging factor, which could lower the surface energy. For example, release agents, service fluids, fingerprints etc. may result in a weaker interfacial strength. Appropriate surface treatment and cleaning are required before adhesive bonding to modify the chemical properties or topography of the surface layer. The surface treatments can be categorized into three types, mechanical, chemical and energetic treatments (Wingfield, 1993). A wide range of chemical, mechanical, energetic surface treatments have been studied since the application of composite materials in industry (Kinloch, 1991; Parker, 1982). The effectiveness of surface treatment also depends on the composite material system. For example, some solvent could remove a specific type of contaminates or change the surface energy for specific type of bulk composite materials. Plasma treatment may result in temperature rise and cause particular composite surface topography change. A proper selection of surface treatment is of vital to the reliability of the adhesive bonding composite structures. One of the most common surface treatments for adhesively bonded composite structure is sand blasting. The purpose of sandblasting is to modify the roughness of the surface. The roughness introduced can

change the failure type from interfacial failure to substrate failure, which leads to improvement of the bondline toughness. However, it was reported that utilization of sandblasting to roughen the composite panel may result in matrix damage caused by sandblasting (Mittal, 1976; Ramanujam, 2007). As discussed above, the proper selection of the parameters in surface treatment is dependent on the specific composite system. There is no universal standard of surface treatment for general composite systems.

1.2 Scope of Work

The bondline is the most common place of failure initiation and need to be studied with great effort. As mentioned above, some researches have shown the composite system dependency. Moreover, the effect of contaminates on the adhesive bondline is only studied by specific cases (Xu et al, 2003; Adams et al, 2009). A systematic experimental and numerical study of the degradation mechanism of the contaminations on bondline integrity has high value for improvements of the performance of the adhesive bonding composite structures.

The overall goal of the proposed research is to understand several contaminates effect on the adhesive bondline integrity and find the relationship between the adhesive bondline properties with the overall effective adhesive bondline toughness. The specific goals of this work are

1. Examine the effect of contaminates on the adhesive mechanical properties.
2. Examine the relationship between the adhesive mechanical properties and the toughness of adhesively bonded joints.

3. Investigate the associated different failure mechanisms.
4. Establish the acceptable contaminate level for reliable adhesively bonded joints.
5. Develop numerical tools to explore the design space for similar adhesive bonding system.
6. Explore the role of the adhesive thickness on the bond joint toughness.

The specific tools to achieve the above goals are:

1. Utilize nanoindentation to examine the effect of contaminates on the adhesive matrix mechanical properties.
2. Fabricate double cantilever beam (DCB) test samples to assess the adhesively bonded composite joints toughness under different types and levels of contaminates.
3. Develop an optical imaging technique to in-situ trace the crack tip during loading of the DCB specimen.
4. Utilize the finite element method (FEM) and cohesive zone model (CZM) to characterize the fracture initiation and propagation in the adhesive interface layer.
5. Utilize the single shear lap test to characterize the effect of contaminates on the adhesive joint maximum failure load.

1.3 Material System

1.3.1 Fiber-Matrix Composite Material System

Carbon fiber reinforced composites is a class of extremely strong and light composites, which has many application in aerospace and automotive industries. The latest

Boeing 787 is built of at least 50% fiber reinforced composites. This carbon fiber reinforced composites consist of two parts, polymer matrix and carbon fiber reinforcement. The most intrinsic quality of composites is the anisotropy introduced by the fiber direction. The anisotropy can be designed to optimize the desired properties with weight benefit. Another two key advantages of composites are high strength and light weight. According to Ashby plot, the fiber reinforced composites are the best in the tensile strength per unit weight (Ashby, 1992).

The composite material system used in this work is Hexcel IM7-G/8552 with Hexcel W3B-282, representing one of widely-used, aerospace-grade, high-performance carbon fiber. The HexPly 8552 is a high performance tough epoxy matrix for use in primary aerospace structures. The prepreg IM7-G/8552 was manufactured by Hexcel Corporation. This composite system has been used as main landing gear doors for F/A-18 and V-22. When damage occurs, the new main landing gear doors require adhesive bonding to the main structure. However, the main landing gear doors are saturated with hydraulic fluids in service. It is not economically possible to remove all of the hydraulic fluids from the composite surface before bonding repair. The effect of contamination on the adhesively bonded joints and the safety contamination concentration level are of vital for the reliability of this structure.

1.3.2 Adhesive Material

Since synthetic polymeric materials were introduced to bonding composite structures, it has been a popular adhesive for composite structure, because the polymeric adhesive can

give durable, high bonding performance in aggressive environments, for example high temperature (Rossi, 1990). There are two groups of polymeric adhesive, thermoplastics and thermosets. Thermosets are formed by a chemical transformation during curing, which is thermally nonreversible. The crosslink occurs in the formation of curing. The thermosets offer obvious advantage over thermoplastic polymeric adhesive, which includes better high glass transition temperature, chemical resistance (Rossi, 1990) etc.

Two-part thermosetting polymeric adhesive “Loctite Hysol EA9394” is utilized in this study, representing one of the common adhesives utilized in aerospace polymer-matrix fiber reinforced composite. It is an amine-cured epoxy paste adhesive with aluminum powder filler. The adhesive exhibits high toughness and strength at high temperature, and can be cured at room temperature. In Figure 1.2, scanning electron microscope (SEM) inspection of the adhesive surface shows a wide range of the filler size (5-50μm).

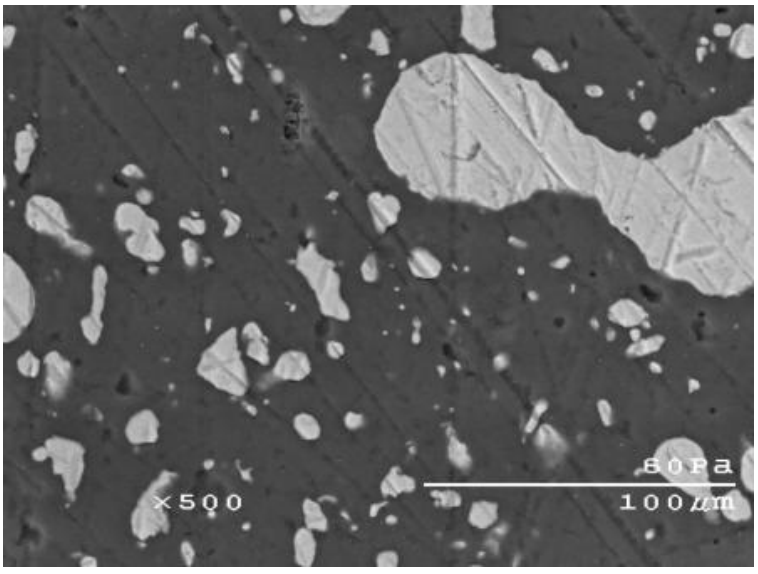

Figure 1.2 SEM image of Hysol EA9394 adhesive surface

1.3.3 Types of Contaminates

For adhesively bonded joints in composite structures, the strength and durability after exposure to contamination are of paramount important. Significant efforts have focused on the characterization of the contamination effect on the adhesive bonding strength. Contamination chemical aging is one of the mechanisms for contaminates degradation. The chemical aging occurs during the oxidation of polymeric adhesive and can be characterized by the debonding of polymer chains (Emanuel, 1987). In polymers, the oxidation reaction rate can be characterized by free radical mechanism (David, 1983; Schnabel, 1981). The free oxidation rate depends both on the reacting temperature and the concentration of contamination. Besides, the structure of polymeric adhesive also affects the degradation rate. The crystalline structure polymer is very dense and can greatly restrict the diffusion of contamination into the polymer. Thus, the safety contamination level should be determined for specific adhesive. The contamination fundamental chemical effect on the polymeric adhesive will cause the degradation of mechanical properties, such as modulus and hardness. This effect on mechanical properties can contribute to the effective adhesive bonding toughness and will be discussed later.

As mentioned above, hydraulic oils are common contaminates for composite structures in aerospace industry. A class of contaminates representing three types of aviation hydraulic oils and two types of mold release agent “frekote” have been adopted in this study as Table 1.1.

	Contaminates	
1	Aviation Hydraulic Oil #1	MIL-PRF-87257
2	Aviation Hydraulic Oil #2	SAE AS1241
3	Aviation Hydraulic Oil #3	MIL-PRF-85570
4	Frekote 44	Mold release agent
5	Frekote 700	Mold release agent

Table 1.1 Different types of contaminates

The contamination concentration levels were chosen by MIL STD 1246C, the level C ($3\mu m/cm^2$) is considered the maximum allowable clean level for repairmen and the level G ($55\mu m/cm^2$) is the maximum listed in the standard.

1.4 Dissertation Organization

In Chapter 2, a whole set of contaminates (hydraulic oils and frekote mold release agents) at level J $55\mu g/cm^2$ is first tested and preliminarily reveal the correlation between the adhesive hardness and the adhesive bonding toughness trend. Finite element model with cohesive zone surface is used to understand the effect of contaminates on the process zone. In Chapter 3, two controlled set of samples exposed to different grades of contaminations are carefully examined. The degradation of adhesive bonding strengths is correlated with the surface feature captured by microscope and surface profilometer. In Chapter 4, a parametric study of the adhesive bonding joints is carried out by finite element model with cohesive surface. The effects of relevant interfacial parameters and material parameters are individually studied. In Chapter 5, the adhesive bonding joints are studied by shear test and double shear lap modeling to reveal the contamination effect in mode II unstable fracture. Chapter 6 summarizes the work presented here. The appendix presents an independent work on image processing analysis of fracture surface in forensics that was also part of the Ph.D. work.

1.5 Reference

1. B. Cantor, M.G. Goringe and E. Ma, Fundamentals of fiber reinforced composite materials, IOP Publishing Ltd (2005).

2. S.C. Her, Stress analysis of adhesively-bonded lap joints. *Composite Structures,* **47**, 673-678 (1999).

3. R.D. Adams and W.C. Wake, Structural adhesive joints in engineering, *Springe*, London (1984).

4. D.M. Hoyt, S.H. Ward, P.J. Minguet, Strength and fatigue life modeling of bonded joints in composite structure, Proc. American Society for Composites (ASC) 15th Technical Conference, 2000.

5. L. Tong, An assessment of failure criteria to predict the strength of adhesively bonded composite doubler lap joints, *Journal of Reinforced Plastics and Composites*, **16**, 698-713 (1997).

6. Z. Suo, C.F. Shih, A.G. Varias, A theory for cleavage cracking in the presence of plastic flow, *Acta Metallurgica et Materialia*, **41**, 1551 (1993).

7. V. Tvergaard, J.W. Hutchinson, Toughness of an interface along a thin fuctile layer joining elastic solids, *Philosophical Magazine A*, **70**, 641-656 (1994).

8. B.F. Sorensen and T.K. Jacobsen, Large-scale bridging in composites: R-curves and bridging laws, *Composites A*, **29**, 1443-1451 (1998).

9. S.N. Abdul Razar and A.R. Othman, A review on the performance of adhesive bonding in polymer composite joints. *Key Engineering Materials,* **471**, 610-615 (2011).

10. I.A. Ashcroft, M.M. Abdel Wahab, A.D. Crocombe, D.J. Hughes and S.J. Shaw, The effect of environment on the fatigue of bonded composite joints. *Composite: Part A,* **32**, 45-58 (2001).

11. M.D. Banea and L.F.M. da Silva, Adhesively bonded joints in composite materials: An overview. *Journal of Materials Design and Applications,* **223**, 1 (2009).

12. M. Zhang and S.E. Mason, The effects of contamination on the mechanical properties of carbon fibre reinforced epoxy composite materials. *Journal of Composite Materials*, **33**, 1363 (1999).

13. M.Y. Al-Mandil, H.S. Khalil, M.H. Baluch and A.K. Azad, Performance of epoxy-repaired concrete under thermal cycling. *Cement & Concrete Composite*, **12**, 47-52 (1990).

14. B.L. Lee and M.W. Holl, Effect of moisture and thermal cycling on in-plane shear properties of graphite fibre-reinforced cyanate ester resin composite. *Composite Part A*, **27A**, 1015-1022 (1996).

15. T. Pribanic, D. McDaniel and V. Musaramthota, Effect of surface contamination on composite bond integrity and durability. 2011.

16. F.L. Paulauskas, C.D. Warren, T.T. Meek, Adhesive bonding via exposure to microwave radiation and resulting mechanical evaluation. Materials Research Society Meeting (1996).

17. A.J. Kinloch, Durability of Structural Adhesives.*Springer* (1983).

18. J.R.J. Wingfield, Treatment of composite surface for adhesive bonding, *International Journal of Adhesion and Adhesives*, **13**, 151-156 (1993).

19. A.J. Kinloch, G.K.A. Kodokian, J.F. Watts, Relationship between the surface free energies and surface chemical compositions of thermoplastic fibre composites and adhesive joint strength, *Journal of Materials Science Letters*, **10**, 815-818 (1991).

20. B.M. Parker and R.M. Waghorne, Surface pretreatment of crabon fibre reinforced composites for adhesve bonding, *Composites*, **13**, 280-288 (1982).

21. N. Ramanujam, T. Nakamura, Estimating surface damage of composite panels with inverse analysis, *Journal of Composite Materials*, **41**, 2471-2498 (2007).

22. R. Adams, J. Cowap, G. Farquharson, G. Margary, and D. aVaughn, The relative merits of the Boeing wedge test and the double cantilever beam test for assessing the durability of adhesively bonded joints, with particular reference to the use of fracture mechanics, *International Journal of Adhesion and Adhesives*, **29**, 609-620 (2009).

23. S. Xu, D. Dillard, G. Dillard, Environmental aging effects on the durability of electrically conductive adhesive joints, *International Journal of Adhesion and Adhesives*, **23**, 235-250 (2003).

24. M.F. Ashby, Materials selection in mechanical design, *Pergamon Press*, Oxford (1992).

25. R.D. Rossi, Engineered materials handbook, ASM International, Materials Park, Ohio (1990).

26. N.M. Emanuel and A.L. Buchachenko, Chemical physics of polymer degradation and stability, *VNU Science Press*, Netherlands (1987).

27. David, D. Sims, Weathering of polymers, *Applied Science Publishers*, London (1983).

28. W. Schnabel, Polymer degradation: principles and practical applications, *Hanser International*, New York (1981).

CHAPTER 2 NANO INDENTATION SURFACE PRESCREENING

2.1 Introduction

Adhesively-bonded structures provide an affordable and low-cost avenue for assembly of complex airborne structures. Assuring integrity of these bonded structures represents a major stumbling block in terms of reliability and assurance of airworthiness. Reliability of bonded joints has been extensively studied using brute-force testing in many service environments. However, a difficulty remains that of establishing a failure criterion or a threshold similar to those for metallic structures. The challenge remains in detecting interfacial progressive damage of bonded structures and the associated weakening of interfacial fracture toughness that can lead to catastrophic failure.

This chapter explores the correlation between the degradation of toughness in adhesively-bonded joints and degradation/changes in measurable mechanical properties of adhesive (e.g. stiffness, yield strength, and hardness). Nanoindentation will be utilized as an effective and non-invasive tool for measuring local material properties. Nanoindentation or depth-sensing-indentation has been applied to a wide range of materials for examining mechanical properties, such as hardness H and modulus E, at the nano-scale (Doerner et al, 1986; Oliver et al, 1992). The mechanical properties of an adhesive layer with contamination at level J will be examined and correlated to measured fracture toughness of adhesively bonded joints for a selected system of adhesive-adherend pairs, using double-cantilever bend

(DCB) testing. The working hypothesis is explained in Sec. 2.2. Details of sample preparation and testing are given in Sec. 2.3. Experimental results are given in Sec. 2.4. The results are rationalized with finite-element simulation of adhesive-adherend pairs with varying levels of interfacial strength σ_o and interfacial fracture energy, Γ.

2.2 Proposed Hypothesis

Adhesively-bonded joint failure may fail into one of the following modes: (i) adhesive failure at the adhesive-adherend interface, (ii) cohesive failure within the adhesive layer, and (iii) substrate failure within the adherend. The highest strength of adhesive-adherend pair is typically the one exhibiting substrate failure within the adherend. In polymer matrix fiber-reinforced composite, adhesive-type failure is the typical failure mode in a compromised adhesive-adherend pair. Accordingly, the central hypothesis of the proposed work is that, for adhesively-bonded joints, there might be a correlation between the degradation of toughness and the mechanical properties of the adhesive layer.

At the local scale of a bondline, the toughness of an adhesive layer is typically characterized by a traction-separation curve (a.k.a. cohesive law), $\sigma = \sigma(\delta)$, as sketched in Figure 2.1. In steady state, the area below the curve is the fracture energy, Γ, a toughness indicator. The cohesive law is regarded as a material property (for each adhesive-adherend pair), and is not significantly affected by the thickness of the adhesive layer (within the commonly used range of 300-400μm, Pardoen et al, 2005). Although the cohesive law is often regarded as a phenomenological model, the mechanisms of each deformation stage can be clearly identified. Under the low traction at the bondline arising from typical service

loads, the adhesive deforms elastically and the interface is intact. After the yield strength of the adhesive σ_Y is reached, the plastic deformation of the adhesive induces a large separation, while the traction increases slowly.

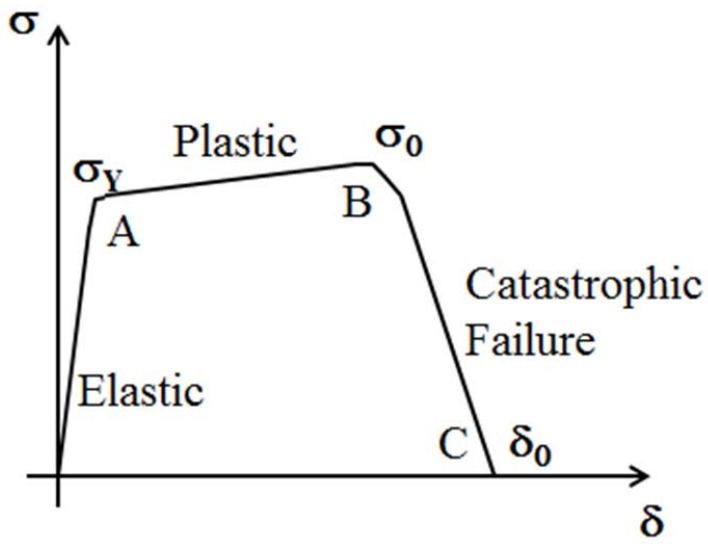

Figure 2.1 The failure process of the adhesive layer could be modeled by a material-specific cohesive law σ(δ)

The increase in traction is due to the combined effect of the increasing hydrostatic stress in the constrained tri-axial stress state and the strain hardening of the adhesive. Finally, when the local traction exceeds the interface strengthσ_0, the adhesive debonds from the adherend. At point C, the adhesive fully separates from the substrate. For such an energy-dissipation process to be effective, the interface strength needs at least to be greater than the yield strength. Otherwise, the plasticity of the adhesive will be entirely shielded, and in this case the adhesive is regarded as unsuitable for the particular adherend system. At the other extreme, when the interface strength is stronger than the ultimate strength of the adhesive,

cracks propagate through the adhesive rather than along the interface; the traction-separation law takes a similar shape with σ_0 reinterpreted as the ultimate strength of the adhesive.

Clearly, the fracture energy of the adhesive layer is directly correlated with its mechanical properties. For example, increasing the yield strength (or hardening rate) would shorten the stage A-B on the cohesive curve and lead to low ductility and perhaps even a sudden ductile-brittle transition when σ_Y is greater than σ_0. On the other hand, aging and environmental contaminants often lead to hardening of most polymer-based adhesives, accompanied by degradation of the interfacial strength. Both effects reduce the fracture energy of the bondline.

The measured mechanical properties of the adhesive σ_Y and E, can be correlated to the measured fracture energy, Γ_{eff} using the following argument. According to Griffith theory (Griffith, 1921), Γ_{eff} scales with the measured indentation modulus as

$$\Gamma_{eff} = \beta \frac{\sigma_\infty^2 a}{E} \tag{1}$$

where β is a geometric factor of order unity, a is the crack length and σ_∞ is the applied remote stress. Accordingly, if contaminates further stiffen the adhesive, Γ_{eff} will drop and vice versa. To understand the role of the adhesive σ_Y , Γ_{eff} can be written as the confluence of the surface or binding energy (energy required to generate new surfaces) γ_{surf} and the energy dissipation through inelastic deformation W_p , such that

$$\Gamma_{eff} = \gamma_{surf} + W_p \tag{2}$$

Utilizing the Irwin approach (Irwin, 1957), the extent of the plastic zone r_p, ahead of the crack tip under SSY, can be expressed as

$$r_p \sim \left(\frac{K_C}{\sigma_Y} \right)^2 \tag{3}$$

K_C is the critical stress intensity factor. Using Tabor's approximation (Tabor, 1951; 1986; Atkins et al, 1965), the indentation hardness is usually considered to be an average measure of the material yield strength in compression ($H \sim 3\sigma_Y$). Accordingly, the work of inelastic dissipation within the adhesive layer scales with the measured indentation hardness is

$$W_p \sim r_p \sim \frac{1}{H^2} \tag{4}$$

To a first-order approximation and for $\sigma_o > \sigma_Y$, it can be assumed that $\Gamma_{eff} \sim \frac{1}{H^2}$. Accordingly a contamination induced softening in the bond layer will increase Γ_{eff}.

In summary, the measured σ_Y and E for the adhesive may provide relative trends for Γ_{eff}, unless overshadowed by significant reduction of σ_o that may embrittle the adhesive-adherend interface.

2.3 Sample Preparation

2.3.1 Nanoindentation Sample Preparation

A nanoindentation test was employed to measure the hardness and modulus of the adhesive EA 9394 when attacked by various kinds of contamination. All contaminants in Table 1.1 have been included in this study. A controlled contamination level of $55\mu g/cm^2$ was adopted, representing Level-J contamination according to MIL STD 1246C. The adhesive Loctite Hysol EA9394 was first pasted on glass slides. The contamination was adjusted by diluting the contaminants with a volatile agent like Hexane. After establishing the proper concentration, the diluted contaminate solution was immediately spread over the uncured adhesive layer, producing a uniform fluid layer with a predetermined height. The selected diluted solution height will result in the proper contamination level per unit area. The contamination level has been verified within a few percent by infra-red spectroscopy. For nanoindentation samples, a layer of the adhesive was spread over a glass slide, then immediately exposed to the thinned contaminate solution. The epoxy was then cured in an oven for 2hrs at 90˚ C (Hysol EA9394 Data Sheet).

2.3.2 DCB Polymer Matrix Composite Sample Preparation

12-ply panels were prepared employing 10 plies of unidirectional prepreg (Hexcel IM7-G/8552) and a bi-directional fabric (Hexcel W3B-282) woven at 45^o on both sides. Standard fabrication of vacuum bagging and hot-press curing methods were implemented as shown in Figure 2.3. The cured panels' surfaces were roughened using 220 alumina grit blasting under 413.7kPa pressure and an estimated nozzle speed of 136kg/hr. A single pass

over the panel with a standoff distance of about 0.3m was utilized with a resulting surface roughness of about 3-4μm. It has been shown (Bossi 2005; Dillingham et al, 2003) that such surface roughness enhances the fracture toughness of the adhesive-adherent pair with prominent mix-mode (fiber pull-out) failure. After surface treatment, the panels were rinsed with water and flushed with Hexane for degreasing. The samples were then cured at 90^{o}C for 2hrs at a heating rate of 15^{o}C/min and a cooling rate of 15^{o}C/min according to NAVAIR 01-1A-21, Sec. 6-7a (2). After the cleaning, a measured dilute contamination was uniformly applied to the composite surface. The adhesive paste was spread on the other surface pair, a 125μm thick Teflon film of 50mm width crack starter. A 250μm shim was inserted around the edge of the panel to maintain the adhesive bond thickness. The two panels were assembled and pressed under 34kPa pressure at room temperature (22^{o}C) for 16 hrs. A final rapid cure was applied for 2hrs at 90˚C in an autoclave furnace. The assembled panels were cut into 1" X 8" samples and aluminum blocks are glued to the ends of the specimens for load transfers. The final DCB sample was as shown in Figure 2.4.

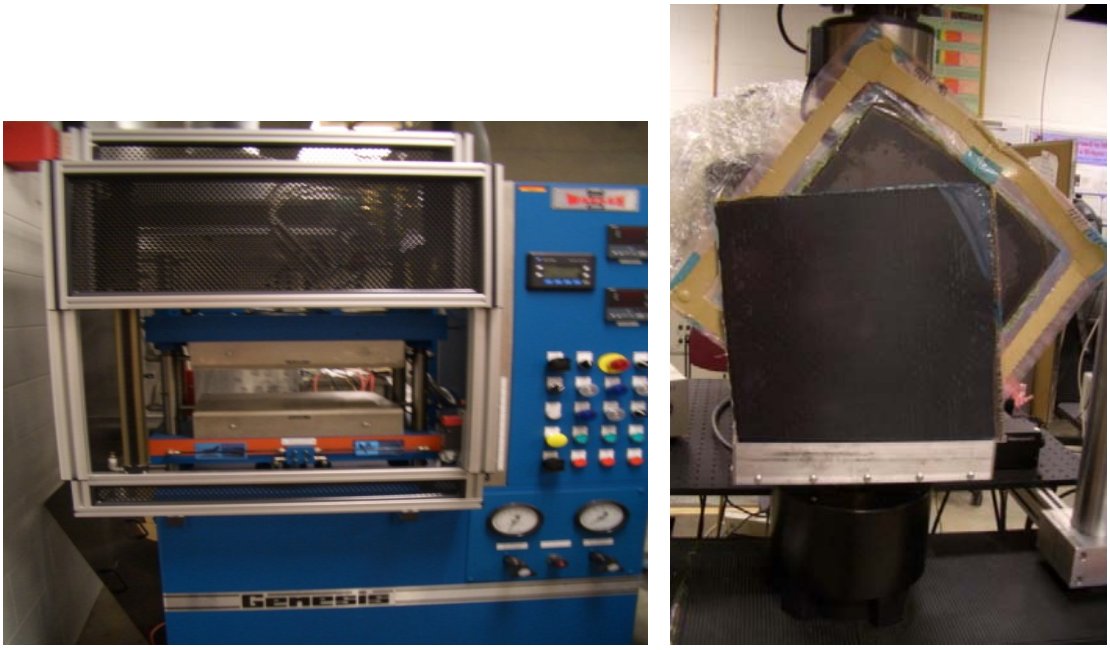

Figure 2.2 (a) The hot-press for laminate manufacturing; (b) A typical composite laminate

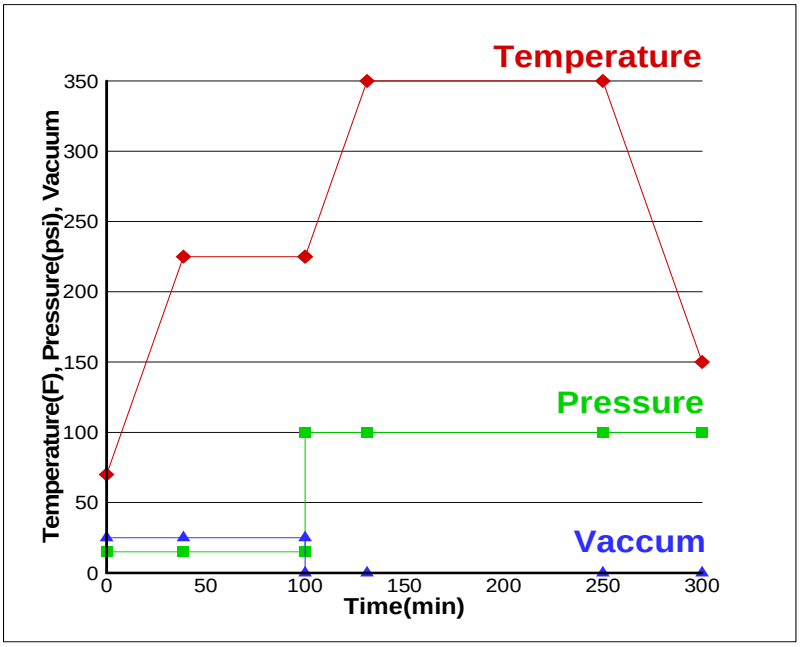

Figure 2.3 The thermal cycle for the fabrication of an IM7/8552 composite laminate.

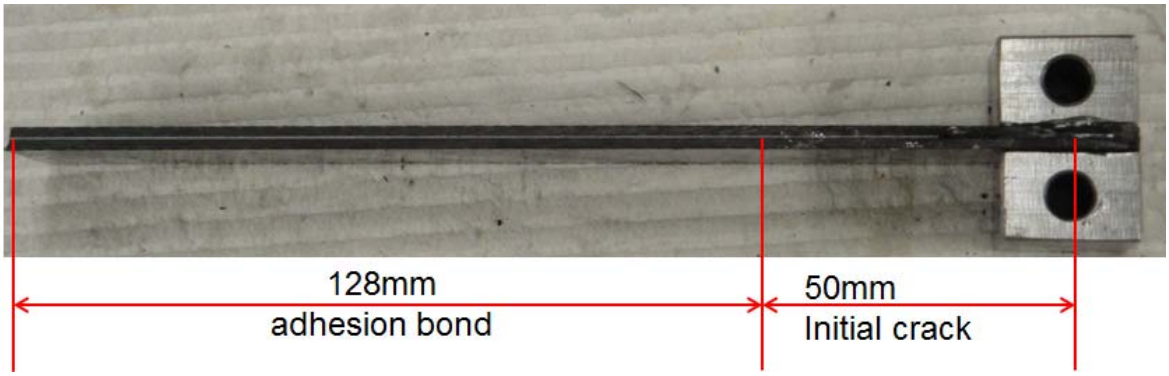

Figure 2.4 Optical image showing the geometric details and dimensions of a DCB specimen.

2.3 Nanoindentation Test Results

The contaminated adhesive was indented from 1000μN to 6000μN at 1000μN intervals. The contact depth was 5μm. Figure 2.5 shows a comparison of the load-displacement curve of reference, hardening, and softening effects.

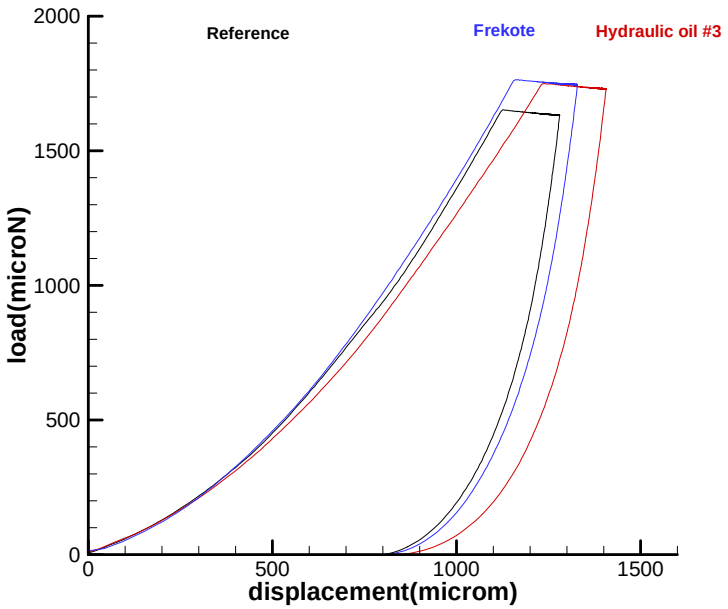

Figure 2.5 The indentation load-displacement curves for the adhesive layer with various contaminates at 55μg/cm^2

From the theoretical work of Oliver and Pharr, we can calculate the modulus and hardness of the tested material by curve-fitting the unloading curve.

$$H = \frac{P_{\max}}{A}$$
$$E_r = \frac{\sqrt{\pi} S}{2\sqrt{A}}$$
$$S = \frac{dP}{dh} \qquad (5)$$

The results are shown as Figures 2.6 and 2.7. From the results, we can notice that the #1 and #2 hydraulic oil has little effect on the adhesive matrix, #3 hydraulic oil has a softening effect on the adhesive EA9394, and Frekote produces a small increase in hardness.

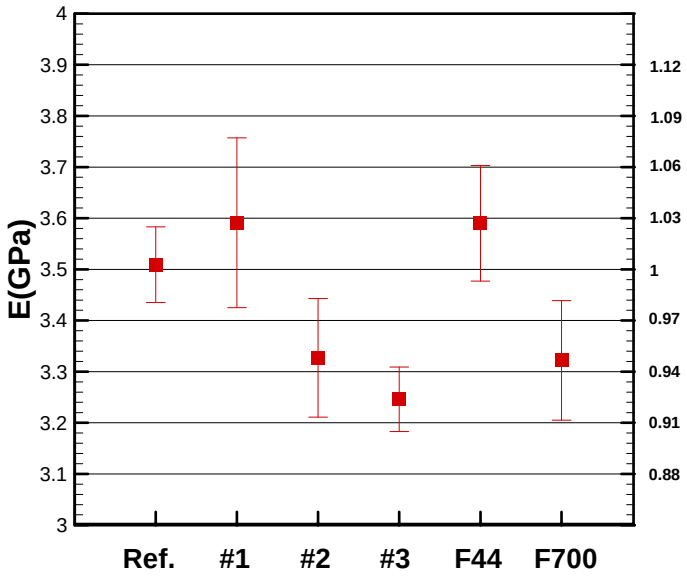

Figure 2.6 The nanoindentation modulus for the adhesive layer with various contaminates at 55μg/cm^2

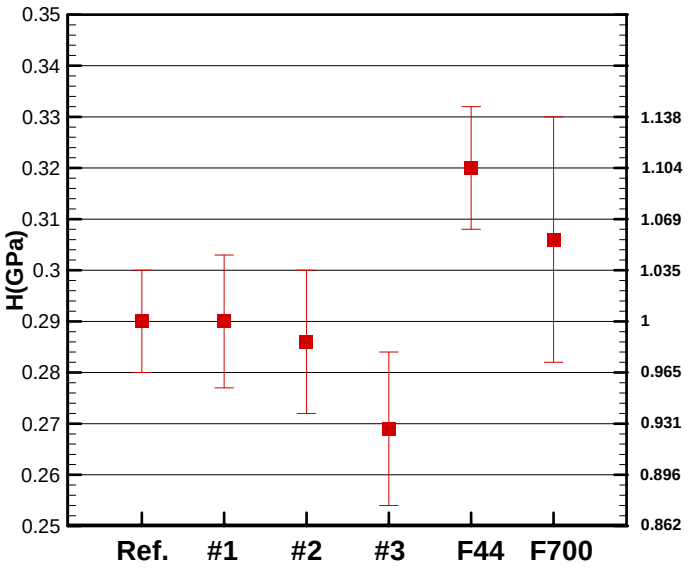

Figure 2.7 The nanoindentation derived hardness for the adhesive layer with various contaminates at 55μg/cm^2

Equation 4 indicates that a reduction in measured hardness or a softening degradation due to contaminant interaction with the adhesive resin will increase the plastic dissipation zone ahead of the crack tip. Such a trend indicates an increase in the plastic dissipation work in fracture toughness. And the hardening effect of Frekote could shrink the plastic zone size and further degrade the effective adhesive bonding toughness. By equation 4, the change of adhesive hardness by contamination can be correlated to the change to the adhesive bonding toughness as in Figure 2.8. However, the trend predicted here deduced from the indentation results can only indicates the comparatively trend between contaminations at the same concentration level. Further DCB test will directly measure the bondline toughness degradation by contaminations.

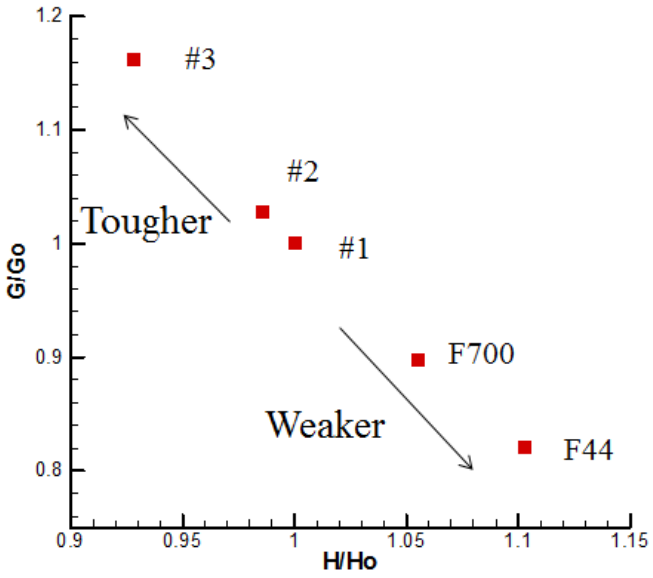

Figure 2.8 The adhesive bonding toughness trend predicted by the nanoindentation measured hardness according to Equation 4

In summary, to understand the effect of contaminants on bondline, a nanoindentation test was used to evaluate the mechanical characteristics of contaminated adhesives. The nanoindentation test gave some insight on the effect of contaminations on bondline toughness. For example, according to the nanoindentation test, the frekote has a greater hardening effect on the bondline than does hydraulic oil #3, which implies that frekote may produce more severe degradation on bond-line strength. However, the accurate bond-line strength after contamination will be determined by direct measurement using the double-cantilever beam test.

2.4. DCB Fracture Toughness Measurements and Results

2.4.1 Experimental Methods

The double cantilever beam tests were carried out in a computer controlled servo-electric testing frame (Instron8800) with a load cell. These tests were performed with displacement control for stable crack propagation. All force-displacement data were recorded during loading samples. After the DCB samples were fastened onto the machine, an optical microscope camera was located ahead of the samples to trace the crack tip. The resolution of the digital images is 30μm/pixel. About 400 images were collected for every DCB sample test and analyzed using a developed Matlab program. The error in the estimated crack length is about 15μm, or about 0.1% of the measured crack length. To obtain a sharp crack tip, the samples were initially loaded because the crack tips were blunt after manufacturing. With a loading rate of 0.02mm/s, the sample was first loaded until a crack started to propagate along the bondline. The sample was then unloaded at a rate of -0.2mm/s until the load decreased to zero. During the second step of reloading, force, crosshead displacement, and in-situ digital images of the sample were simultaneously recorded. DCB tests were repeated on three identical samples to collect consistent data.

For a DCB specimen with end block, the head of the beam is stiffened by the end blocks. So a correction should be involved to the end block effect. Another correction should be considered is the large displacement correction if the specimen opening length is larger than specimen thickness. According to Standard ASTM D5528, the energy release rate G for a DCB specimen is

$$G = \frac{F}{N} \times \frac{3P\delta}{2ba} \tag{6}$$

$$F = 1 - \frac{3}{10}\left(\frac{\delta}{a}\right)^2 - \frac{3}{2}\left(\frac{\delta \cdot t}{a^2}\right) \tag{7}$$

$$N = 1 - \left(\frac{L}{a}\right)^3 - \frac{9}{8}\left[1 - \left(\frac{L}{a}\right)^2\right]\left(\frac{\delta \cdot t}{a^2}\right) - \frac{9}{35}\left(\frac{\delta}{a}\right)^2 \tag{8}$$

F is the large-displacement correction and N is the end-block correction. The width of the sample b was taken to be the average width of three points. The crack length a was the horizontal length from the center of the end block to the crack tip calculated from digital images. L is the half-length of the end block, t is the thickness of the DCB sample, and P and δ are the load and displacement applied on the DCB sample. The value of bond-line toughness is equal to the steady-state energy release rate.

2.4.2 Results and Discussions

Three identical samples were tested at Level-J contamination of 55μg/cm2 (MIL STD 1246C). Figure 2.9 shows three typical cases of the force-displacement data and the corresponding calculated energy release rate. The results show varying adhesion energy degradation. The worst were the Frekote with about 7% residual adhesive fracture toughness. The best contaminant was Hydraulic fluid #3, although it did not attain more than 30% of the adhesive fracture toughness. A summary of the measurements is given in Table 2.2 and Figure 2.10. We speculate that the applied contaminants contribute to the shielding of the process zone, which is the main reason for bond-line strength degradation.

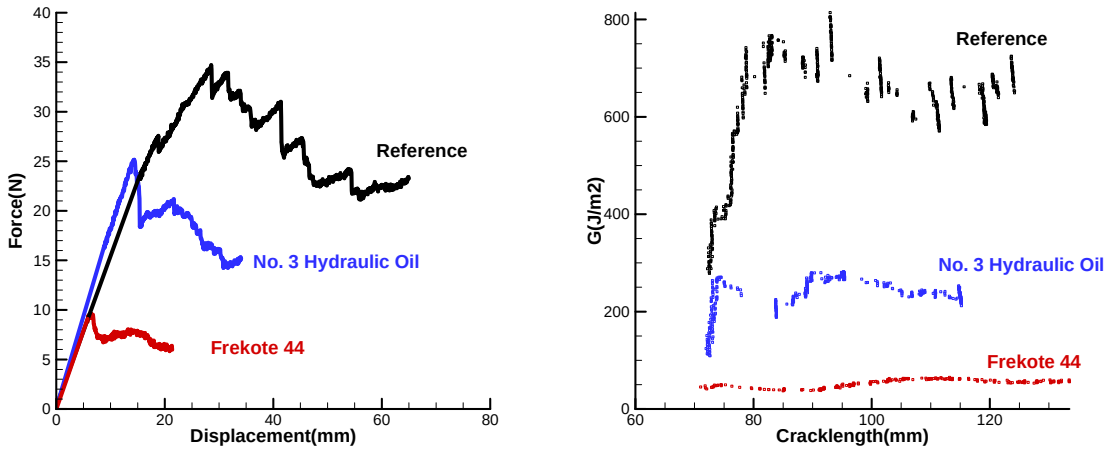

Figure 2.9 DCB test results: (a) Force-displacement curves; (b) The measured fracture energy release rate (reference, No.3 hydraulic oil at 55μg/cm^2, frekote 44 at 55μg/cm^2).

	Ra (μm)	**G (J/m^2)**	**STDEV (J/m^2)**	**Residual**	**Failure Type**
Unexposed	4.98	685	75.5	100%	Mixed
#1(55μg/cm^2)	4.84	115.6	30.3	16.9%	Adhesive Failure
#2(55μg/cm^2)	5.51	133.8	13.8	19.5%	Adhesive Failure
#3(55μg/cm^2)	4.13	206	94.1	30.1%	Adhesive Failure
Frekote44	5.91	50.3	18.3	7.3%	Adhesive Failure
Frekote700	4.16	63.8	9.3	9.3%	Adhesive Failure

Table 2.1 Summary of the fracture toughness measurement for different contaminates highlighting the several chemical degradation of the adhesive strength

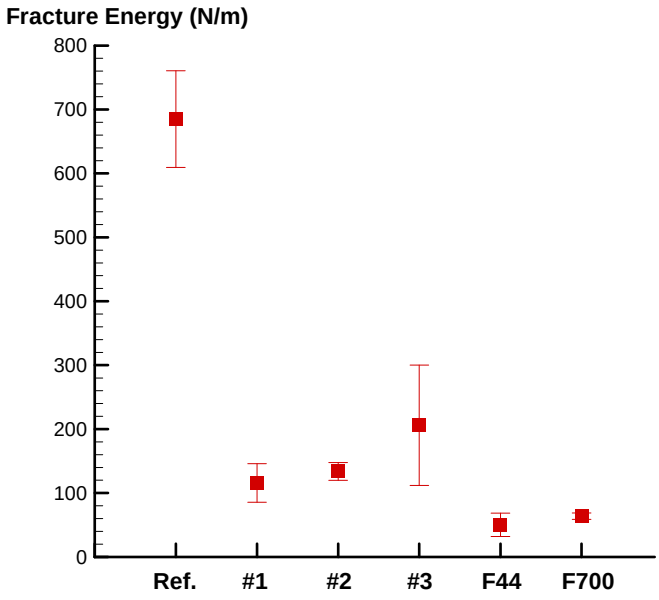

Figure 2.10 Summary of the fracture toughness measurement for different contaminates at Level-J (55μg/cm^2) highlighting the severe degradation of the adhesive strength.

The DCB results show a similar trend to those of the nanoindentation results. A contaminate, such as Frekote, has a hardening effect on adhesive that could cause more degradation on bond-line toughness and vice versa. Considering that the five contaminants applied on the bondline at the same level and #1 hydraulic oil have little effect on the adhesive matrix, we use #1 oil as the standard in plotting a comparison of the nanoindentation prediction and the DCB measurements, as shown in Fig. 2.11. For five contamination cases, the DCB measured bond-line toughness and the hardness were normalized by #1 hydraulic oil. From Equation 4, the nanoindentation predicts a bond-line toughness change with $\Gamma \sim \frac{1}{H^2}$. From Figure 2.11, though the nanoindentation could show the same trend as the contamination effect, the actual contamination effect on toughness was

more significant than that predicted by nanoindentation. The reason of the discrepancy may be attributed to the combination effect of hardness and the surface properties change. The fiber bridging zone, which is main feature in the adhesively bonded composites fracture, is not involved in the adhesive hardness prediction. To reconcile the discrepancy, finite-element modeling was used to determine the mechanism of the contamination degradation effect. The data from this work was used to develop a cohesive element in numerical simulation.

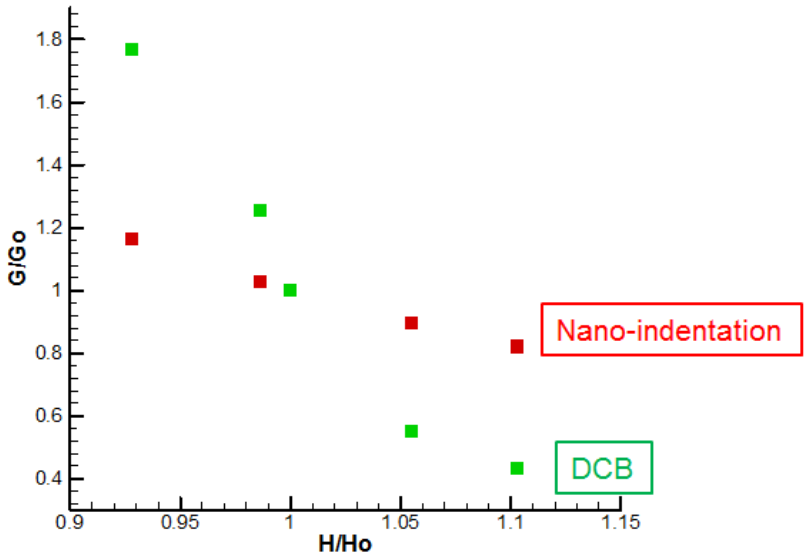

Figure 2.11 Summary of the residual fracture toughness at Level-J (55μg/cm^2) for different contaminates type

2.5 Role of Adhesion and Plastic Dissipation with FEM Analysis and Discussions

Finite-element analysis (FEA) has been widely employed to predict bond strength of adhesion (Song et al, 2006; Kafkalidis et al, 2002; Hua et al, 2008). A cohesive element with separation law has proven to be a successful tool for simulating the bonding break (Lane et

al, 2000). Theoretical and numerical studies of interface toughness of a thin-layer bond have been presented by Hua and Tvergaard (Hua et al, 2008; Tvergaard et al, 1994) and these studies give a solid foundation to the double-cantilever beam test.

For simulating crack growth in the model, the cohesive surface element was applied between the adhesive layer and the composite substrate. The cohesive surface is an interface element with zero thickness. The constitutive relationship of this criterion is as Figure 2.12:

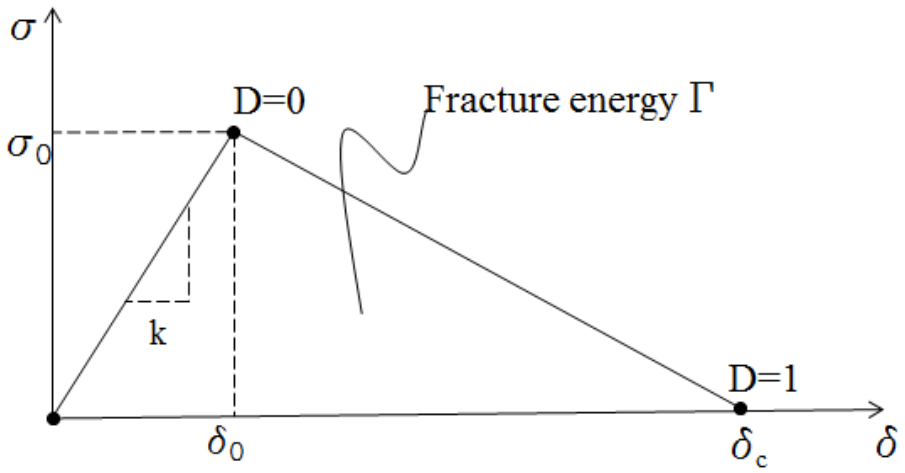

Figure 2.12 Schematic diagram of the phenomenological traction separation law of cohesive surface element

The constitutive curve describes the failure behavior of the cohesive element. The area under the constitutive curve is the intrinsic fracture energy of the cohesive element, corresponding to the interfacial fracture toughness. The traction separation law is determined by three independent parameters: k, σ_0, Γ. In our work, the stiffness k of the cohesive behavior was calculated from modulus $k = Et$, where t is the element size. The interfacial fracture energy was determined from the total effective fracture energy and the critical force

was determined from the fracture initiation force. The parameters used in this study are shown in Table 2.2.

	Reference-no contamination	Level J contamination
Stiffness K (N/mm)	3e6	3e6
Maximum stress σ (MPa)	135	60
Interfacial fracture energy G (J/m^2)	250	50

Table 2.2 The cohesive surface parameters used in the FEM simulation

The bond-line toughness was defined at a time when the total energy release rate reached a plateau. The sensitivity of the macroscopic fracture process to intrinsic cohesive behavior was clear, as shown in Figure 2.13. From Figure 2.14, it can be seen that the plastic dissipation portions are predominant in affecting total fracture toughness. Further examination of the plastic zone shows that the plastic zone size in reference model 1 is 0.06mm, while it deceases almost to zero at Level J-55$\mu g/cm^2$.

From the simulation, we can conclude that the total fracture energy is composed of two parts; one comes from the intrinsic fracture surface energy and another larger one is dissipated by the plastic work during the crack growth. Notice that the process zone was dramatically reduced by the decrease in interfacial fracture toughness; we conclude that the contaminations attacking the bondline would not only affect the adhesive properties, but also the decrease in interfacial fracture energy would further shield the plastic dissipation. Such an interfacial shielding effect could explain the discrepancy between the DCB results and the nanoindentation prediction.

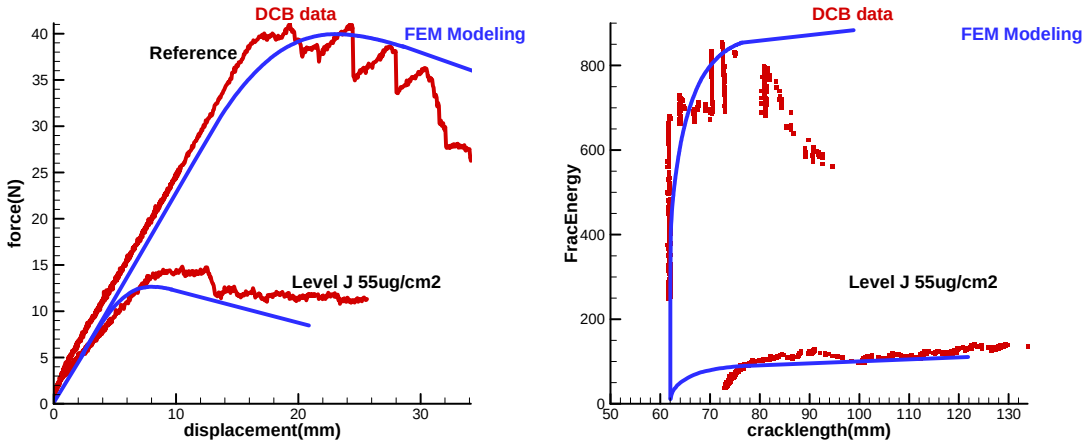

Figure 2.13 Comparison between FEM results and the experimental data for reference and hydraulic oil #1@55μg/cm^2.

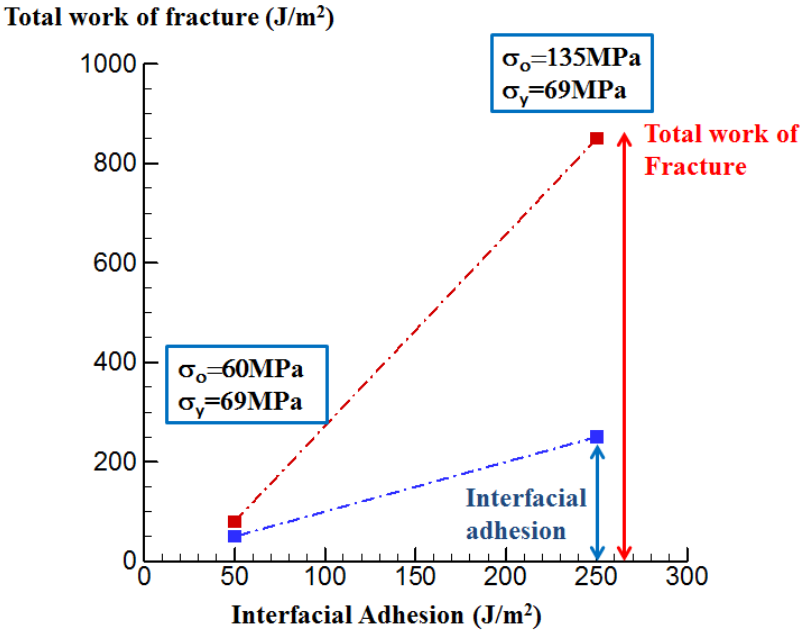

Figure 2.14 FEM results showing the increased role of plastic dissipation when σ_o of the interface is greater than the adhesive yield strength σ_y

2.6 Conclusions

To understand the effect of contaminants on adhesive bonded structures, nano-indentation test was used to evaluate the modulus and hardness of the contaminated adhesives and Mode I DCB test was used to measure the fracture toughness of the contaminated bondline toughness. The nanoindentation test showed the softening effect on the adhesive EA 9394 by hydraulic oil #3 and the hardening effect by frekote 44 and 700, and the energy release rate calculated from DCB test shows only about 13% bond strength left after various contaminants. The nanoindentation data can give some hint about the qualitative degradation level. The frekote, which has hardening effect on adhesive, has more severe degradation on the bondline than hydraulic oil #3. The data from experimental work is used to develop a cohesive element model in numerical simulation. Further simulations successfully showed the interfacial shielding effect of contaminants on the bond-line strength and fracture process.

2.7 References

1. M.F. Doerner and W.D. Nix, A method for interpreting the data from depth-sensing indentation instruments, *Journal of Materials Research*, **1**, 601-609 (1986).

2. W.C. Oliver and G.M. Pharr, An improved technique for determining hardness and elastic modulus using load and displacement sensing indentation experiments, *Journal of Materials Research*, **7**, 1564-1583 (1992).

3. T. Pardoen, T. Ferracin, C.M. Landis and F. Delannay, Constraint effects in adhesive joint fracture. *Journal of the Mechanics and Physics of Solids*, **53**, 1951-1983 (2005).

4. A.A. Griffith, The phenomena of rupture and flow in solids, *Philosophical Transactions of the Royal Society of London*, **A 221**, 163-198 (1921).

5. G. Irwin, Analysis of stresses and strains near the end of a crack traversing a plate, *Journal of Applied Mechanics*, **24**, 361–364 (1957).

6. D. Tabor, Hardness of Metals, Oxford University Press, Oxford (1951).

7. A.G. Atkins and D. Tabor, Plastic indentation in metals with cones, *Journal of the Mechanics and Physics of Solids*, **13**, 149-164 (1965).

8. ASTM Standard D5528, Test method for mode I interlaminar fracture toughness of unidirectional fiber-reinforced polymer matrix composite, Annual Book of ASTM Standards, **15.3**. ASTM Int., W. Conshohocken, PA

9. R. Bossi, R. Carlsen, F.J. Boerio, G. Dillingham, Composite surface preparation QA for bonding, SAMPE (2005).

10. R.G. Dillingham, S. Conyne-Rapin, F.J. Boerio, R.H. Bossi, R. Crane, Surface preparation of composite materials for adhesive bonding, Adhesion Society Meeting (2003).

11. Y. Hua, A.D. Crocombe, M.A. Wahab, I.A. Ashcroft, Continuum damage modeling of environmental degradation in joints bonded with EA9321 epoxy adhesive, *International Journal of Adhesion and Adhesives*, **28**, 302-313 (2008).

12. V. Tvergaard, J.W. Hutchinson, Toughness of an interface along thin ductile layer joining elastic solids, *Philosophical Magazine A*, **70**, 641-656 (1994).

13. M. Lane, R. Dauskardt, A. Vainchtein, H. Gao, Plasticity contributions to interface adhesion in thin-film interconnect structures, *Materials Research Society*, **15**, 2758-2769 (2000).

14. M.S. Kafkalidis, M.D. Thouless, The effects of geometry and material properties on the fracture of single lap-shear joints, *International Journal of Solids and Structures*, **17**, 4367-4383, (2002).

15. Y. Hua, A.D. Crocombe, M.A. Wahab, I.A. Ashcroft, Continuum damage modeling of environmental degradation in joints bonded with EA9321 epoxy adhesive, *International Journal of Adhesion & Adhesives*, **28**, 302-313, (2008).

16. S.H. Song, G.H. Paulino, W.G. Buttlar, Simulation of crack propagation in asphalt concrete using an intrinsic cohesive zone model, *Journal of Engineering Mechanics*, **132**, 1215-1223 (2006).

CHAPTER 3 DOUBLE CANTILEVER BEAM TEST

3.1 Introduction

Many researchers have examined a great number of complex and synergistic factors that may affect the reliability of the bondline (Banea et al, 2009). Bond-line contaminations (Crane et al, 2008) and joint-surface pretreatment (Jone, 1991; Chin et al, 1996; Smith et al, 2007) have been found to be the principal factors. Surface treatment methods on composite surfaces (for example sand blasting, plasma cleaning (Davies et al, 1991), peel ply (Kanerva et al, 2013)) were proposed for improving bonding toughness (Dillingham et al, 2013). Adhesive-bonding-joint failure has three modes: i) adhesive failure at the adhesive-adherend interface; ii) cohesive failure within the adhesive layer, and iii) substreate failure within the adherend. Some studies have found that surface treatment can change the failure mode to improve bonding toughness. A too-roughened surface leads to cohesive failure or substrate failure, and a surface not roughened enough leads to a low estimation of degradation of bondline toughness. According to research at Boeing (Bossi et al, 2005), 3-4μm roughness gives a proper level of bonding strength with stable fracture propagation along the bondline.

The double cantilever beam test was first introduced for fracture toughness measurement in 1966 (Mostovoy et al, 1966). The DCB tests have also been used to study the static, dynamic, fatigue and environmental loads on adhesive bonding strength (Joseph et al, 1993; Rakestraw et al, 1995; Rao et al, 1995). The fracture energy of adhesively bonded joints can be determined by the quasi-static DCB test with compliance method according to ASTM Standard D5528. One of the assumptions for the standard is the elasticity of the

cantilever beam. Thus the plastic work only happens in the adhesive layer and the bondline. In this chapter, double-cantilever beam test is used to measure the bond-line toughness of adhesively bonded joints with different level of hydraulic oil.

The composite structure is composed of 10-ply Hexcel IM7-G/8552 composite and Loctite Hysol EA9394 paste adhesive was used to bond two composite cantilever beams. Aviation hydraulic oil is a commonly-found substance in service environments and must be cleaned off before composite repair. Various levels of aviation hydraulic oil were examined to determine the role of contamination exposure level on bond-line toughness. The resulting DCB data and fracture surface roughness is carefully examined to determine the underlying mechanism of the fracture process.

3.2 Materials and Sample Preparation

3.2.1 Materials

According to the degradation mechanisms proposed by David (David, 1983; Schnabel, 1981), the diffusion rate of the contamination in the polymeric adhesive depends on the temperature and the concentration level.

In this chapter, the effect of contamination levels on the adhesive bonding toughness was directly measured by DCB test. Aviation hydraulic oil #1 was chosen (MIL-PRF-87257) as contaminant applied at the adhesive bondline. Chapter 2 showed that #1 oil has no effect

on the mechanical properties of selected adhesive EA9394. In accordance with maintenance standard (MIL STD 1246C), the contamination levels in Table 3.1 were selected.

Contamination level	Surface concentration
A	1 μm/cm^2
C	3 μm/cm^2
G	10 μm/cm^2
J	55 μm/cm^2

Table 3.1 The contaminates concentration levels

3.2.2 Sample Preparation

ASTM D5528 is a sophisticated standard protocol for mode I DCB testing. In accordance with that standard, the sample laminates were made of 10-ply stacked unidirectional prepreg (Hexcel IM7-G/8552). Additional one-layer bi-directional woven fabric (Hexcel W3B-282) was used as a cover layer at 45^o on both sides. Standard fabrication methods of vacuum bagging and hot-pressing curing methods were used. The cured composite were roughened using 220 alumina grit under 413.7kPa pressure and an expected nozzle speed of 136kg/hr. A single pass over the panel with a stand-off distance about 0.3m. The resulting surface roughness was about 3-4μm. Figure 3.1 and Figure 3.2 show the composite surface before and after the sandblasting. Figure 3.3 shows the surface roughness as determined by a Zygo profilometer. After surface treatment, the composite were rinsed with water and wiped with Hexane for degreasing. Then the samples were cured at 90^{o}C for 2hrs at a heating rate of 5^{o}C/min and a cooling rate of 5^{o}C/min (NAVAIR 01-1A-21, Sec. 6-7a (2)). After cleaning, measured dilutions of hydraulic oils were uniformly applied on the roughened composite surfaces. The adhesive was spread onto another sand-blasted composite surface and a 125μm thick Teflon film of 50mm width was inserted as a crack starter. A 250μm shim was inserted around the edge of the panel to support the adhesive bond

thickness. The supported shim was used to keep the adhesive layer thickness under curing pressure. The two-composite panel was assembled and stacked under 34kPa pressure at room temperature (22^{o}C) for 16 hours. A round fixture was used to apply even pressure, as shown in Figure 3.4. A subsequent curing step was applied for 2 hours at 90˚C in an autoclave. The glass transition temperature of the cured adhesive is around 82˚C. The thickness of the adhesive layer was around 0.4mm measured after bonding. The spill-out of the adhesive from the specimen edges were cut out. After curing, the composite stack was cut into 1” X 8” pieces. Aluminum end blocks for load transfer were glued to the ends of the specimens.

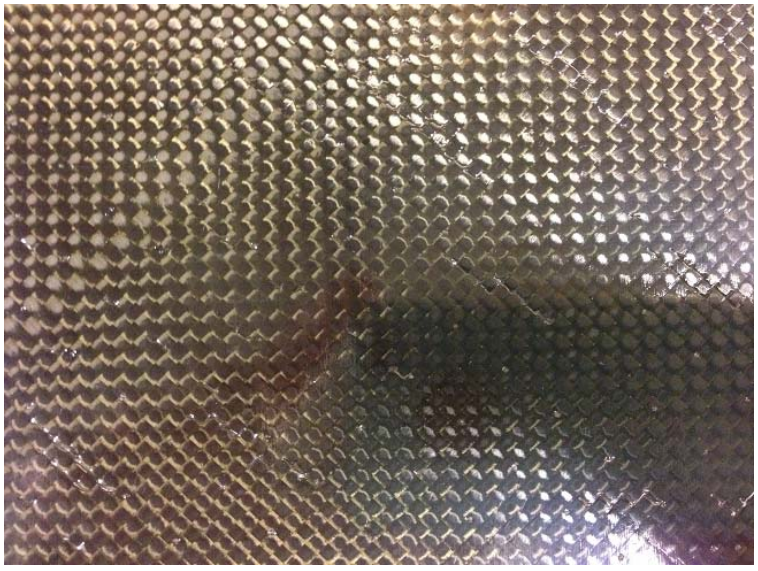

Figure 3.1 An optical image of the composite panel surface before sand blasting

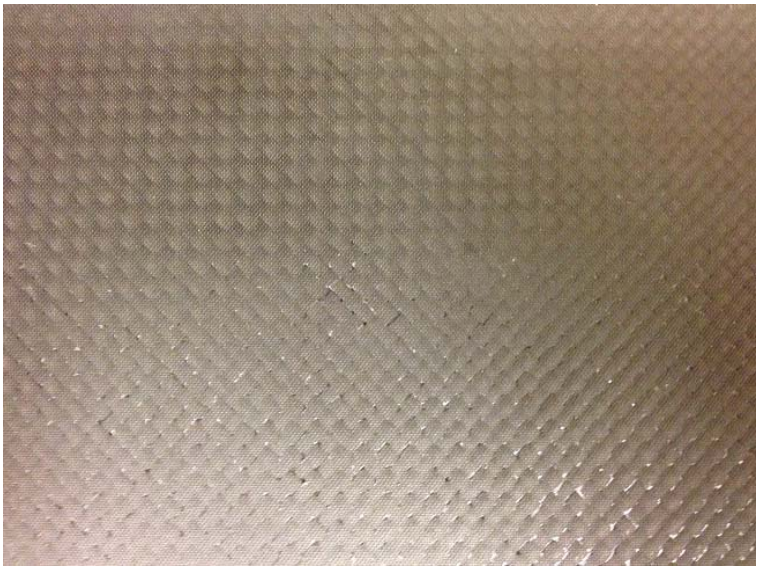

Figure 3.2 An optical image of the composite panel surface after sandblasting

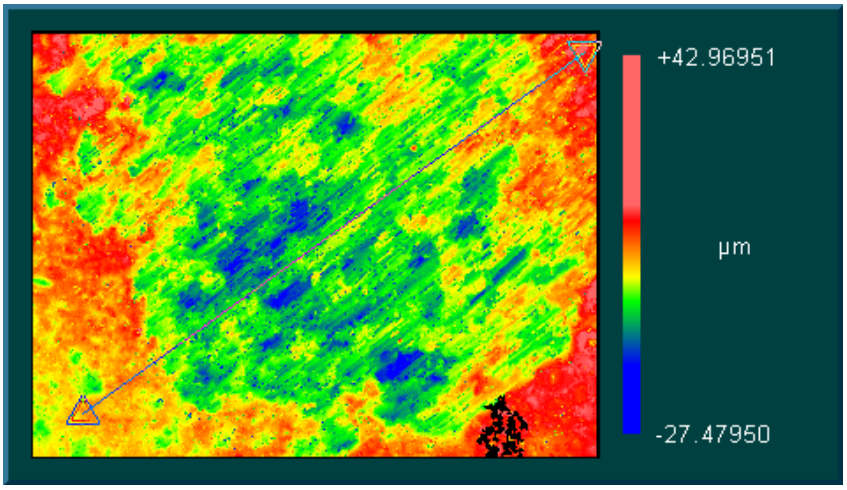

Figure 3.3 The surface topology of a composite panel after sandblasting, roughness is 4.839µm

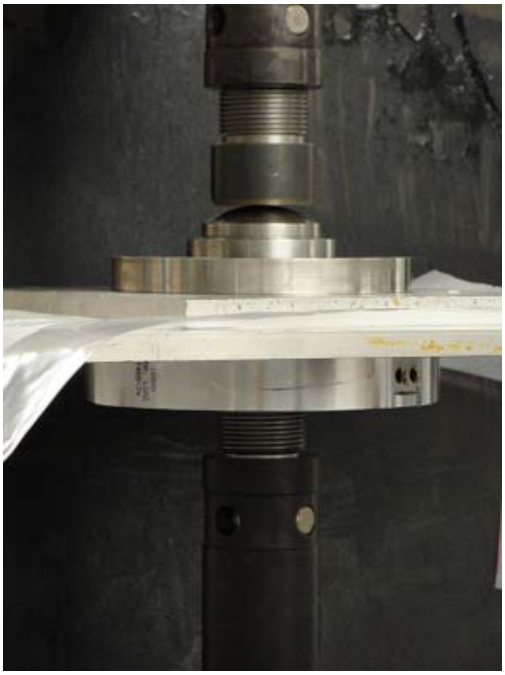

Figure 3.4 The Compression fixture for DCB sample assembly

3.3 DCB Fracture Test Protocol

3.3.1 DCB Testing

The double-cantilever beam tests were carried out in a computer-controlled servo-electric testing frame (Instron8800), as shown in Figure 3.5. These tests were performed with displacement control for achieving stable crack propagation. Figure 3.6 shows a typical loading process for the experiment. Because of the blunt crack tips after manufacture, the samples were initially loaded to obtain a sharp crack tip, with a loading rate of 0.02mm/s, the sample was first loaded until a crack began to propagate along the bondline. Then the sample was unloaded at a rate of -0.2mm/s until the load dropped to zero. If the plastic deformation had occurred in the composite cantilever beam, the force-displacement curve would not return to the origin. From the load-displacement data in our work, the force-displacement

curves did return to the origin, which indicates that all of the cantilever beam deform pure elastically. During the second step of reloading, force, crosshead displacement, and in situ digital images of the sample were simultaneously recorded. The DCB tests were repeated on three identical samples to collect consistent data.

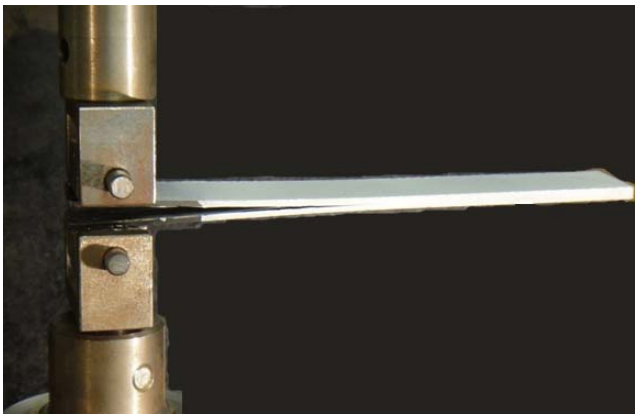

Figure 3.5 The DCB expertimental testing setup, showing the loading bloacks

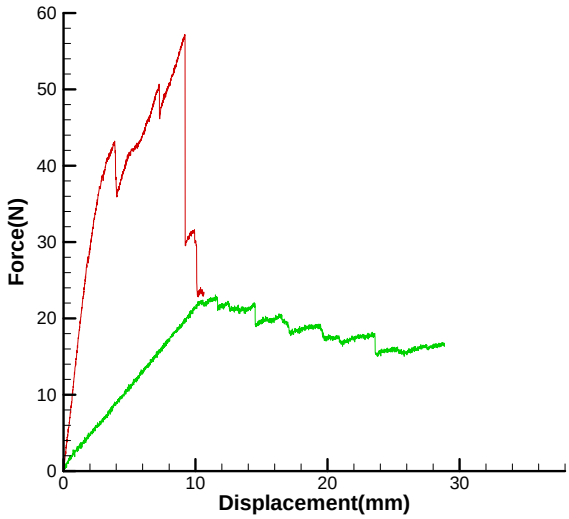

Figure 3.6 Experimental force-displacement curve for a DCB test, showing the initiation stage (red) and the propagation stage (green). (Reference-no contamination)

3.3.2 In-situ Measurement of Crack Tip Length

For calculating the energy release rate through the compliance method, in-situ crack-tip length was measured through image processing. During the test, an optical microscope camera was located ahead of the samples to trace the crack tip. The resolution of the digital images was 30μm/pixel. About 400 images were collected for every DCB sample test and analyzed using a Matlab program developed for crack length measurement. The Matlab program transforms the image into binary code, and then located the crack zone in the image. In the crack zone, the number of pixels from the left end to the crack tip is measured and converted into length. Figure 3.7 is a typical image processed by the program. The error in the estimated crack length is half pixel, about +/-15μm, or about 0.05% of the measured crack length.

Figure 3.7 Matlab image processing output for a DCB sample (white bands), showing the original opened crack flanks (black wedge) and the trace of the crack tip as it propagates (white central line).

3.3.3 Fracture Energy Calculation

According to Standard ASTM D5528, the energy release rate G for a DCB specimen is

$$G = \frac{F}{N} \times \frac{3P\delta}{2ba} \tag{9}$$

$$F = 1 - \frac{3}{10}\left(\frac{\delta}{a}\right)^2 - \frac{3}{2}\left(\frac{\delta \cdot t}{a^2}\right) \tag{10}$$

$$N = 1 - \left(\frac{L}{a}\right)^3 - \frac{9}{8}\left[1 - \left(\frac{L}{a}\right)^2\right]\left(\frac{\delta \cdot t}{a^2}\right) - \frac{9}{35}\left(\frac{\delta}{a}\right)^2 \tag{11}$$

F is the large-displacement correction and *N* is the end-block correction. The width of the sample *b* is taken as the average width of three points. The crack length *a* is the horizontal length from the center of the end block to the crack tip calculated from digital images. *L* is the half-length of the end block, t is the thickness of the DCB sample, and *P* and δ are the load and displacement applied to the DCB sample. The value of bond-line toughness is equal the steady-state energy release rate.

As the load versus displacement curve start to deviate from linearity, the loading reaches the initial energy release rate G_I. After the sufficient crack advanced, the energy release rate becomes stable and the specimen reaches the steady state energy release rate G_{ss}. The steady state energy release rate is used to evaluate the adhesive bonding toughness.

3.4 Results and Discussions

3.4.1 The Surface Treatment

Over years, researchers proposed several theories to provide an explanation for understanding the mechanisms of the adhesive adhesion. However, none of the theories can individaully give a full understanding of adhesion phenomenon. Mechanical interlocking is one of theory to explain the mechanism of adhesion proposed by McBain and Hopkins (McBain et al, 1925). They believe that the mechiancal interlock could prevent the adhesive from being peeled off the surface. The interlock occurs when a liquid adhesive flow into the surface pores and solidify. Some researchers found that the porous surface did improve the adhesion strength (Venables et al, 1979). In general, the roughening of the surface could results in a increased surface area. And the increased effective surface enhance the surface energy between the adhesive and adherend. However, it should be noted that some researcher also found that smooth adherend surface can give good adhesion for certain materials (Mittal, 1976). Sand-blasting is commonly used to increase the roughness of the surface and also to remove some contamination from the surface. Some researchers have found that increasing the surface roughness to about 4μm shifts the failure from the adhesive/adherent interface to a substrate failure of the adherend with possible fiber pull-out (Bossi, 2005). Such a shift in failure mechanism would greatly increase the bond-line fracture toughness.

For evaluating the effect of sandblasting, typical load-displacement and bond-line toughness are shown in Figures 3.8 and 3.9. From these results, it is clear that the sand-blasted surface can provide better bonding tougness and stable crack propagation for the

selected composite system IM7/8552. The original smooth-molded surface, as expected, has low bond-line toughness because of its low surface roughness, leading to an unstable break. After DCB samples break, close examinations of the fracture surfaces show typical mixed-mode failure for the sandblased surface and clean interfacial failure for the smooth surface. The reason for the transition of the failure mode could be explained by the interlock mechanism. The surface roughening increases the roughness Ra from 1μm to 4μm. Thus, the micro-pores on the surface can increase the surface energy and prevent crack from unstable propagation. From these results, we felt that 3-4μm roughness was suitable for the composite system under study and we used sand-blasting in this work to evaluate effects of contaminant on the surface-bondline.

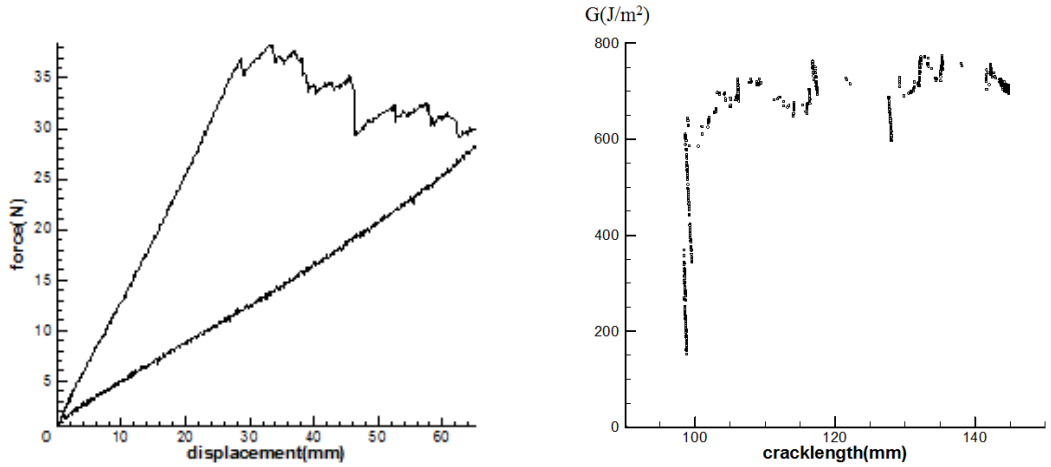

Figure 3.8 Experimental force-displacement curve for a DCB test and the corresponding fracture energy for a of sand blasted surface.

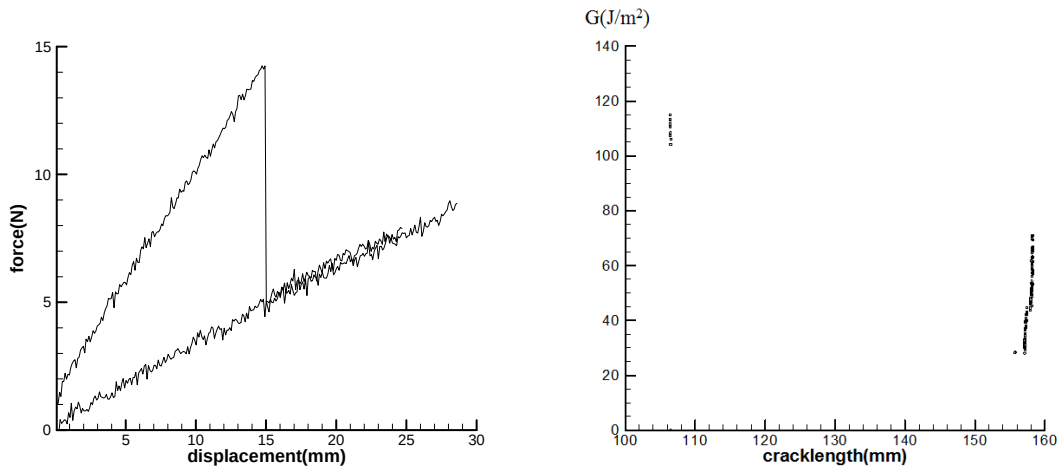

Figure 3.9 Experimental force-displacement curve for a DCB test and the corresponding fracture energy for the as pressed "smooth" composite panel surface.

3.4.2 Role of Contamination Levels A, C, G, J

In real application, the acceptable concentration level of contamination is critical for the reliability of the adhesive bonding structures. A sophisticated standard of concentration levels is required to guide the manufacturing and repairmen process. In this segment, we will measure the bondline degradation by contamination for establishing a standard. And the contamination concentration is connected to the bondline strength by cohesive zone model.

The role of hydraulic fluid #1 MIL-PRF-87257 was further explored at levels A, C, G and J. It was found that even level-C (3μg/cm^2), previously considered to be a safe level, could result in significant adhesion-strength degradation, Summaries of the force-displacement curves and the corresponding calculated adhesion-fracture toughness are given in Figures 3.10-3.13. Figure 3.15 summarizes the calculated fracture toughness for each contamination level. The insert images show the transition from fiber-pull-out failure

mechanisms at the reference state to bond-line failure at level J. Table 3.2 summarizes the experimental measurements.

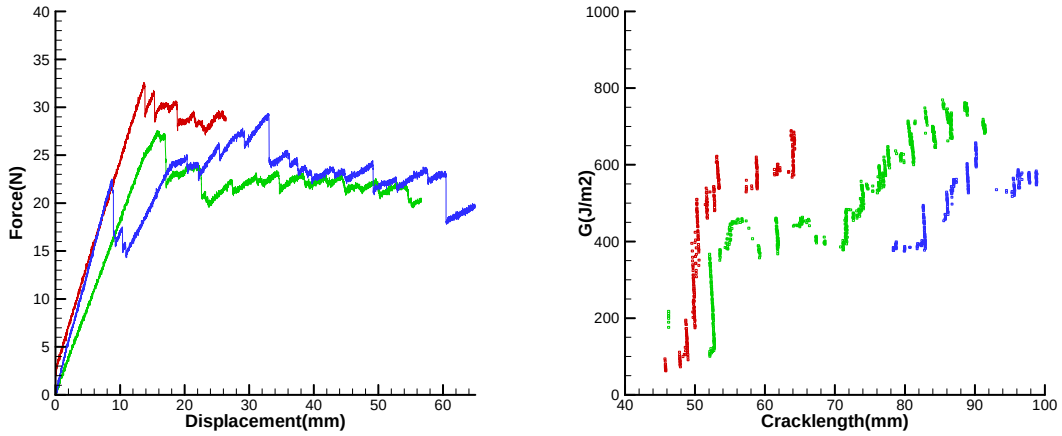

Figure 3.10 Force-displacement curves and the corresponding fracture energy release rate for the hydraulic fluid #1 @1μg/cm^2

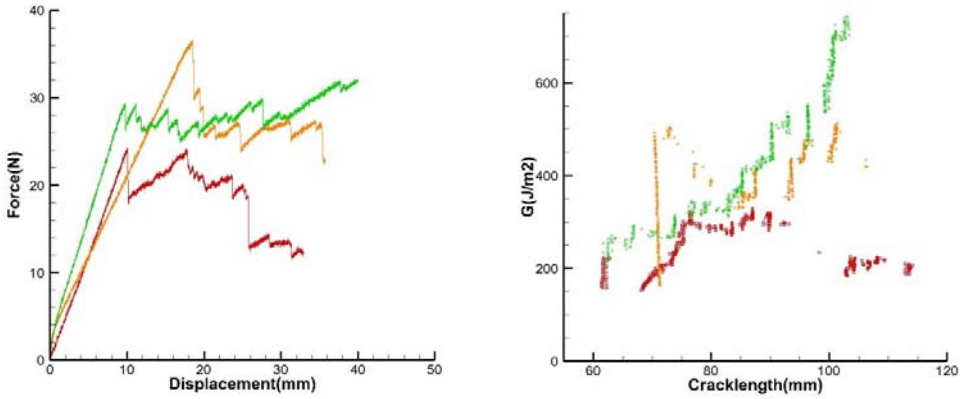

Figure 3.11 Force-displacement curves and the corresponding fracture energy release rate for the hydraulic fluid #1 @3μg/cm^2

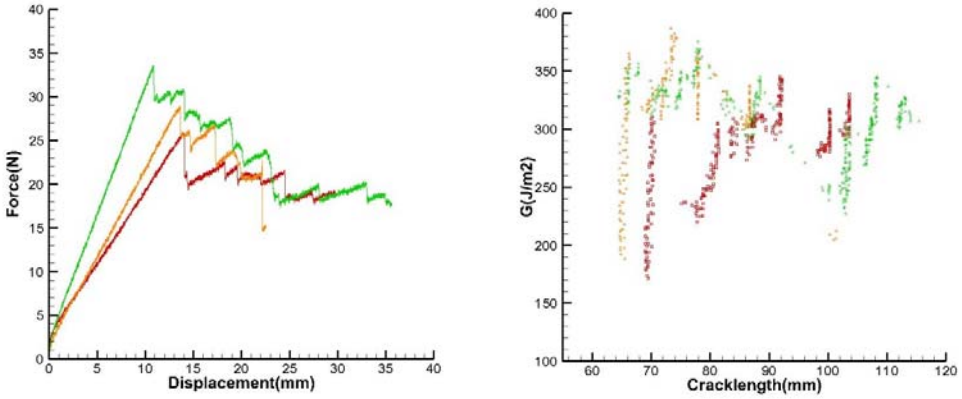

Figure 3.12 Force-displacement curves and the corresponding fracture energy release rate for the hydraulic fluid #1 @10μg/cm^2

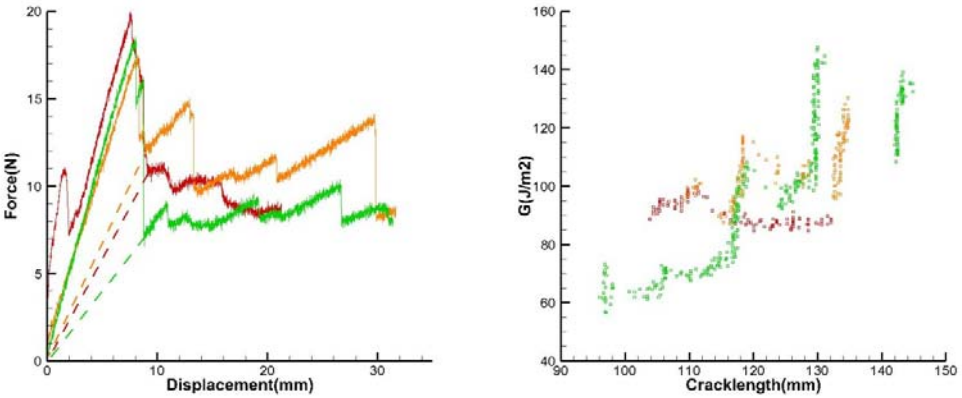

Figure 3.13 Force-displacement curves and the corresponding fracture energy release rate for the hydraulic fluid #1 @55μg/cm^2

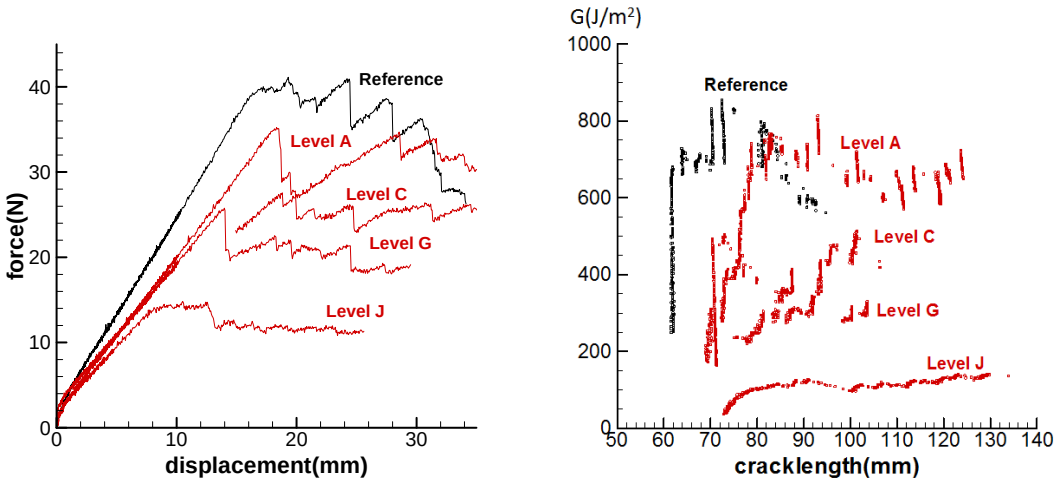

Figure 3.14 Force-displacement curve and fracture energy for the A, C, G, J level of hydraulic oil #1

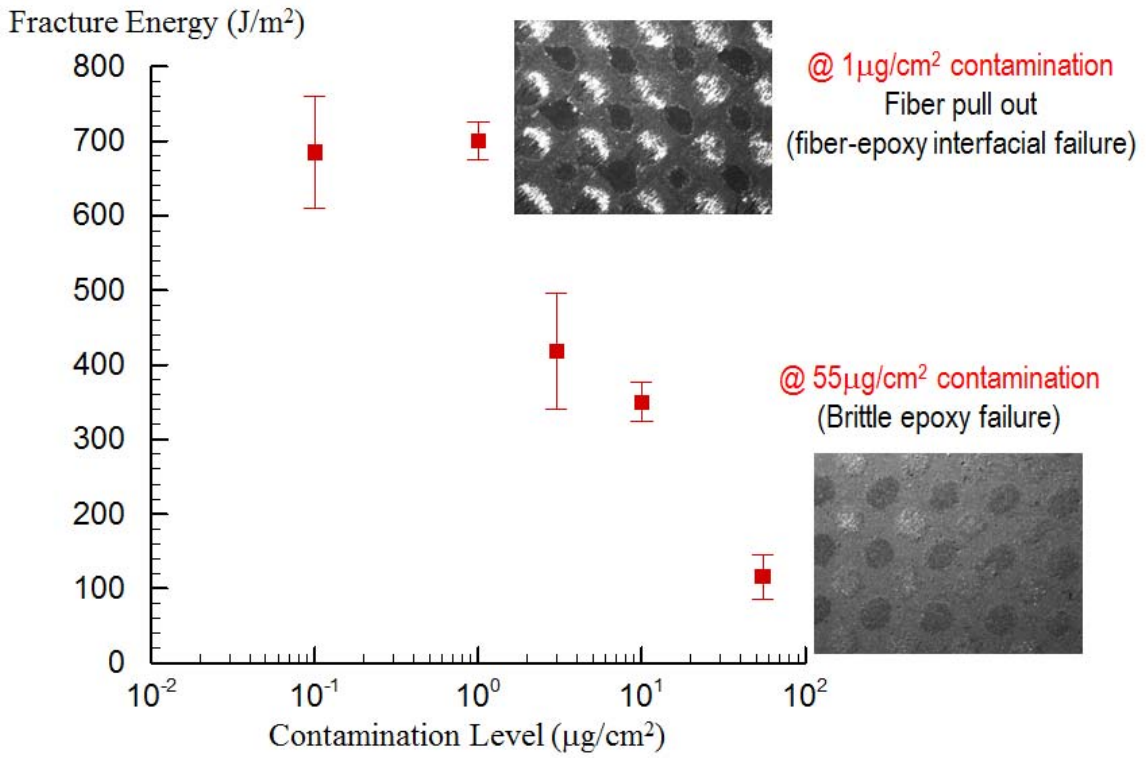

Figure 3.15 Role of #4 hydraulic oil contamination levels on adhesion strength for hydraulic fluid #1. The insert shows the transition from fiber pull-out to bond-line failure

Contamination Level	Ra(µm)	G (initiat.) (J/m²)	G (Steady S.) (J/m²)	Residual Strength
None	4.979	750	713	100%
1µg/cm²	4.839	675	700	98.18%
3µg/cm²	5.507	500	463	64.94%
10µg/cm²	4.128	310	350	49.09%
55µg/cm²	5.907	150	101	14.17%

Table 3.2 Summary of the fracture toughness measurements for different levels of hydraulic fluid #1

From the load-displacement curve in Figure 3.16, it is interesting to note that, at the beginning of the crack initiation, the shape of the curve has a transition from a round shape to a sharp drop. The rounded shape crack initiation indicates plastic deformation in the adhesive layer, because the force drops while the crack length stays the same. This transition shows that the plastic energy dissipation shrinks with increasing contamination level. The round-shape crack initiation indicates the presence of plastic flow. We can thus conclude that the contamination can not only decrease the surface energy but can also cause the plastic zone to shrink. Further examination of the fracture surface shows consistency with this conclusion.

Cohesive zone model proposed in chapter 2 is a phenomenological model for mathematically describing the relation between crack opening δ and the local stress σ during fracture process. Through this mathematical description, we can connect the contamination effect on the adhesive bondline to the macroscopic adhesive bonding toughness. Some researchers have studied the cohesive zone model with different shapes. Details of the cohesive zone shape will be discussed in Chapter 4. In this work, we utilize the triangular shape cohesive model to simulate the fracture process of adhesive bondline, which has three parameters. There are several methods to experimentally determine the cohesive parameters for cohesive zone model (Budiansky, 1988; Hutchinson, 1990; Cox, 1991; Bao, 1993). Since too many micro-mechanisms occur in the debonding procedure, it is more efficient to use phenomenological parameters. Kaute proposed a direct method to measure the cohesive law parameters for fiber cross-over (Kaute et al, 1993). He analyzed the fiber pull-out mechanism and determined the cohesive parameters by the properties of fibers, matrix and their

interface. Some researchers calculated the cohesive parameters through experimental measurement of crack growth resistance and the crack tip opening based on an application of the J integral (Suo, 1992; Sorensen, 1998). In this work, we will use another phenomenological method to determine the cohesive parameters for different contamination concentration levels.

Through the DCB experimental results, we have found that there are several critical parameters characterizing the fracture process, which is the stiffness of loading, crack initiation force and fracture toughness. The contamination concentration levels can affect two of the three parameters, which are the crack initiation force and the fracture toughness. The stiffness of loading is determined by the composite beams, not affected by the contamination. And the cohesive zone model has three parameters, which are the stiffness k, cohesive strength σ_0, cohesive energy γ_0. The cohesive stiffness can be determined by the stiffness of loading and the element size (Matous, 2008). And it is constant for different concentration of contamination. The effective fracture toughness of adhesively bonded joints can be predominantly affected by cohesive energy γ_0 (Hutchinson, 1992). And the cohesive strength is the maximum stress of cohesive law. The bonding stress will start to drop after the local stress reaches this limit. Thus the cohesive strength has influence on the crack initiation force. The two most important parameters (σ_0, γ_0) characterizing the cohesive zone model have two corresponding independence experimental parameters (crack initiation force and the effective fracture toughness). We can determine the cohesive parameters through the experimental data by estimation and data alignment.

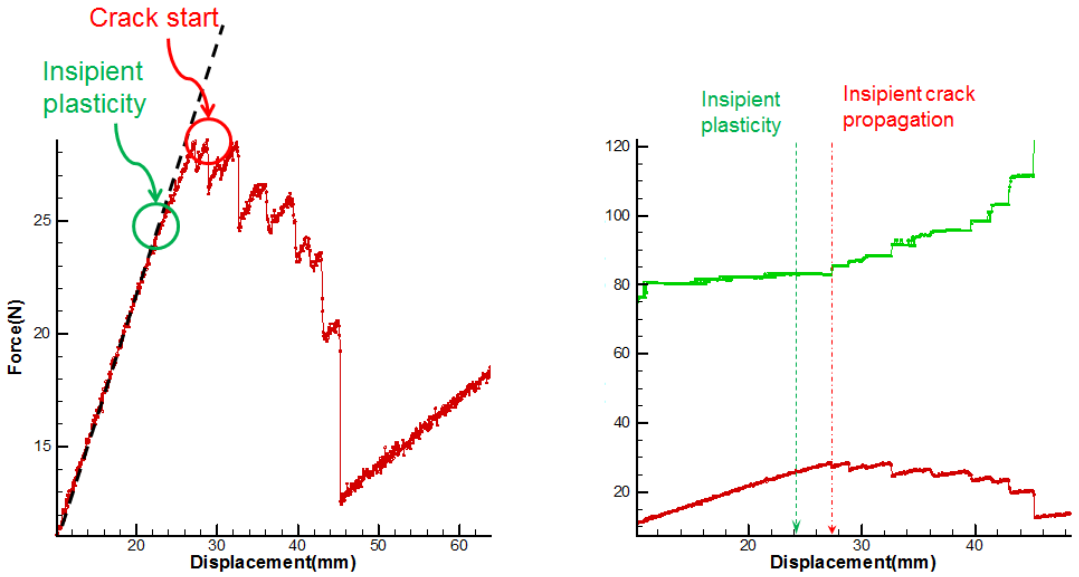

Figure 3.16 The experimentally measured (a) F-d curve and (b) the crack extension as a function of cross-head displacement for a sample exhibiting ductile crack tip initiation (#1 hydraulic oil @ 1μg/cm^2).

The fracture morphology screening of the composite surface pair is shown in Figures 3.17-3.23. Figure 3.18 and Figure 3.19 show typical ductile-fracture surfaces, while Figure 3.22 and Figure 3.23 show typical brittle-fracture surfaces. Compared to the brittle-fracture surface the ductile-fracture surface has larger areas of fibers, with sharp features. Also, the height difference of the ductile-fracture surface is high, indicating that the adhesive deformation is large during debonding. The brittle-fracture surface is much flatter and has fewer pull-out fibers. Fiber pull-out exhibits larger process zone size and higher resistance to fracture. This ductile-to-brittle fracture morphology transition is consistent with the hypothesis proposed in Chapter 1. In the ductile fracture, the interfacial adhesive strength is stronger than the yield stress, so the adhesive exhibits a large amount of plastic deformation before debonding. By applying a higher concentration level of contaminant, the interfacial adhesive strength is weakened. Once the interfacial adhesive strength drops below the yield

stress of the adhesive, plastic deformation of adhesive disappears. Thus, the contaminant, which has a hardening effect on the adhesive, has more chance to create catastrophic failure.

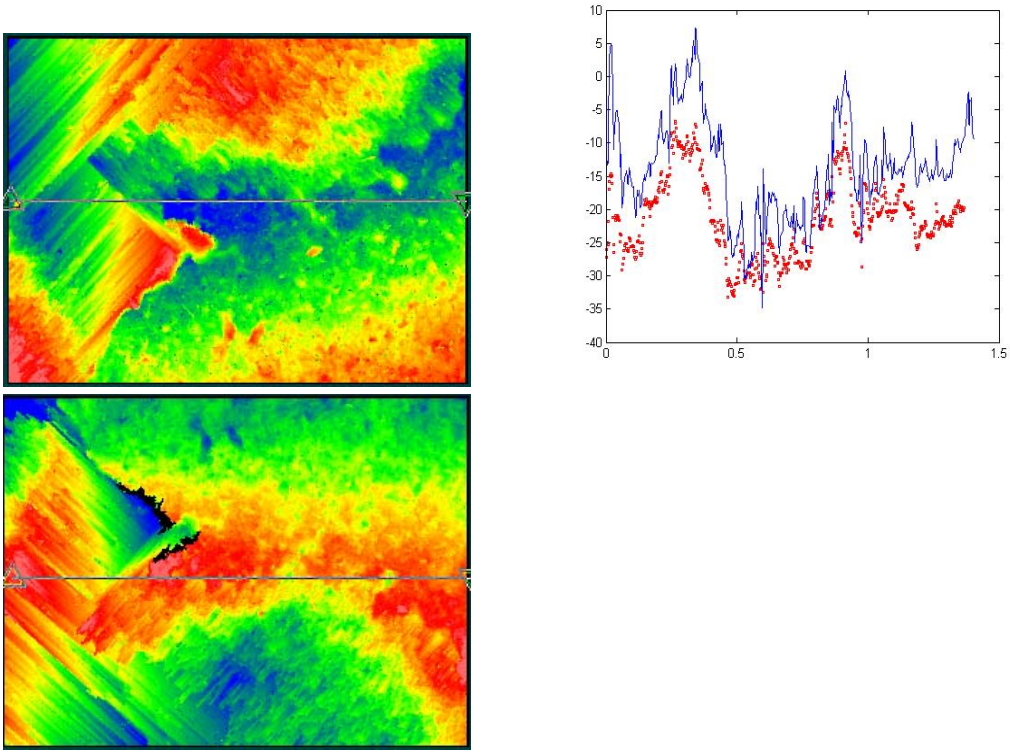

Figure 3.17 3D surface rendering of the pair of the fracture surfaces (a, b). (c) A 2D line profile from a corresponding line on both surfaces showing the extent of local plastic deformation (Reference uncontaminated sample).

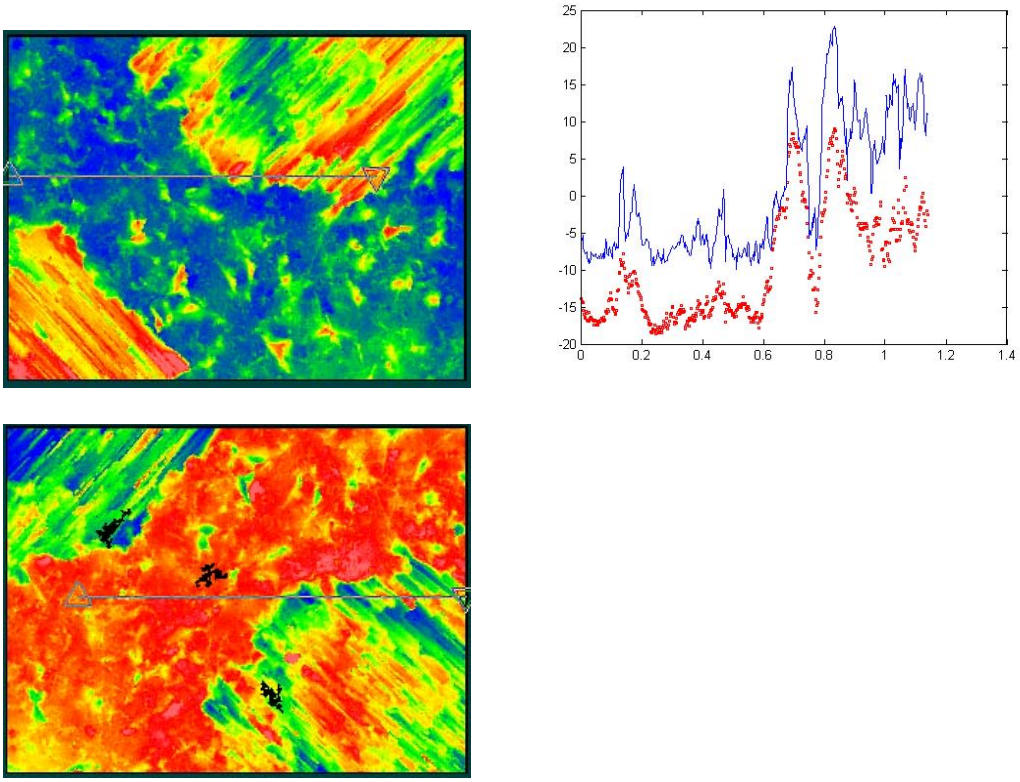

Figure 3.18 3D surface rendering of the pair of the fracture surfaces (a, b). (c) A 2D line profile from a corresponding line on both surfaces showing the extent of local plastic deformation (#1 Oil @ 1μg/cm^2 contaminated sample).

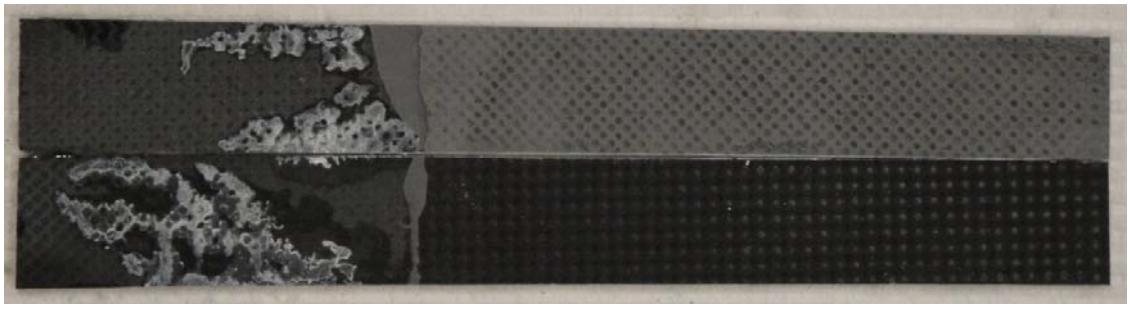

Figure 3.19 The DCB sample pair showing the final fracture surface (#1 Oil @ 1μg/cm^2 contaminated sample).

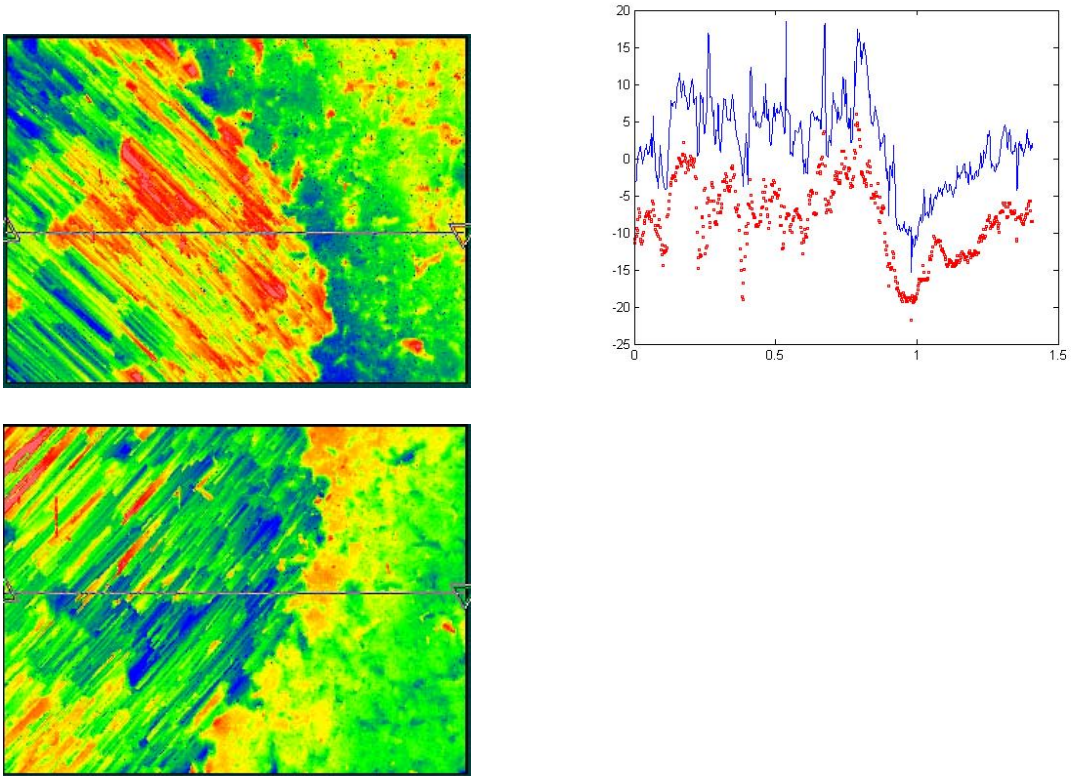

Figure 3.20 3D surface rendering of the pair of the fracture surfaces (a, b). (c) A 2D line profile from a corresponding line on both surfaces showing the reduction of local plastic deformation (#1 Oil @ 3μg/cm^2 contaminated sample).

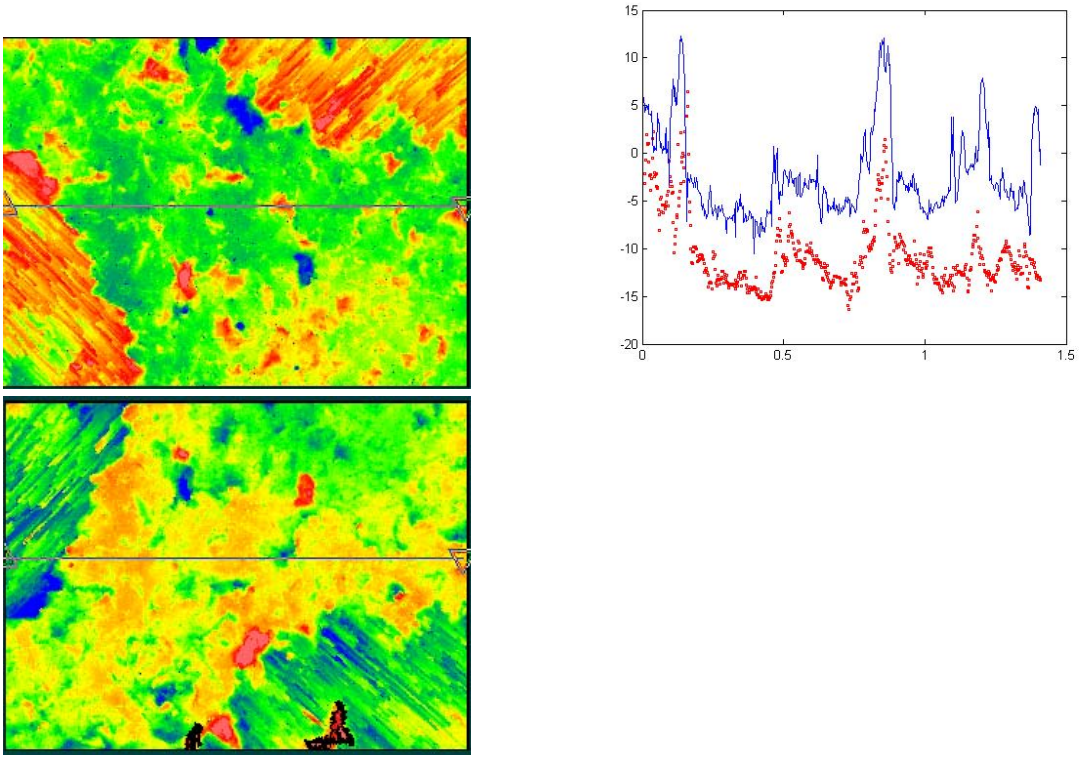

Figure 3.21 3D surface rendering of the pair of the fracture surfaces (a, b). (c) A 2D line profile from a corresponding line on both surfaces showing the reduction of local plastic deformation (#1 Oil @ 10μg/cm^2 contaminated sample).

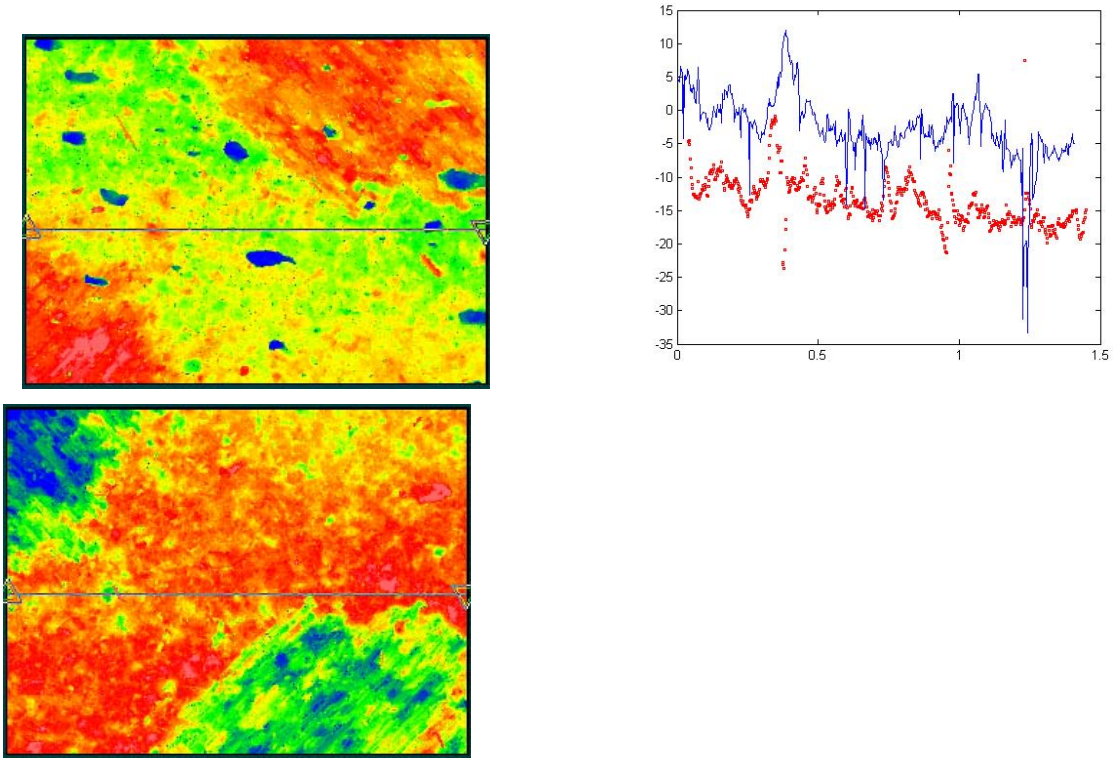

Figure 3.22 3D surface rendering of the pair of the fracture surfaces (a, b). (c) A 2D line profile from a corresponding line on both surfaces showing the reduction of local plastic deformation (#1 Oil @ 55µg/cm^2 contaminated sample).

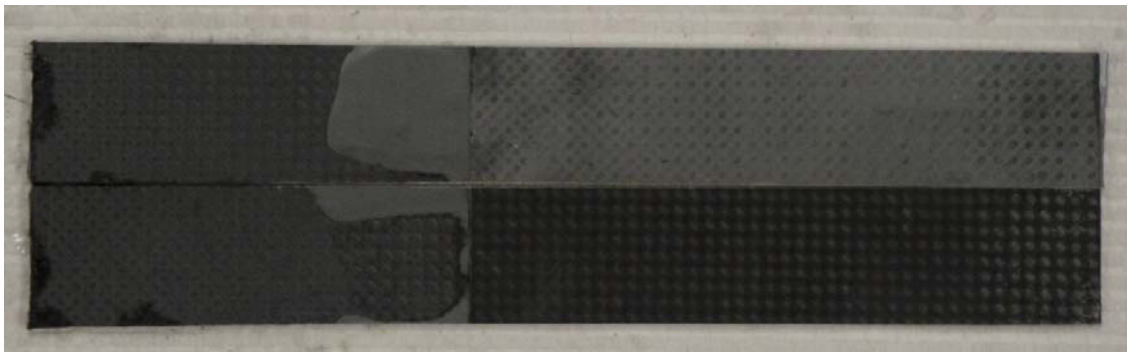

Figure 3.23 The DCB sample pair showing the final fracture surface (#1 Oil @ 55µg/cm^2 contaminated sample).

3.5 Conclusions

To achieving a reliable adhesive-bonding joint, it is very important to understand the effects of surface pretreatment and contamination concentration level effect on bonding surfaces of composite materials. In this work, a Mode I DCB test was used to measure the fracture toughness of the adhesive-bonding structures with different levels of contaminant. From these results, the sand-blasting to 4μm was found to be suitable for the current composite system (Hexcel IM7-G/8552) because it gives a high bonding strength with stable crack propagation. On the sand-blasted surface, different levels of contamination were applied. The contaminated adhesive bonding toughness was measured by mode-I DCB test. From the measured bond-line toughness and the fracture surface characterization, we conclude that a contaminant at level C is not adequate for achieving safe and reliable adhesive-bonding joints. The plastic zone size is considered to be the critical factor in achieving adhesive-bonding joint toughness. Applied contaminants contribute to decreased interfacial fracture energy. When the interfacial critical stress was weakened by these contaminants, the process zone shrunk. In mode I fracture, the plastic dissipation drops significantly because of the interfacial shielding effect, the primary effect leading to adhesive-bond strength degradation. The experimental results were further analyzed to find the cohesive zone parameters.

3.6 References

1. M.D. Banea and L.F.M. da Silva, Adhesively bonded joints in composite materials: An overview. *Journal of Materials Design and Applications*, **223**, 1, (2009).

2. R.L. Crane, G. Dillingham, Composite bond inspection. *Journal of Material Science*, **43**, 6682, (2008).

3. C. Jones. The chemistry of carbon fibre surfaces and its effect on interfacial phenomena in fibre/epoxy composite. *Composite Science and Technology*, **42**, 275-298, (1991).

4. J.W. Chin, J.P. Wightman. Surface characterization and adhesive bonding of toughened bismaleimide composite. *Composite Part A: Applied Science and Manufacturing*, **27A**, 419-428, (1996).

5. L.V. Smith, P. Pothakamuri, P.J. Vanvoast. The effect of surface treatment on the degradation of composite adhesives. JAMS Meeting, 2006.

6. R.G. Dillingham, B.R. Oakley, E.Dan-Jumbo, J. Baldwin, R. Keller, J. Magato. Suraface treatment and adhesive bonding techniques for repair of high temperature composite materials. *Journal of Composite Materials*, **0**, 1-7, (2013).

7. P. Davies, C. Courty, N. Xanthopoulos, H.J. Mathieu. Surface treatment for adhesive bonding of carbon fibre-poly(etherether ketone) composite. *Journal of Materials Science Letters*, **10**, 335-338, (1991).

8. M. Kanerva, O. Saarela. The peel ply surface treatment for adhesive bonding of composite: A review. *International Journal of Adhesion and Adhesives*, **43**, 60-69, (2013).

9. R. Bossi, R. Carlsen, F.J. Boerio, G. Dillingham, Composite surface preparation QA for bonding, SAMPE, (2005).

10. S. Mostovoy and E.J. Ripling, Fracture toughness of an epoxy system, *Journal of Applied Polymer Science*, **10**, 1351-1371 (1966).

11. R. Joseph, J.P. Bell, A.J. McEvily, and J.L. Liang, Fatigue crack growth in epoxy/aluminum and epoxy/steel joints, *The Journal of Adhesion*, **41**, 169-187 (1993).

12. M.D. Rakestraw, M.W. Taylor, D.A. Dillard, and T. Chang, Time dependent crack growth and loading rate effects on interfacial and cohesive fracture of adhesive joints, *The Journal of Adhesion*, **55**, 123-149 (1995).

13. N.B. Rao and A.R. Acharya, Evaluation of fracture energy G_{Ic} using a double cantilever beam fibre composite specimen, *Engineering Fracture Mechanics*, **51**, 317-322 (1995).

14. J.W. McBain and D.G. Hopkins, On adhesives and adhesive action, *The Journal of Physical Chemistry*, **29**, 188 (1924).

15. J.D. Venables, D.K. McNamara, J.M. Chen, T.S. Sun, and R.L. Hopping, Oxide morphologies on aluminum prepared for adhesive bonding, *Applications of Surface Science*, **3**, 88-98 (1979).

16. K.L. Mittal, Adhesion aspects of metallization of organic polymer surface, *Journal of Vacuum Science and Technology*, **13**, 19 (1976).

17. David, D. Sims, Weathering of polymers, *Applied Science Publishers*, London (1983).

18. W. Schnabel, Polymer degradation: principles and practical applications, *Hanser International*, New York (1981).

19. M. Zhang, S.E. Mason. The effects of contamination on the mechanical properties of carbon fibre reinforced epoxy composite materials. *Journal of Composite Materials*, **33**, 1363, (1999).

20. S.G. Kalarikkal, B.V. Sankar, P.G. Lfju. Effect of cryogenic temperature on the fracture toughness of graphite/epoxy composite. *Journal of Engineering Materials and Technology*, **128**, 151-157, (2006).

21. I.A. Ashcroft, M.M. Abdel-Wahab, A.D. Crocombe, D.J. Hughes, S.J. Shaw. The effect of environment on the fatigue of bonded composite joints. *Composite: Part A*, **32**, 45-58, (2001).

22. V. Shenoy, I.A. Ashcroft, G.W. Critchlow, A.D. Crocombe, M.M. Abdel-Wahab. Strength wearout of adhesively bonded joints under constant amplitude fatigue. *International Journal of Fatigue*, **31**, 820-830, (2009).

23. S. Erpolat, I.A. Ashcroft, A.D. Crocombe, M.M. Abdel-Wahab. A study of adhesively bonded joints subjected to constant and variable amplitude fatigue. *International Journal of Fatigue*, **26**, 1189-1196, (2004).

24. S. Erpolat, I.A. Ashcroft, A.D. Crocombe, M.M. Abdel-Wahab. Fatigue crack growth acceleration due to intermittent overstressing in adhesively bonded CFRP joints. *Composite: Part A*, **35**, 1175-1183, (2004).

25. M.Y. Al-Mandil, H.S. Khalil, M.H. Baluch and A.K. Azad. Performance of epoxy-repaired concrete under thermal cycling. *Cement & Concrete Composites*, **12**, 47-52, (1990).

26. B.L. Lee, M.W. Holl. Effect of moisture and thermal cycling on in-plane shear properties of graphite fibre-reinforced cyanate ester resin composite. *Composite Part A*, **27A**, 1015-1022, (1996).

27. ASTM Standard D5528, Test method for mode I interlaminar fracture toughness of unidirectional fiber-reinforced polymer matrix composite, Annual Book of ASTM Standards, **15.3**. ASTM International, W. Conshohocken, PA.

28. B. Budiansky, J.C. Amazigo, and A.G. Evans, Small scale crack bridging and the fracture toughness of particulate reinforced ceramics, *Journal of the Mechanics and Physics of Solids*, **36**, 167 (1988).

29. J.W. Hutchinson and H.M. Jensen, Models of fiber debonding and pullout in brittle composites with friction, *Mechanics of Materials*, **9**, 139 (1990).

30. B.N. Cox and D.B. Marshall, The determination of crack bridging forces, *International Journal of Fracture*, **49**, 159 (1991).

31. G. Bao and Y. Song, Crack bridging for fiber composites with slip dependent interfaces, *Journal of the mechanics and Physics of Solids*, **41**, 1425 (1993).

32. D.A.W. Kaute, H.R. Shercliff and M.F. Ashby, Delamination, fiber bridging and toughness of ceramic matrix composites, *Acta Metallurgica et Materialia*, **41**, 1959-1970 (1993).

33. Z. Suo, G. Bao, B. Fan, Delamination R-curve phenomena due to damage, *Journal of the Mechanics and Physics of Solids*, **40**, 1 (1992).

34. B.F. Sorensen and T.K. Jacobsen, Large scale bridging in composites: R-curves and bridging laws, *Composites Part A*, **29A**, 1443-1451 (1998).

35. K. Matous, M.G. Kulkarni, P.H. Geubelle, Multiscale cohesive failure modeling of heterogeneous adhesives, *Journal of the Mechanics and Physics of Solids*, **56**, 1511-1533 (2008).

CHAPTER 4 FINITE ELEMENT ANALYSIS MODELING DOUBLE CANDTILEVER BEAM TEST

4.1 Introduction

From the continuum viewpoint, fracture is the formation of new surfaces in the body. Linear elastic fracture mechanics has been proven to be useful for brittle fracture. Energy-based failure theory introduced by Griffith (1921) formed the foundation for linear elastic fracture mechanics. Irwin observed that the stress field near crack tip in isotropic linear elastic materials is similar for all geometry and loading conditions (1957). The crack tip opening stress and displacement field were deduced and connected to the fracture energy. However, in practice, the adhesively bonded joints undergo non-linear phenomena, for example plasticity. Further, the linear elastic fracture mechanics has an intrinsic restriction, small scale yielding, which is not met in the fracture process of adhesively bonded joints. The crack propagation with these pre-existing flaws has multiple complex damage mechanisms (Fleck 1992). The non-linear cohesive zone mechanics was first presented by Dugdale (1960) and Barenblatt (1962) for avoiding the inconsistency of infinite stresses at the symmetric crack tip in homogeneous isotropic materials. Recent developments in finite-element analysis have led to widespread numerical use of the cohesive zone model (Needleman, 1994). Cohesive-zone models have successfully characterized fracture failure in metals, polymers, and crystals (Song et al, 2006; Kafkalidis et al, 2002; Hua et al, 2008).

The key idea of the cohesive-zone model is introducing a finite-length cohesive area as the interface to avoid singularity by modeling the crack tip as a finite cohesive zone. The cohesive-zone model has been used to study both linear fracture mechanics and non-linear fracture mechanics, especially in laminated composite (Fleck et al, 1991). It has been proven that the parameters of the cohesive zone model can be determined by fracture experiments (Xu et al, 1994).

Previous work has given a detailed investigation of the contamination effect on bondline integrity based on experimental double-cantilever beam tests and nanoindentation tests (Chapters 2 and 3). Experimental data has shown that hydraulic oils can change the mechanical properties of the adhesive and the interface strength. The contamination applied to a bondline can degrade its strength to 20% of its original strength, as shown in in Figures 2.6 and 2.7.

In this work, cohesive zone model was used to investigate the detailed fracture process. The aim of this study is to give a full assessment with respect to the effect of bond-line properties on total fracture strength. In particular, the properties are divided into three groups, i.e., the intrinsic bondline strength, the properties of the adhesive, and the thickness of the interfacial adhesive. The finite-element analysis package ABAQUS was used to model the double cantilever beam test and the delamination process was simulated using a cohesive-zone model. The parameters in the cohesive-zone model, including the modulus and yield strength of the adhesive, were provided from a complete set of experiments (Chapter 2). The

total effective fracture energy Gc was calculated and equated to the intrinsic bond-line toughness plus the plastic dissipation energy.

4.2 Simulation Configuration of DCB Samples

4.2.1 Modeling

The double-cantilever beam was simulated as a 2-D model and the composite beams were modeled as linear elastic materials with four-node plain-strain shell elements (Figure 4.1). The modulus of the composite is 43.7GPa as calculated from a three-point bending test. To simplify the simulation, the adhesive was modeled as an isotropic material. Considering that the size of the process zone is much larger than the fiber size and filler size, this simplification is reasonable.

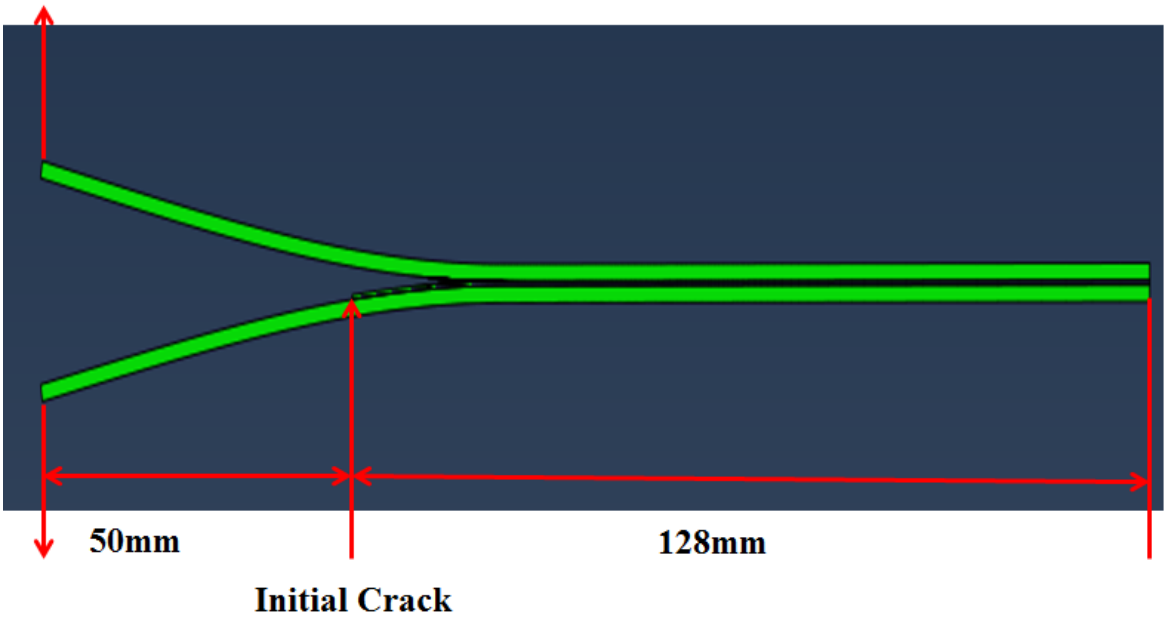

Figure 4.1 The double cantilever beam model diagram in ABAQUS

4.2.2 The Cohesive Zone Model

The cohesive zone model is used to mathematically describe the debonding process in this work. The fundamental issue for simulating the fracture process is the characterization of cohesive interaction between traction and body strain. Cohesive law can be classified by either non-potential based models (Yang, 2001; Zhang, 2005) or potential based models (Needleman, 1987; Beltz and Rice, 1991; Tvergaard and Hutchinson, 1993). Considering the physical image of void nucleation from atomistic point of view, atomic bonds at certain points with material defects undergo significant stretching, which leads to atomic decohesion and formation of new surface. At the stage of atomic debonding, the first derivative of the fracture energy potential provides the traction on the surface. And the second derivative of the energy potential provides the material properties (i.e. stiffness). Several potential functions have been studied to simulate the fracture process. A polynomial potential function was proposed to simulate void nucleation (Needleman, 1987). The exponential potential function was proposed for large shear displacement by Beltz and Rice (1991). Non-potential based models are developed for simplicity. A trapezoidal-shape cohesive law was utilized to simulate mix-mode fracture by Yang (2001). Bilinear cohesive law was utilized for analyze the homogeneous materials with dynamic failure (Zhang and Paulino, 2005; Liljedhal et al, 2006).

To simulate crack growth in the adhesive bondline, the bilinear cohesive surface element was applied between the adhesive layer and the composite layer. Previous works have shown that the bilinear cohesive zone model is able to bridge the gap between craze micromechanics and the role of crazing in polymer fracture (Tijssens et al, 2000; Estevez et

al, 2000). This assumes that the singular crack-tip region can be replaced by a zone in which non-linear phenomena occur. The fracture process in the cohesive zone is characterized by the cohesive law that relates stress and displacement. The constitutive relationship of this criterion is shown in Figure 2.11.

The constitutive curve describes failure behavior of the cohesive zone. The area under the constitutive curve is the intrinsic fracture energy of the cohesive element. As the displacement of the elements increase, once it approaches δ_0 the stress reaches maximum σ_0 and then begins to drop and failure is initiated. When the displacement reaches δ_c, the cohesive bond completely breaks. The bilinear traction separation law is determined by three independent parameters: k, σ_0, Γ. There are several methods to determine the cohesive parameters. Sorensen and Jacobsen determined the cohesive parameters by differentiating the J-integral with respect to the end-opening displacement (2003). Anderson and Stigh have studied a similar method (2004). Yang et al applied a 3-point bending test and showed that the local strain at the crack tip was 40% (2001). Thus, the cohesive stress was chosen corresponding to the 40% strain. Li et al have shown that the two parameters of cohesive model can be determined from experimental results (2005). First the cohesive energy were determined by the correlation of the fracture energy that relatively independent of the cohesive stress. Second the cohesive stress was varied until the whole load-displacement curve was consistent with the experimental results. In this work, we will apply an approach similar to Li's approach for choosing the cohesive parameters. The stiffness k of the cohesive behavior is calculated from modulus $k = Et$, where t is the element size, E is the modulus of adhesive. The cohesive energy was determined by the correlation of the fracture energy from

DCB test. Then the cohesive stress was determined by the correlation of the initiation force from DCB test.

Another critical condition for steady cohesive surface simulation is element size. Too small an element size (compared to $\delta_{c)}$) contributes to a distortion of the cohesive element, because the cohesive surface element has no stiffness in the lateral direction. If the element size is too large, the stress would concentrate on only a single element. That would lead to a bad gradient of the stress distribution and poor accuracy. Additionally, too large an element would enlarge the process zone size and cause it to be overestimated. The element size in this work is 0.083mm.

4.3 Simulation Results and Discussions

4.3.1 Modeling Parameters

There are many parameters, including bulk material properties, geometric dimensions and cohesive parameters. The leading parameters of the fracture process simulation relate to the shape of the cohesive law, and include the stiffness k, the maximum stress $\sigma_{0,}$ and the intrinsic fracture energy Γ. The mechanical properties and the thickness of the epoxy layer have a secondary role in determining the total fracture energy. In this work, these three sets of simulations were individually studied to investigate their effects on the steady-state fracture energy.

4.3.2 Cohesive Surface Element Parameters

Three independent parameters: stiffness, maximum stress, and intrinsic fracture energy, determine cohesive surface zone behavior. Various studies have found that the maximum stress σ_0 and the stiffness K have only a limited effect on cohesive behavior (Tvergaared et al, 1992). However, we have found that they do have some significant influence on the convergence problem. From our experiments, the results demonstrated that contaminations could decrease the intrinsic fracture energy and have some effect on the modulus. Thus, we simultaneously decreased the maximum stress and the intrinsic fracture energy to keep the unloading traction ratio constant, as shown in Figure 4.3.

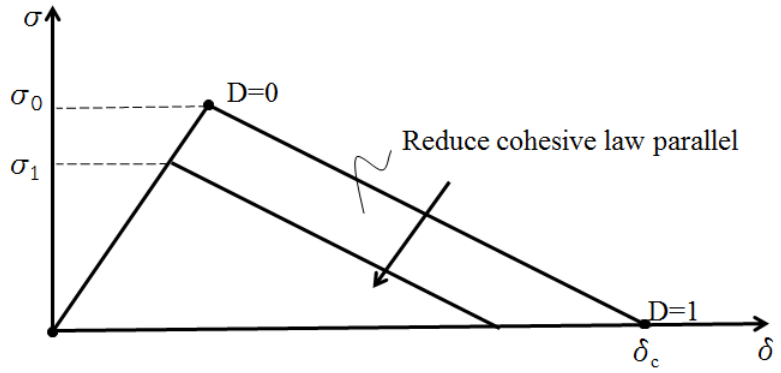

Figure 4.2 The method of changing the traction separation law parameters to account for different degradation level.

To investigate the effect of cohesive behavior on the macroscopic fracture process, five models were examined with constant geometry and material properties. In this set of simulations, the yield stress of epoxy was 69Mpa and the thickness of the epoxy layer was 0.4mm. Previous DCB work showed that, at a very high level of contamination, the measured

bond-line toughness is about 100J/m^2. The cohesive parameters were determined by the method described above and shown in Table 4.1.

	Model 1-1	Model 1-2	Model 1-3	Model 1-4	Model 1-5
Stiffness k	3e6	3e6	3e6	3e6	3e6
Maximum stress σ_0 (MPa)	135	130	114.5	76	60
Intrinsic fracture energy G_i (J/m^2)	250	230	180	80	50

Table 4.1 The cohesive surface law parameters for different realizations.

The fracture energy was defined to occur when the total energy release rate reached a plateau. The sensitivity of the macroscopic fracture process to intrinsic cohesive behavior was clear, as shown in Figure 4.4. The plastic dissipation in the total fracture energy is $G_p=G_t-G_i$. From Figure 4.5, it can be seen that plastic dissipation is the predominant effect determining the total fracture toughness, and the plastic energy is sensitive to the intrinsic fracture energy because the plastic zone size is monotonically related to the intrinsic fracture energy. Further examination of the plastic zone showed that the plastic zone size in model 1-1 is 0.06mm, while it deceases almost to zero at model 1-5. Figure 4.7 and Figure 4.8 show how the plastic zone size change is affected by the interfacial parameters.

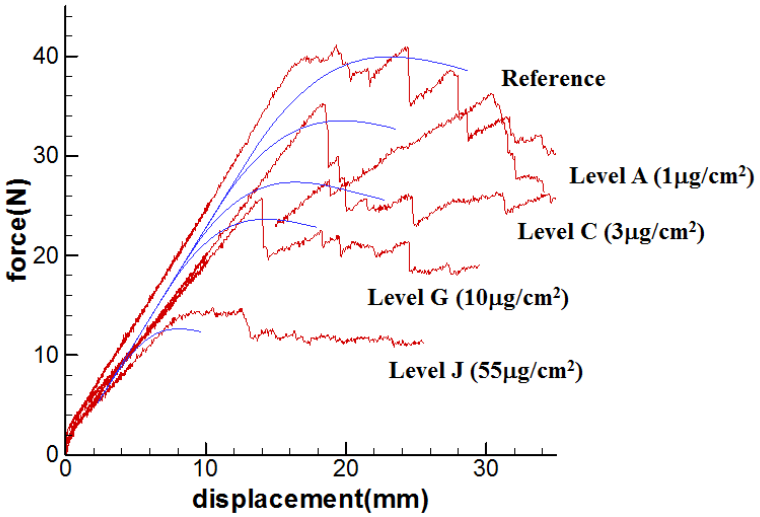

Figure 4.3 The comparison between FEM results with the experimental data at different levels of contamination (red-#1 Hydraulic oil), blue line is FEM results, and red line is DCB measured data.

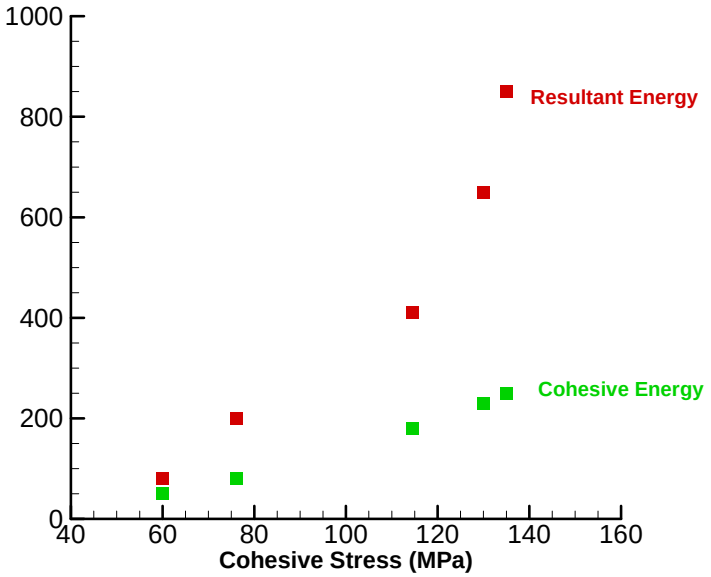

Figure 4.4 FEM results of the fracture energy for different level of cohesive surface element.

The simulation results were rationalized with the DCB results in Chapter 3. The adhesive bondline toughness at each concentration level was fitting to the modeling bondline toughness. Then, the simulation results was plotted according to the log of the contaminates concentration levels in Figure 4.6. It shows the trend of the adhesive bondline toughness with the contaminates concentration levels. The interfacial shielding effect was quantitatively connected with the contaminates concentration level. The log of contaminates concentration level has an almost linear relation with the interfacial strength decrease. This weakening effect of contaminates on the interfacial bonding strength further decrease the plastic zone size and leads to the plastic work decrease during debonding.

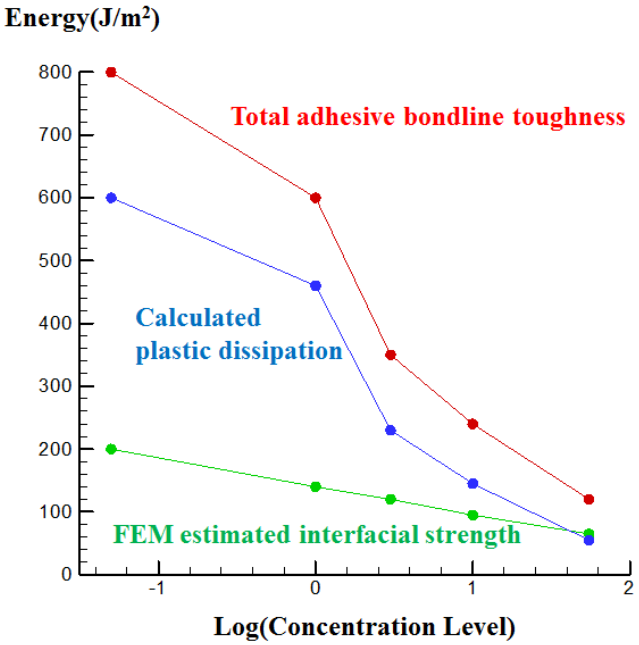

Figure 4.5 The deduced plastic dissipation from DCB experiments and numerical results.

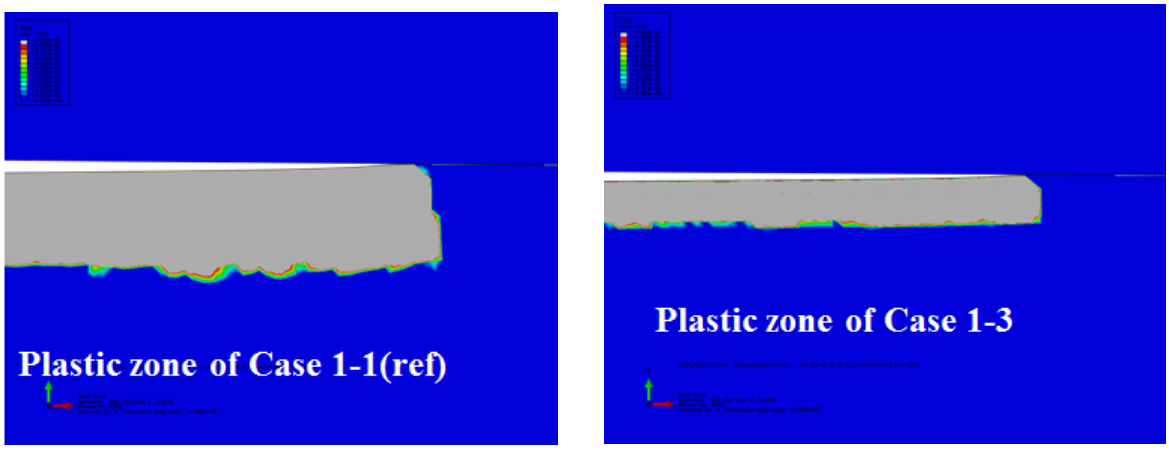

Figure 4.6 The plastic zones of different interfacial strength (grey part)

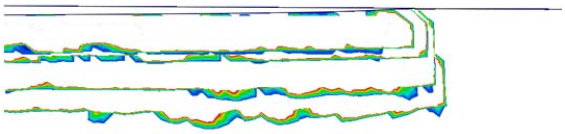

Figure 4.7 The evolution of plastic zone size with decreasing cohesive energy

From these results, we concluded that hydraulic oil has a degradation effect on the intrinsic fracture toughness of the bondline. According to this set of simulations, the degraded intrinsic fracture toughness could significantly shrink the plastic zone size, so the effective bond-line toughness is sensitive to contamination-induced degradation.

4.3.3 Bulk Material Properties

From nanoindentation experiments we have also observed that contamination has some hardening or softening effects on the modulus and hardness of the adhesive matrix

(Chapter 2). The hardening effect of the epoxy could shrink the process zone because the process zone size is determined by $\frac{\Gamma}{\sigma_y}$. However, a prediction based on this assumption produces a large discrepancy with respect to the DCB-measured bond-line toughness. A detailed simulation study regarding the effect of material properties is required to understand material degradation caused by contamination. From experiments, the modulus and yield stress of the adhesive matrix are 4.3GPa and 69MPa. The material properties used in simulations are shown in Tables 4.2 and 4.3. The cohesive element parameters are the same as for the reference state.

	Model 2-1	Model 2-2	Model 1-1	Model 2-4	Model 2-5
Modulus (MPa)	4300	4300	4300	4300	4300
Yield stress (MPa)	51.75	55.2	69	86.25	103.5

Table 4.2 The bulk material property

	Model 3-1	Model 3-2	Model 1-1	Model 3-4	Model 3-5
Modulus (MPa)	2150	3225	4300	5375	8600
Yield stress (MPa)	69	69	69	69	69

Table 4.3 The bulk material property

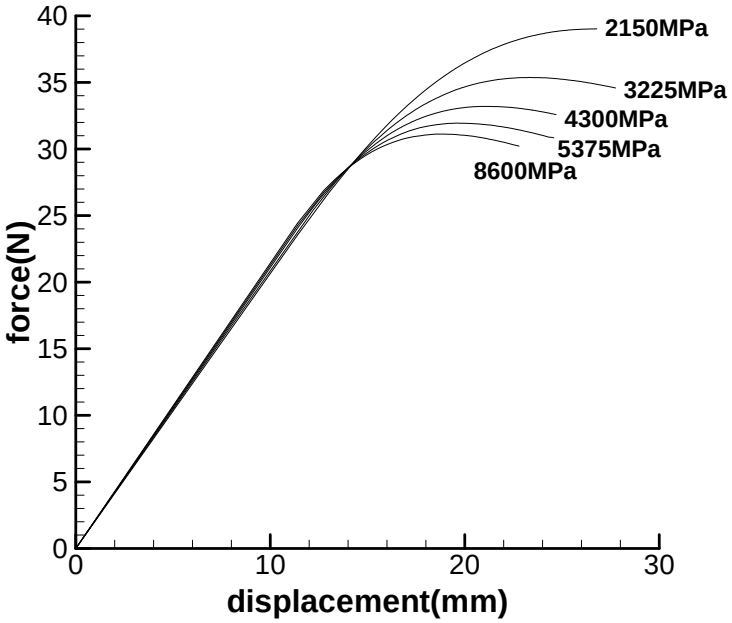

Figure 4.8 The load-displacement curve of the FEM for different level of adhesive modulus

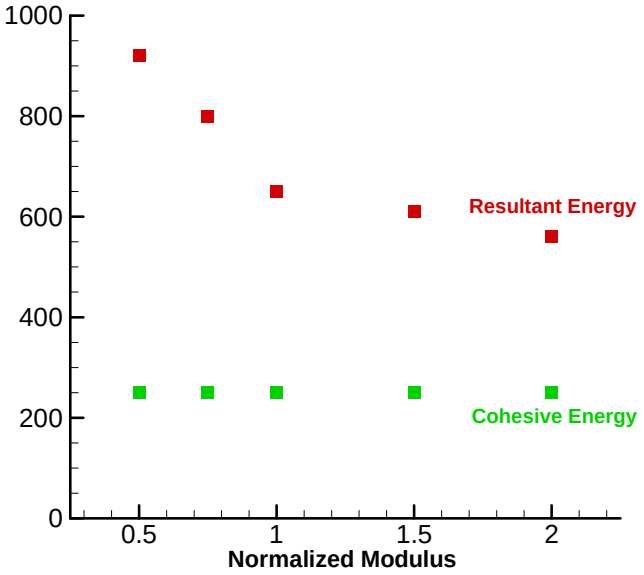

Figure 4.9 The resultant fracture energy versus normalized modulus

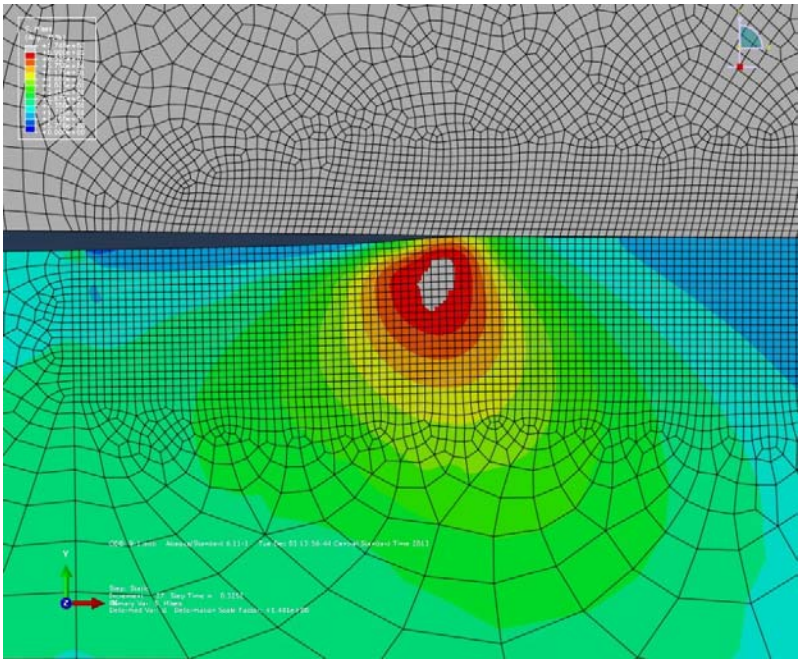

Figure 4.10 The stress distribution around the crack tip and the plastic zone (grey part) in the reference state (model 1-1)

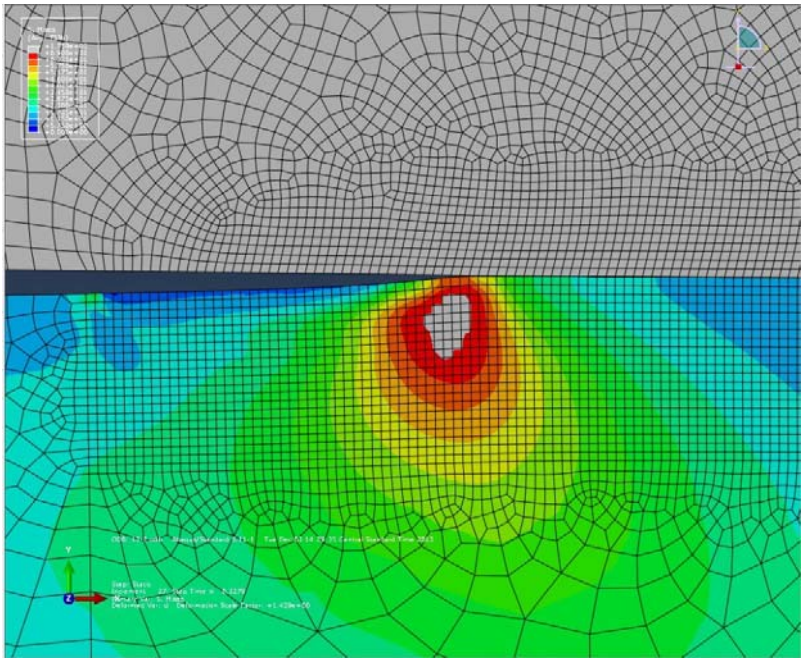

Figure 4.11 The stress distribution around the crack tip and the plastic zone (grey part) of model 3-2 (0.8E)

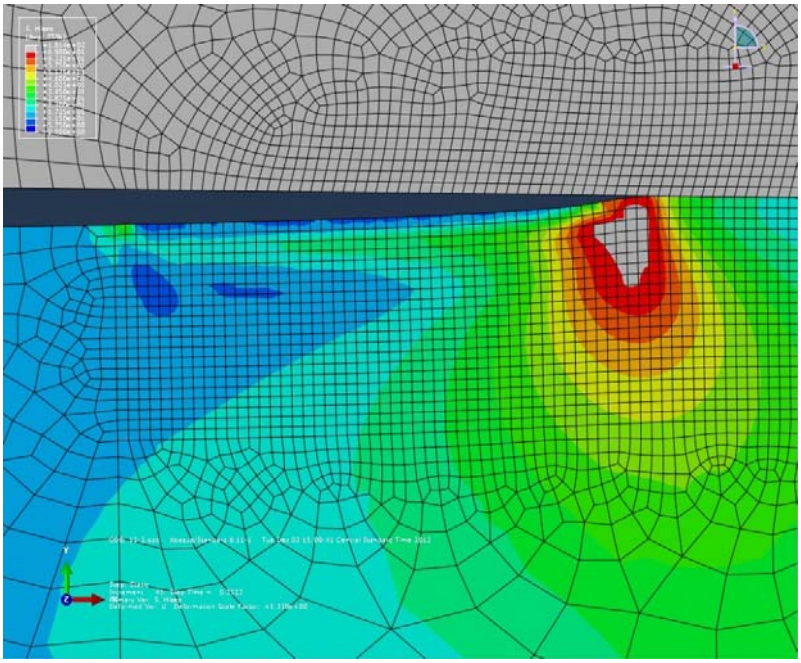

Figure 4.12 The stress distribution around the crack tip and the plastic zone (grey part) of Model 3-1 (0.5E)

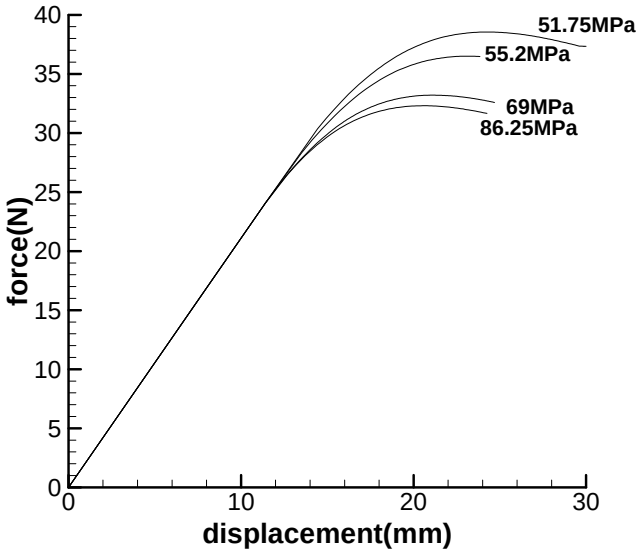

Figure 4.13 The load-displacement curve of the FEM for different level of adhesive yield stress

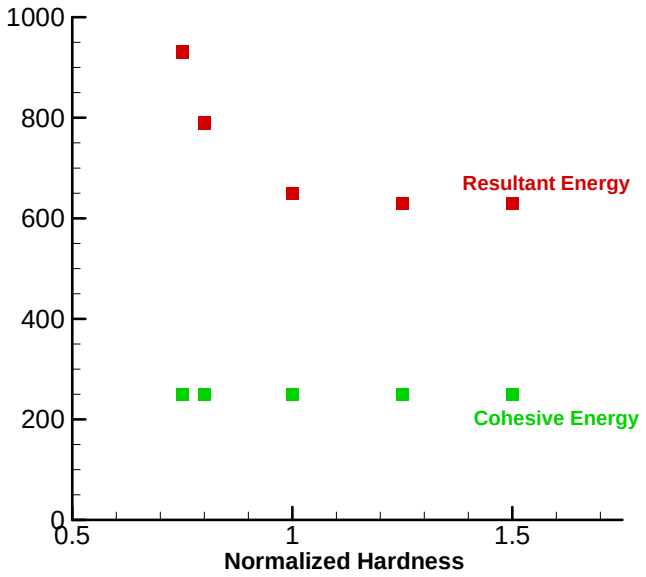

Figure 4.14 The resultant fracture energy versus normalized hardness

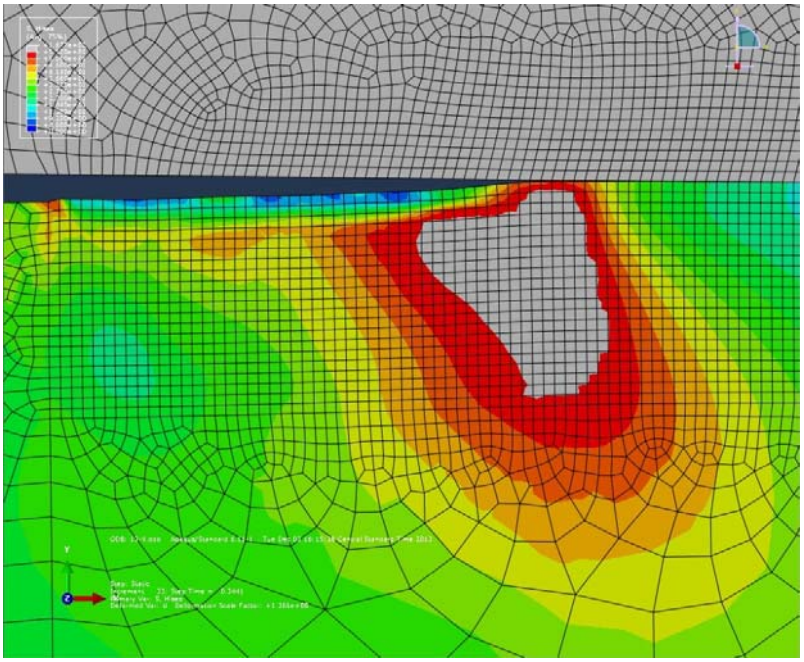

Figure 4.15 The stress distribution around the crack tip and the plastic zone (grey part) of model 2-2 ($0.8\sigma_Y$)

From the results shown in Figures 4.9-4.16, it is clear that the total fracture process is much more sensitive to a change of yield stress than the modulus. From Figure 11,16, it is obvious that the plastic zone size expand significantly by 20% decrease of yield stress. On the other hand, from Figure 11-13, the plastic zone size expands a little by even 50% decrease of modulus. Such plastic zone size change determines the plastic dissipation energy, which is the comparative large part of the total fracture energy. This is reasonable because in an elastic-plastic fracture, the process zone size determined by $\frac{\Gamma}{\sigma_y}$ rather than by $\frac{\Gamma}{E}$. The shape of the plastic zone also changes with the amplitude by the change of modulus and yield stress. It is interesting to note that the yield stress has a larger-value plateau. At a specific level, the total fracture toughness is insensitive to a change in the yield stress. This behavior has been explained by Suo using an SSV model (Suo et al, 1993).

4.3.4 Adhesive Thickness

Because the adhesive layer thickness is only 0.4mm and the composite panel is much stiffer than the epoxy, the composite panel has a constraining effect on the stress state in the adhesive layer. Thus, the effect of thickness is important for understanding the global fracture process. It can be noted that the mesh size should be proportional to remain mesh-independent while reducing thickness. The thicknesses of three models are shown in Table 4.4. Other parameters are the same as those in the reference state.

	Model 1-1	Model 4-2	Model 4-3
Thickness of epoxy (μm)	400	200	100
Mesh size (μm)	10	5	2

Table 4.4 The thickness and mesh size of three cases

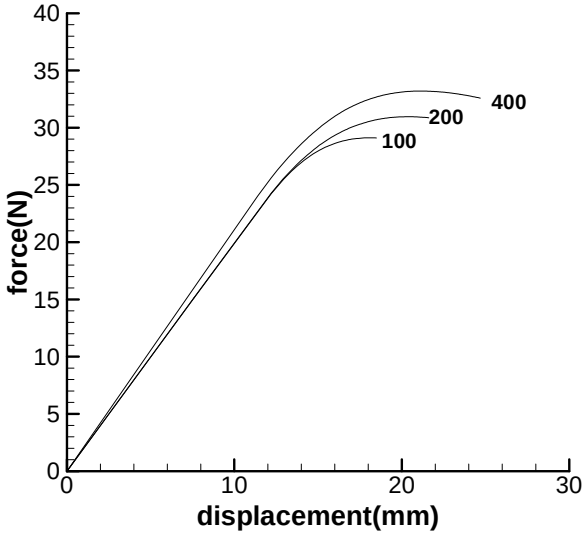

Figure 4.16 The load-displacement curve of the FEM for different thickness (μm)

From these results, it is clear that the effective bond-line fracture toughness is sensitive to the adhesive-layer thickness. This is expected because the process zone is compressed by the reduced thickness. Further examination on the residual strain on the epoxy layer shows that the both the magnitudes and thicknesses of the residual strain in these three cases decrease with thickness, as shown in Figures 4.14 and 4.15. The extracted residual strain along the vertical height of the epoxy layer is shown in Figure 4.16. Note that the residual strain on the top surface of the adhesive is zero, proving that the stiffer composite panel has a shielding effect on the stress state in the adhesive layer.

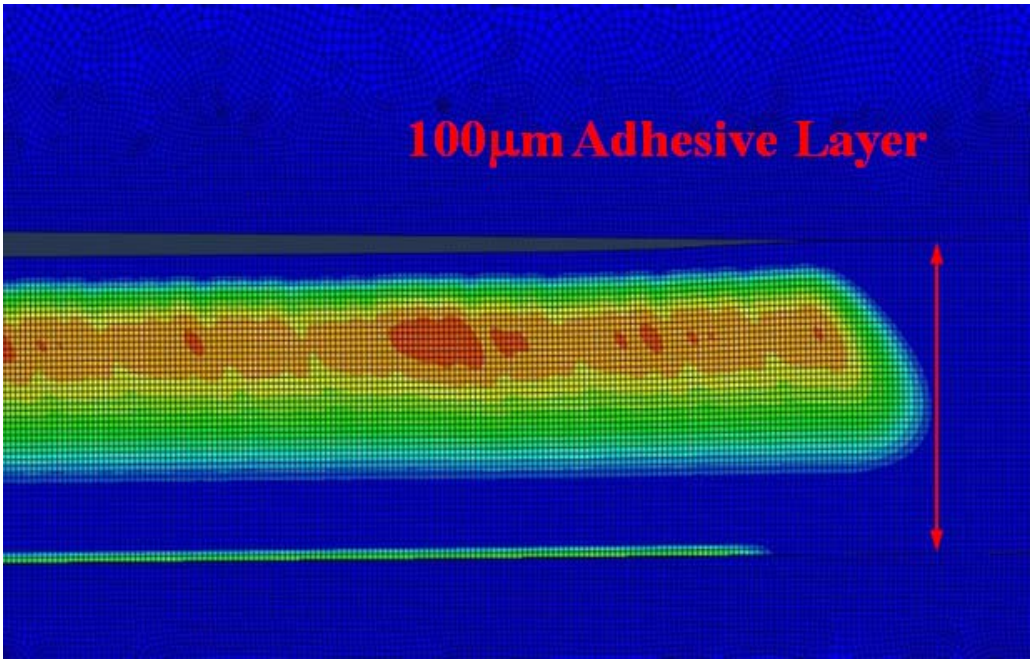

Figure 4.17 The plastic strain in 100μm adhesive layer (color wake)

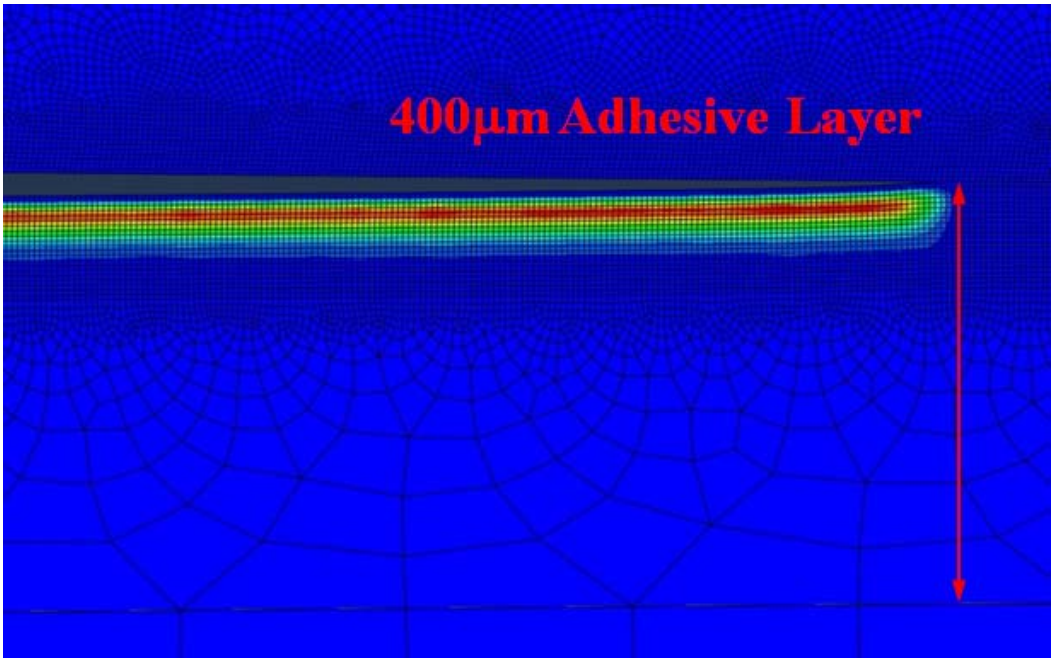

Figure 4.18 The plastic strain in 400μm adhesive layer (color wake)

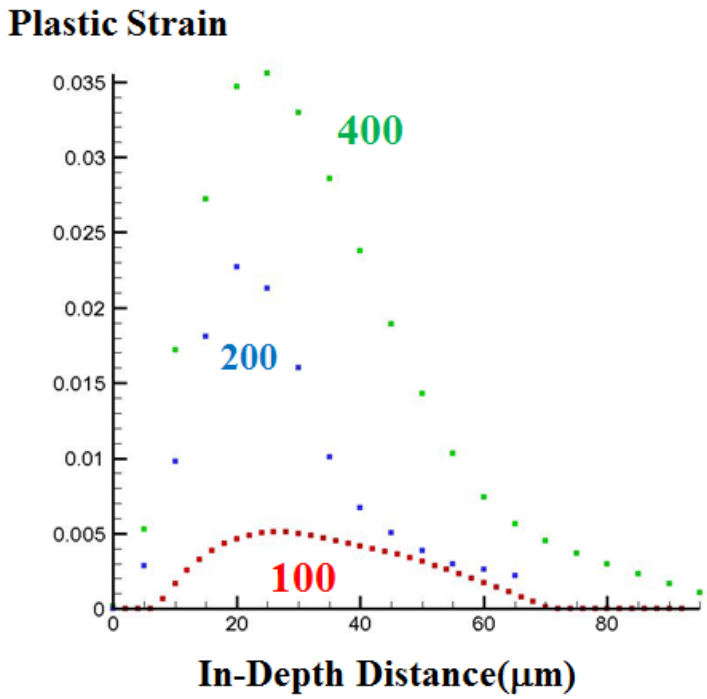

Figure 4.19 The plastic strain distribution vertical to the adhesive layer

In this work, cohesive surface model was used to study the bondline properties in an adhesive bonding double cantilever beam. The sensitivity of bondline toughness to the bondline properties was examined. The effects of the intrinsic fracture energy, the bulk material properties and the thickness of the epoxy layer were carefully studied to understand their contribution to the plastic dissipation by three sets of FEM simulations. The plastic energy dissipation is the predominant part in the effective bondline fracture energy in this contaminates-adhesive bondline delamination. In addition, cohesive parameters predicted fracture process was compared with the load-displacement and fracture date measured from experiments in Figure 4.17. The trend of the simulations results has good agreement with that of experiments.

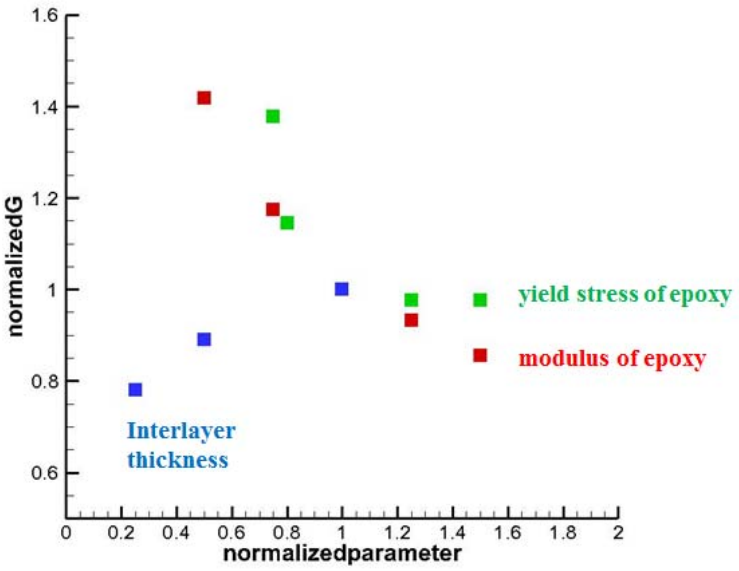

Figure 4.20 The normalized parameters versus the normalized resultant fracture energy

4.4 References

1. A.A. Griffith, The phenomena of ruptures and flow in solids, *Philosophical Transactions of the Royal Society of London*, **221A**, 163-198 (1921).

2. G. Irwin, Analysis of stresses and strains near the end of a crack traversing a plate, *Journal of Applied Mechanics*, **24**, 361-364 (1957).

3. A.R. Akisanya, N.A. Fleck, Brittle fracture of adhesive joints, *International Journal of Fracture*, **58**, 93-114 (1992).

4. G.I. Barenblatt, The mathematical theory of equilibrium cracks in brittle fracture, *Advanced in Applied Mechanics*, **7**, 55-129 (1962).

5. S.H. Song, G.H. Paulino, W.G. Buttlar, Simulation of crack propagation in asphalt concrete using an intrinsic cohesive zone model, *Journal of Engineering Mechanics*, **132**, 1215-1223 (2006).

6. Higgins, Adhesive bonding of aircraft structures, *International Journal of Adhesion & Adhesives*, **20**, 367-376, (2000).

7. H. Chai, Fracture work of thin bondline adhesive joints, *Journal of Materials Science Letters*, **7**, 399-401, (1988).

8. D.S. Dugdale, Yielding of steel sheets containing slits, *Journal of the Mechanics and Physics of Solids*, **8**, 100-104, (1960).

9. A. Needleman, An analysis decohesion along an imperfect interface, *International Journal of Fracture*, **42**, 21-40, (1990).

10. V. Tvergaard and J.W. Hutchinson, The influence of plasticity on mixed mode interface toughness, *Journal of the Mechanics and Physics of Solids*, **41**, 1119-1135, (1993).

11. V. Tvergaard and J.W. Hutchinson, On the toughness of ductile adhesive joints, *Journal of the Mechanics and Physics of Solids*, **44**, 789-800, (1996).

12. M.S. Kafkalidis, M.D. Thouless, The effects of geometry and material properties on the fracture of single lap-shear joints, *International Journal of Solids and Structures*, **17**, 4367-4383, (2002).

13. Y. Hua, A.D. Crocombe, M.A. Wahab, I.A. Ashcroft, Continuum damage modeling of environmental degradation in joints bonded with EA9321 epoxy adhesive, *International Journal of Adhesion & Adhesives*, **28**, 302-313, (2008).

14. N.A. Fleck, J.W. Hutchinson, Z. Suo, Crack path selection in a brittle adhesive layer, *International Journal of Solids and Structures*, **27**, 1683-1703, (1991).

15. X.P. Xu, A. Needlman, Numerical simulation of fast crack growth in brittle solids, *Journal of the Mechanics and Physics of Solids*, **42**, 1397-1434, (1994).

16. Q.D. Yang, M.D. Thouless, Mixed-mode fracture analyses of plastically-deforming adhesive joints, *International Journal of Fracture*, **110**. 175-187 (2001).

17. Z. Zhang, G.H. Paulino, Cohesive zone modeling of dynamic failure in homogeneous and functionally graded materials, *International Journal of Plasticity*, **21**, 1195-1254 (2005).

18. C.D.M. Liljedhal, A.D. Crocombe, M.A. Wahab, Damage modeling of adhesively bonded joints, *International Journal of Fracture*, **141**, 147-161 (2006).

19. M.G.A Tijssens, E. van der Giessen, L.J. Sluys, Modeling of crazing using a cohesive surface methodology, *Mechanics of Materials*, **32**, 19-35 (2000).

20. R. Estevez, M.G.A. Tijssens, E. van der Giessen, Modeling of the competition between shear yielding and crazing in glassy polymers, *Journal of the Mechanics and Physics of solids*, **48**, 2585-2617 (2000).

21. B.F. Sorensen, T.K. Jacobsen, Determination of cohesive laws by the J-integral approach, *Engineering Fracture Mechanics*, **70**, 1842-1858 (2003).

22. T. Anderson, U. Stigh, The stress-elongation relation for an adhesive layer loaded in peel using equilibrium of energetic forces, *International Journal of Solids and Structures*, **41**, 413-434 (2004).

23. Q.D. Yang, M.D. Thouless, S.M. Ward, Elastic-plastic mode-II fracture of adhesive joints, *International Journal of Solids and Structures*, **38**, 3251-3262 (2001).

24. S. Li, M.D. Thouless, A.M. Waas, J.A. Schroeder, P.D. Zavattieri, Use of mode-I cohesive-zone models to describe the fracture of an adhesively-bonded polymer-matrix composite, *Composite Science and Technology*, **65**, 281-293 (2005).

25. S. Li, M.D. Thouless, A.M. Waas, J.A. Schroeder, P.D. Zavattieri, Use of cohesive-zone models to analyze fracture of a fiber-reinforced polymer-matrix composite, *Composite Science and Technology*, **65**, 537-549 (2005).

26. A. Needleman, A continuum model for void nucleation by inclusion debonding, *Journal of Applied Mechanics*, **54**, 525-531 (1987).

27. G.E. Beltz, J.R. Rice, Dislocation nucleation versus cleavage decohesion at crack tip, in modeling the deformation of crystalline solids: physical theory, application and experimental comparisons, *TMS*, Warrendale, PA (1991).

28. V. Tvergaared, J.W. Hutchinson, The relation between crack growth resistance and fracture process parameters in elastic plastic solids, *Journal of the Mechanics and Physics of Solids*, **40**, 1377-1397, (1992).

29. Z. Suo, C.F. Shih and A.G. Varias, A theory for cleavage cracking in the presence of plastic flow, *Acta Metallurgica et Materialia*, **41**, 1551-1557, (1993).

30. ABAQUS User's Manual, v6.11, Pawtucket, USA, 2002.

CHAPTER 5 SINGLE SHEAR LAP TEST AND DOUBLE SHEAR LAP MODELING

5.1 Introduction

Previous nanoindentation studies have shown that hydraulic oils can have hardening (Frekote) or softening (#3 hydraulic oil) effects on an adhesive matrix (EA9394). According to fracture mechanics, the measured mechanical properties of adhesives can be correlated to the fracture process through Griffith and Irwin theory.

$$\Gamma_{eff} = \beta \frac{\sigma_{\infty}^2 a}{E} \tag{12}$$

$$r_p \sim \left(\frac{K_C}{\sigma_Y} \right)^2 \tag{13}$$

where β is a geometric factor of order unity, a is the crack length and σ_{∞} is the applied remote stress. Thus, a contaminant producing a softening effect would increase the fracture zone size and the plastic dissipation would increase correspondingly.

Double-cantilever beam tests have shown that the contaminations applied at bondline could dramatically decrease the mode-I steady-state bond-line strength. In such cases, an interfacial energy-weakening effect is the primary effect on bond-line integrity. However, to have a full understanding of contaminant effect on bondline, the behavior of the failure initiation and shear strength with contaminants requires more study. The single-shear lap

(SSL) test has great practical importance. It can show the fracture initiation critical force in the fracture process, because the crack would be catastrophic after the critical force.

The shear lap test was first proposed to analyze the deformation of an adhesive layer under differential-shear loading (Volkersen, 1938). Later, Goland expanded Volkersen's work and analyzed the shear lap by examining the effects of the bending moment introduced by tensile loading (Goland et al, 1944). The plasticity of the adhesive layer was further taken into account by L.J. Hart-Smith (Hart-Smith, 1974). Delale studied the single-shear lap joint mathematically (Delale et al, 1981). They found that the maximum shear stress in adhesive is lower than the maximum normal stress. In Dalale's work, they assumed linear elastic adherend and viscoelastic adhesive. However, a universal stress-based criteria has not been well established (Lee, 1991). Finite-element method was also employed to conduct shear lap test with various assumptions to understand both material and geometry effects (Zou et al, 2004; Dattaguru et al, 1984; Kafkalidis et al, 2002). The bonding edge of the adhesive-bonded joints is a critical boundary condition in shear testing. Many experimental and numerical studies have examined the effect of fillet shape on adhesive bonding. Adams compared triangular and square shapes of adhesive-bonded joints and found that a triangular fillet could reduce stress concentration effects by 30% compared to a square fillet (Adams et al, 1974). In this work, for simplicity and comparison of the different contaminants, we cut the fillet for consistent results. A mixed-mode cohesive zone model has been developed to model interfacial behavior of bi-material systems (Tvergaard et al, 1992; Wei et al, 1997). It has proven to produce good agreement with experimental results. This approach has been used to model the behavior of plastic adhesive joints in shear lap test (Yang et al, 1999).

In this work, the single-shear lap test has been used to measure bond-line fracture-initiation force. Composite structure is composed of 10-ply Hexcel IM7-G/8552 composite and Loctite Hysol EA9394 paste adhesive was for adhesive bonding. Aviation hydraulic oil (#3 MIL-PRF-85570) was introduced at different levels to play the role of contamination during the fracture initiation process. A finite-element method with a cohesive-zone model was used to rationalize the experimental results.

5.2 Materials and Sample Preparation

5.2.1 Materials

In this study, we chose aviation hydraulic oil #3 (MIL-PRF-85570) as a contaminant to be applied on adhesive bondline. Previous work (Chapter 2) showed that #3 oil has a softening effect on the selected adhesive EA9394. In accordance with the maintenance standard (MIL STD 1246C), the following contamination levels were selected.

Contamination level	Surface concentration
G	10 μm/cm^2
J	55 μm/cm^2

Table 5.1 The contaminate levels

5.2.2 Sample preparation

Single shear lap testing is a common method for measuring the shear toughness of adhesive-bonding composite. ASTM 3161 is a standard designed for measuring the shear strength of an adhesive bond. In accordance with that standard, the sample laminates were

made of 10-ply stacked unidirectional prepreg (Hexcel IM7-G/8552). A bi-directional woven fabric (Hexcel W3B-282) was used as a cover layer applied at 45^{o} on both sides. The stacked fiber was vacuum-bagged and autoclave-cured. The cured composite was sand-blasted with 220 alumina grit at 413.7kPa to roughen its surface to 3-4μm Ra. Figure 3.3 shows the surface roughness as measured by a Zygo profilometer. After surface treatment, the composite was rinsed with water and wiped with Hexane for degreasing, and samples were then cured at 90^{o}C for 2hrs (NAVAIR 01-1A-21, Sec. 6-7a (2)). After cleaning, measured dilutions of hydraulic oils were applied uniformly on the entire roughened composite surfaces and the adhesive pasted onto the 25.4x101.6mm bonding area of another sand-blasted composite surface. A 0.2mm shim was inserted around the edge for maintaining the adhesive bonding thickness. The two-composite panel was assembled and stacked under 34kPa pressure at ambient temperature for 24 hours. Curing was then applied for 2 hours in an autoclave at 90˚C. After curing, the composite stack was cut to a width of 25.4mm. Because the adhesive would spill out under the pressure, removal of a spillover section was required to establish a standard boundary condition. 25.4x50mm tension blocks were adhered to the ends of the sample to support fitting into the test frame.

Figure 5.1 Optical image showing the geometric details of a SSL specimen.

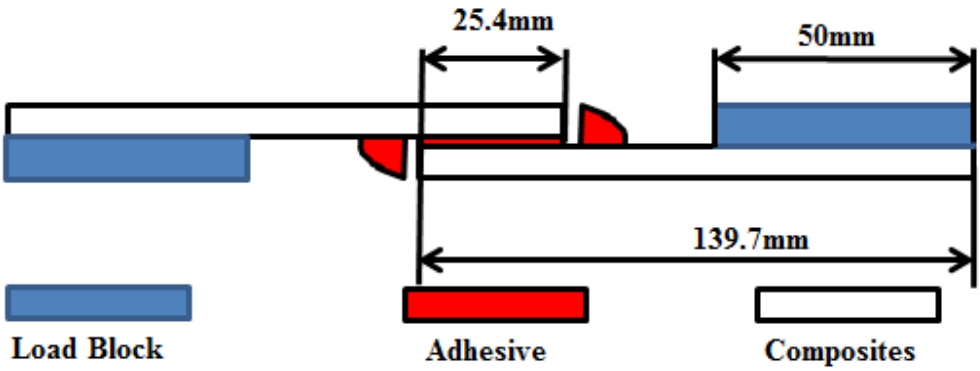

Figure 5.2 The dimensions of the single shear lap samples

5.3 Single Shear Lap Test and results

5.3.1 Single Shear Lap Test Protocol

The single-shear lap tests were carried out in a computer-controlled servo-electric testing frame and performed with displacement control using a loading rate of 0.02mm/s. Force and crosshead displacement were recorded. The SSL tests were repeated on two identical samples to provide data consistency.

Figure 5.3 The SSL expertimental testing setup.

5.3.2 Results and Discussions

Aviation hydraulic fluid #3 MIL-PRF-85570 was examined at levels G and J. Summary of break force and calculated critical stress values are given in Figure 5.4. Sliding of samples sometimes occurred between the clamps and load blocks, and was attributed to

lack of friction between clamps. Since the most important parameters in this experiment were the critical forces or critical shear strengths, the resulting inaccuracies in displacement data were neglected.

From the results, it is interesting to notice that the critical force of fracture initiation increases with higher contamination levels. From previous work it can be seen that hydraulic oil #3 has a softening effect on the adhesive matrix. Such a softening effect on the adhesive layer could expand the plastic zone size according to Irwin theory $r_p \sim (\frac{K_C}{\sigma_Y})^2$, and the contamination also could decrease the interfacial bonding strength. In such a case, softening is the primary effect because the shear process zone size is much larger than the constrained mode I tension process zone. The experimental work shows the effect of contamination on the fracture initiation force, but a detailed stress field analysis is still needed to understand the softening effect. Cohesive zone models were further utilized to simulate this single-shear lap test.

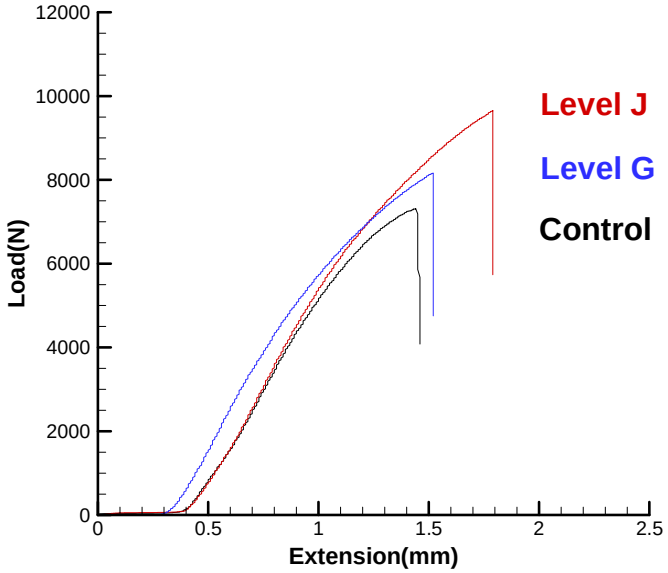

Figure 5.4 Summary of load-displacement curves of the shear lap test

Sample	Control-1	Control-2	10μg/cm^2	55μg/cm^2 -1	55μg/cm^2 -2
Critical Load(N)	7237	6993	8161	9639	9015

Table 5.2 Summary of the fracture toughness measurements for different levels of hydraulic fluid #3

5.4. Shear Lap FEM Analysis and Discussions

Commercial finite-element package ABAQUS was used to simulate the 2-D double-shear lap model with a cohesive-zone model. The composite panel was modeled with linear elastic material. The adhesive was modeled as an elastic-plastic material. The material properties of composite and adhesive are given in Table 5.3.

	Adhesive	Composite
Modulus(MPa)	4300	43700
Yield stress(MPa)	69	N/A
Poisson ratio	0.3	0.3

Table 5.3 The material properties in the finite element model

The adhesive bonding was modeled using a cohesive-zone model, as shown in Figure 2.12. The cohesive surface was elaborately introduced in Chapter 4. The constitutive equation of the cohesive law is based on a phenomenological model. At the start of loading, the stress and strain have a monotonically-increasing relationship. After a critical point, the stress will start to drop while the strain increases. The cohesive bonding breaks when the stress drops to zero.

The constitutive curve describes the failure behavior of the cohesive element. The area under the constitutive curve is the intrinsic fracture energy of the cohesive element, corresponding to the interfacial fracture toughness. The cohesive law is governed by three independent parameters: k, σ_0, Γ. In this chapter, we will examine the effect of #3 hydraulic oil on the bondline. Because the cohesive parameters for mode II failure are unknown, we assume that the ratio of cohesive parameters for reference state and contaminated state (#3 at 55μg/cm^2) are constant for both mode I and mode II failure. The ratio of cohesive parameters for mode I failure was first determined by the method described in Chapter 4. From the curve correlation, the cohesive parameters for #3 hydraulic oil at 55μg/cm^2 are determined and shown in Table 5.4. Figure 5.5 shows the corresponding initiation force and steady state fracture energy for both experimental and simulation results.

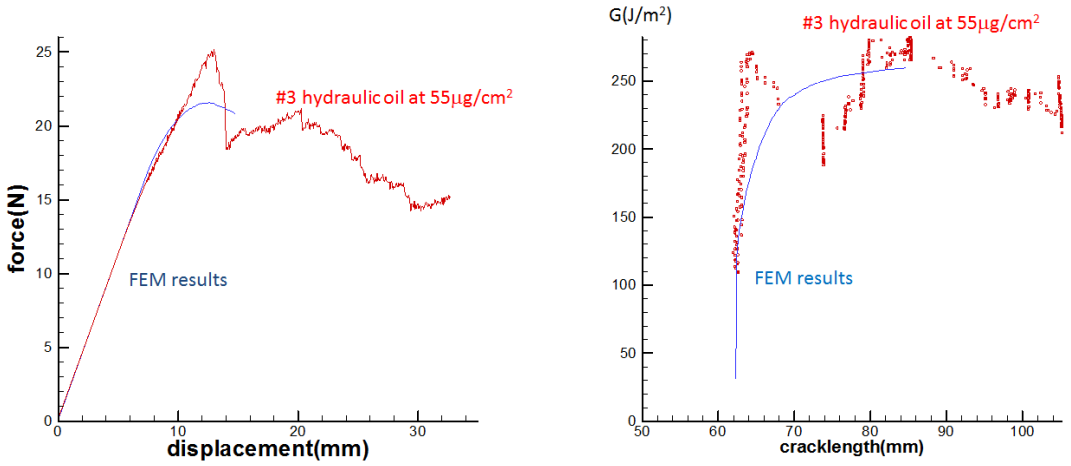

Figure 5.5 The force-displace plot and crack length-energy release rate plot for determine corresponding cohesive parameters for #3 hydraulic oil at 55µg/cm^2

	Reference- no contamination	#3 hydraulic oil at Level J contamination
Stiffness K(MPa)	3e6	3e6
Cohesive stress σ(MPa)	135	67.5
Interfacial fracture energy G(J/m^2)	250	62.5

Table 5.4 The interfacial parameters for the reference state and the contamination state of #3 hydraulic oil at 55µg/cm^2

From Table 5.4, the ratio of cohesive stress for reference state and contaminated state (#3 at 55µg/cm^2) is 2. Then the cohesive parameters for mode II failure will be determined by corresponding single shear lap experimental results. The cohesive stress is determined by the corresponding maximum force in the shear test. The cohesive energy is determined by proportional method described in Chapter 4. From single shear lap experiments, the cohesive stress and cohesive energy for reference state are 95MPa and 120J/m^2. Then from the ratio of cohesive stress determined from mode I failure, the cohesive parameters for contaminated state (#3 at 55µg/cm^2) are 47.5MPa and 30J/m^2.

Chapter 2 has shown that #3 hydraulic oil have softening effect on the adhesive. Chapter 4 showed that the applied #3 hydraulic oil on the bondline can weaken the cohesive energy and stress. In this chapter, four cases were studied to show the mixed effect on the critical shear stress in mode II failure. A double shear lap model was used to evaluate the bondline fracture initiation force with different bondline parameters. The parameters used in this study are shown in Table 5.5.

Case	Cohesive Stress (MPa)	Cohesive Energy (J/m2)	Adhesive Yield Stress (MPa)	Adhesive Modulus (MPa)
A	95	120	69	4300
B	47.5	30	69	4300
C	47.5	30	62.5	3956
D	95	120	62.5	3956

Table 5.5 The parameters used in the double shear lap simulation

Because the shear model represents an unstable fracture, the force at the tenth element break was recorded for each case. Figure 5.6 shows the contribution of cohesive parameters and adhesive mechanical properties to the critical shear stress in the DSL model.

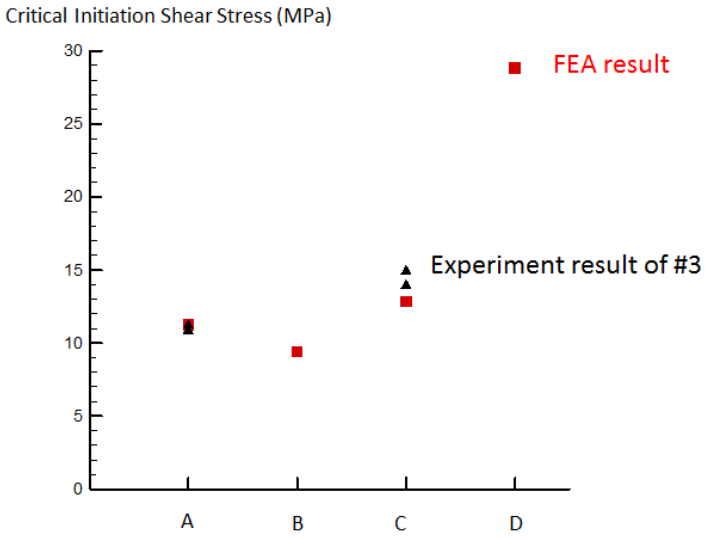

Figure 5.6 FEM results showing the parametric effects on critical initiation shear stress in DSL modeling

In Figure 5.6, case A is the reference case, which correspond to the non-contaminated bondline maximum shear stress. Case B shows the interfacial weakening effect of contamination with the cohesive stress changing from 95MPa to 47.5MPa, corresponding to the concentration of the contaminant. The maximum shear stress drops from 12MPa to 9.5MPa with the interfacial weakening. Case D shows the softening effect of contamination. As measured by nanoindentation, with 55μg/cm^2 #3 hydraulic oil, the adhesive yield stress drops from 69MPa to 62MPa and the adhesive modulus drops from 4.3GPa to 3.9GPa. It is as expected that the softening of the adhesive could increase the maximum shear stress, because the plastic zone size expand with the decreased modulus and yield stress. In case C, it is shown that the combination of the two effects can slightly increase the maximum shear stress. And the simulation results have good agreement with the experimental results.

From the simulation, we conclude that the total fracture energy is composed of two parts; one comes from the intrinsic fracture surface energy and another larger part is dissipated by the plastic work during crack growth. By applying the contamination on the bondline, the cohesive strength and the adhesive mechanical properties may be changed. The interfacial (cohesive) weakening can shrink the plastic zone size as shown in Chapter 4. And the adhesive softening can expand the plastic zone size. Unlike mode I failure, the combination of these two opposite effects can slightly increase the maximum shear stress in mode II failure. The reason of this phenomenon is that, the crack is unstable in the shear test; the maximum initiation force depends on the crack initiation process. Thus contaminated-induced cohesive energy weakening has less effect in the mode II failure. However, the softening effect has the same effect on the stress distribution. Therefore, the combination of these two effects may increase fracture initiation force.

5.5 Conclusions

To fully understand the effect of contaminants on bond-line integrity, a single-shear lap test was used to measure the critical force of adhesive bonding attacked by hydraulic fluid oil #3 MIL-PRF-85570. It has been shown that the greater the level of contaminant applied on the bondline, the higher the bonding strength in mode II failure. Additional numerical simulation was used to investigate the stress distribution of the shear test. It was found that the change of yield stress of adhesive determine the process-zone size. And the cohesive energy weakening had less effect on the unstable crack in shear test; because the catastrophic failure occurs before the cohesive zone completely fail. Therefore, in the mode

II failure, the combination of the effects of contamination may increase the crack initiation force at some specific conditions.

5.5 References

1. V.O. Volkersen, Die nietkraftverteilung in zugbeanspruchten nievtverbindungen mit konstanten laschenquerschnitten, *Luftfahrforschung*, **15** ,41-47, (1938).

2. M. Goland and E. Reissner, The stresses in cemented joints, *Journal of Applied Mechanics*, **66**, A17-A27, (1944).

3. L.J. Hart-Smith, Analysis and design of advanced composite bonded joints, NASA contractor report, McDonnell Douglas Corporation, California, 1974.

4. F. Delale and F. Erdogan, Viscoelastic analysis of adhesively bonded joints, *Journal of Applied Mechanics*, **48**, 331-338, (1981).

5. L.H. Lee, Adhesive Bonding, *Plenum Press*, New York (1991).

6. G.P. Zou, K. Shahin, F. Taheri, An analytical solution for the analysis of symmetric composite adhesively bonded joints, *Composite Structures*, **65**, 499-510, (2004).

7. B. Dattaguru, R.A. Everett, J.D. Whitcomb and W.S. Johnson, Geometric nonlinear analysis of adhesively bonded joints, *Journal of Engineering Materials and Technology*, **106**, 59-65, (1984).

8. M.S Kafkalidis, M.D. Thouless, the effects of geometry and material properties on the fracture of single lap shear joints, *International Journal of Solids and Structures*, **39**, 4367-4383 (2002).

9. R.D. Adams, N.A. Peppiatt, Stress analysis of adhesive-bonded joints, *Journal of Strain Analysis*, **9**, 185-196, (1974).

10. V. Tvergaard and J.W. Hutchinson, The relation between crack growth resistance and fracture process parameters in elastic-plastic solids, *Journal of the Mechanics and Physics of Solids*, **40**, 1377-1397, (1992).

11. V. Tvergaard and J.W. Hutchinson, On the toughness of ductile adhesive joints, *Journal of the Mechanics and Physics of Solids*, **44**, 789-800, (1996).

12. Y. Wei and J.W. Hutchinson, Nonlinear delamination mechanics for thin films, *Journal of the Mechanics and Physics of Solids*, **45**, 1137-1159, (1997).

13. Y. Wei and J.W. Hutchinson, Interface strength, work of adhesion and plasticity in the peel test, *International Journal of Fracture*, **93**, 315-333, (1999).

14. Q.D. Yang, M.D. Thouless and S.M. Ward, Numerical simulations of adhesively-bonded beams failing with extensive plastic deformation, *Journal of the Mechanics and Physics of Solids*, **47**, 1337-1353, (1999).

15. Q.D. Yang, M.D. Thouless, Mixed-mode fracture analyses of plastically-deforming adhesive joints, *International Journal of Fracture*, **110**, 175-187, (2001).

CHAPTER 6 GENERAL CONCLUSIONS

6.1 Conclusions

The dissertation studied the degradation mechanisms of specific contaminants on adhesive bonding of composite. The main focus of this work was the contamination effect on the adhesively bonded joints. It is found that the contamination has effects on both the interfacial bonding strength and the adhesive mechanical properties.

These two effects of contaminants on adhesive bondline were explored and theoretically analyzed to correlate with the adhesively bonded joints strength. Nanoindentation was used to make a non-destructive and quick measurement of the mechanical properties of an adhesive attacked by contaminants. Through the screening of nanoindentation, the Frekote have hardening effect on the adhesive EA9394, #3 hydraulic oil has softening effect on the adhesive, #1 and #2 hydraulic oil has no significant effect on the adhesive. The degradation sorting was established according to the nanoindentation results. The mode I DCB test was further used to directly measure the bond-line toughness of the contaminated adhesive bonding. It is shown that the residual adhesive bonding toughness was below 20% of original non-contaminated bonding strength at level J ($55\mu g/cm^2$). The nanoindentation test and the DCB test have the same trend for the series of contamination degradation at the same contamination level. A finite-element model with cohesive zone surface was employed to rationalize the contamination effect on the adhesive-bonding-joint toughness. It is found that an interfacial shielding effect shrinks the plastic dissipation energy

in the mode I DCB test. Thus, bond-line toughness degradation is primarily caused by decreased interfacial energy in mode-I fracture.

A series of DCB tests was conducted to find the acceptable concentration level of two types of contaminants. Surface treatment is required to create reliable adhesive bonding. And a proper failure type was discussed. The sandblasting to 4μm roughness was found to be the suitable surface pretreatment for the current composite/adhesive system. The correlation between contaminant concentration levels and adhesive-bonding toughness was established for hydraulic oil #1 and #2. The features of the load-displacement curve and the fracture surface topography show a gradual transition of the failure type from large-scale bridging to brittle fracture caused by contamination-induced interfacial strength weakening.

A full parametric study of adhesive bondline was conducted using finite-element methods with cohesive zone surface. The parameters of adhesive bondline were divided into three groups. The first group describes the first effect of contaminants, the interfacial shielding effect. Different levels of concentration on adhesive bondline were modeled to study the corresponding interfacial surface toughness. It is found that the interfacial strength weakening can shrink the plastic zone size. Thus the plastic dissipation decreases with the applied contamination level. The second group of parameters confirmed the second effect of contaminants, the effect on adhesive mechanical properties. The contaminant effect on the hardness and modulus of adhesive layer were correlated to the effective adhesive bond-line toughness through the plastic dissipation. The third group is the thickness of the adhesive layer. The simulation results verify the shielding effect of the thickness. The plastic zone size

is constricted by the thickness of the adhesive layer in mode I fracture. Thus, the plastic dissipation and the effective bondline toughness decrease with the thinner adhesive layer thickness.

In chapter 5, the single-shear lap test experimentally shows the effect of the hydraulic oil #3 on the bondline fracture initiation force. It is found that the fracture initiation force increase with applied #3 hydraulic oil contamination level. Further simulation of shear test clarified the whole fracture-initiation process. It is found that the contamination-induced interfacial strength weakening has less effect on the unstable crack initiation in mode II failure. The softening effect of #3 hydraulic oil expands the plastic zone size. Therefore, the combination of the contamination effects makes the crack initiation force slightly higher in mode II failure.

In summary, this research provides a fundamental understanding of contaminant effects on adhesive-bonded joints in composite structures. The experimental and numerical work provides a framework based on a constitutive cohesive zone model. The two effects of the contaminants on the bondline have been differentiated. The effect of contamination on bond-line toughness was studied both experimentally and numerically. The theory and results presented in this work could be exploited to improve the reliability of adhesive bonding, set a failure criterion for adhesive-bonded composite structures, and provide some insight on universal criterion with respect to the contaminant effect.

6.2 Future Work

The work revealed two effects of contaminants on the adhesive bonding joints toughness. In Chapter 2, DCB test shows the interfacial shielding effect is the primary effect. In Chapter 5, single shear lap test shows the softening effect is the primary effect. It would be important to elucidate a phase diagram for general boundary condition.

In Chapter 3, the acceptable level of contaminants was investigated on the selected composite system. According to the study, the degradation of bondline integrity is caused by the interfacial shielding effect. More contaminants type could be testified to establish a universal relationship of the concentration level and the interfacial shielding strength.

In Chapter 4, the parametric study of adhesive bondline was conducted by finite element study. The adhesive properties and the interfacial strength have been studied experimentally. The thickness effect of the adhesive layer could be explored by experiments. A series of DCB sample with different adhesive layer could give a correlation between the thickness and the effective bondline toughness. Through curve fitting, the interfacial toughness of specific concentration level of contaminants could be deduced by the points, which the thickness is zero.

Another extension of this work would be establishing the interplay between contaminants and other factors. In real application, the adhesive bonding joints always suffer

multi-factors degradation. The clarification of the interplay between factors could further reduce the production cost of composite structures.

APPENDIX: SPECTRAL ANALYSIS OF THE 3D FRACTURE SURFACES FOR ENHANCED FORENSIC MATCHING

A.1 Introduction

Tool marks have been used as evidence in testimony since 1993. Since then, the National Institute of Justice (NIJ) has an expanding need for the forensic evidence extracted from criminal tools (U.S. DoJ, 2009). Many researchers have studied the reproducibility and durability of the forensic tool mark (Bonfanti et al, 1999; Monturo et al, 2010; Miller et al, 2001). The premise of the tool mark evidence is based on the uniqueness generation of the tool mark. There are many unique parameters that can trace to the unique tool mark, including color, shape and orientation of tool mark, grain size etc. (Katterwe 2005). Manufacturing process (Bonfanti et al 1999) and loading history (i.e. attack motion) (Ekstrand, 2012; Grieve, 2013) of the tool are the main areas to study the uniqueness of the toolmark generation. The manufacturing finishing process (e.g. rolling, extrusion forging, stamping) can be described by unique Grain Orientation Distribution Functions (Alexanndrov et al, 1995). Through the mathematical description of tool marks, the manufacturing process can be restored. And the toolmarks on the fracture surface have been proven to relate the loading history (e.g. loading rate, loading mode) (Baldwin et al, 2013). Uniqueness of environment degradation could also give uniqueness toolmark feature (Baldwin et al, 2013). However, the tool mark evidence was challenged due to the lack of scientific evidence and the examiners' subjective opinion. In 2000, the toolmark match

evidence was considered inadmissible in the supreme court of Florida. More work is required to make a reproducible and reliable method to distinguish the toolmark.

The purpose of this work is to provide a reliable algorithm to analyze forensic tool marks. This study focused on matching the fracture surfaces of steel knives with different breaking history. 3-D Zygo profilometer was used to scan the fracture surface of the steel knives. Micro-level features were collected by digital image scanning. A developed program was used to analyze the data from the start and determine the matches or non-matches. This developed statistical program can exclude the subjectivity by examiners and significantly improve the efficiency. Fast Fourier transform (FFT) was used to transform the scanning fracture surface to the frequency spectrum. The microstructures of the fracture surface were characterized in the frequency spectrum. Proposed statistical method was utilized to analyze the characteristics of the microstructures in the frequency spectrum and determine the match of the fracture surface database.

A.2 Proposed Hypothesis and Implementation Methodologies

A.2.1 Proposed Basic Theory

Starting with the general materials classification, solid materials have three classes: crystalline (metals and ceramics), semi-crystalline (polymers) and amorphous (Polymers and glasses). They have different molecular structures and therefore different characteristic toolmarks. In this work, we focus on the steel knives (SS-440C), which is crystalline metal. Crystalline material is typically a polycrystalline aggregate, which is comprised of crystal

lattice and grain. The sizes and orientation of the lattice and grain have unique statistical characterization that could enable the forensic toolmark (which is the fracture surface micro-features) examination.

For crystalline metal, the fracture surface micro-features or toolmarks are composed of multi scales of material microstructures as depicted on Figure A.1. The sub-micron level structures (dislocations, grain size and grain orientation etc.) are more likely related to the manufacturing process. For example, the thermal treatment of the steel could contribute to certain grain size. The mechanical treatments (e.g. extrusion or rolling) have their own characteristics of grain orientation. The interplay between material properties and the loading history result in the above-micron level structures. For example, the bending break would leave a paralleled toolmark along the symmetric line. And the grain size could affect the spacing between two paralleled toolmarks. The loading process under cold temperatures would show brittle fracture and leave a smoother surface than ductile fracture. Thus the forensic tool mark examination has a solid background on the material science and mechanics. In mechanics, crack initiation, coalescence and propagation depend on the tool's crystallographic structure and loading history. The tool-breaking process leaves the unique mark on the surface. Through analyzing the fracture surface toolmark, we can unveil the crack behavior and then determine the correlation of two surfaces.

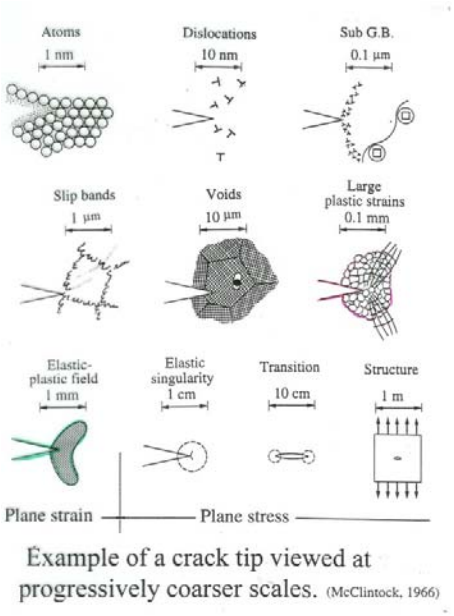

Figure A.1 Interaction of the crack trajectory with the material length scale, viewed at progressively coarser scales (McClintock, 1966)

Clearly, the micro-feature distribution on the fracture surface is directly related to the unique tool. Digital image analysis gives a new angle to study the forensic toolmark (Baldwin et al, 2004). The major advantage of digital image analysis is that the objective statistical analysis gives scientific foundation to the forensic tool mark analysis. With digital images of the fracture surface, there are two main leading methods to analyze the micro-features. The first one is based on real space. Scale-invariant feature transform is one of the algorithms to detect local invariant feature and determine the correlation (L. David 1999; L. David, 2004). Another method is based on frequency spectrum. This method transforms the original image into frequency domain and then analyzes the frequency spectrum. Because the micro-features on the fracture surface result from the interplay between the tool's crystallographic structure and loading history, the micro-features have several length scales.

And different scales of micro-features correspond to different cause to toolmark. For example, the toolmark at grain-size scale indicates the manufacturing process. Thus, the frequency method is more suitable and nature in detecting the multi-scales micro-features. It is easy to divide the frequency domain to analyze different scales of micro-features.

Fourier transform is very common to transform the real space signal to frequency domain. The 1-D Fourier transform for images along the axis is

$$F(k) = \sum_{j=1}^{N} f(j)(e^{(-2\pi i)/N})^{(j-1)(k-1)} \tag{A.1}$$

Where the *f(j)* is one line of the image in real space, *F(k)* is the frequency spectrum of the line. Figure A.2 and A.3 show an example of the Fourier transform of the standard sin wave. Figure A.2 is the sum of two sine waves with random noise. It is hard to distinguish the features from the real domain. After the transformation, the characteristics frequency of the features is very clear in frequency domain Figure A.3.

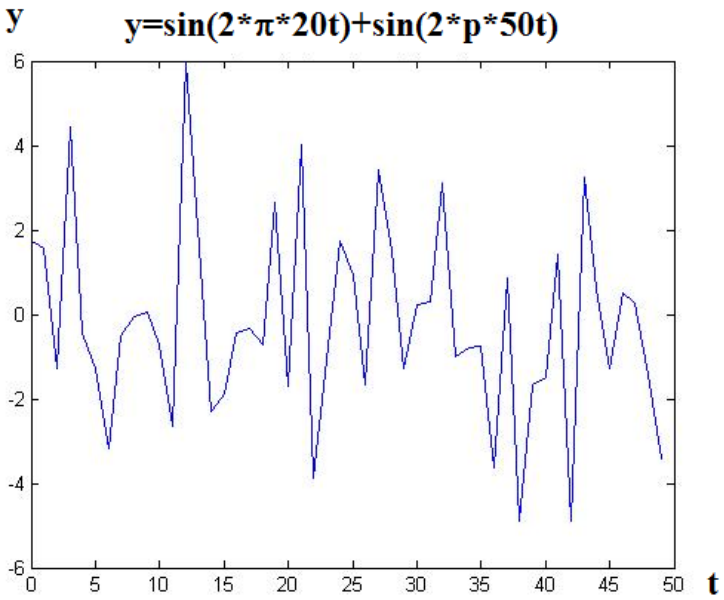

Figure A.2 The combination of two sine waves with different frequency

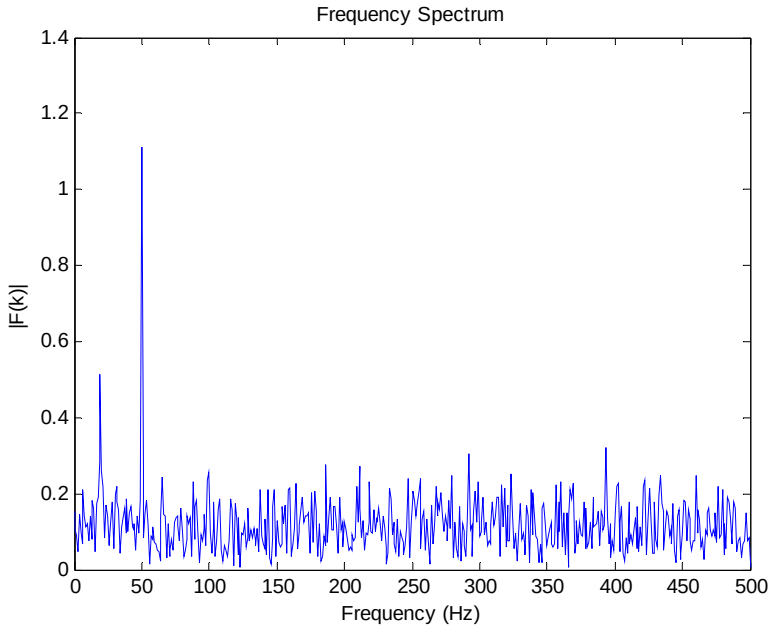

Figure A.3 The characteristic frequencies of the signal in Figure A.2 shown after Fourier Transform

Considering the paired fracture surfaces, they have the same grain size, the same orientation of grain and the similar features of tool mark. It is hard to distinguish the tool mark at different scale with the naked eye. With digital image processing at the frequency domain, the characteristics frequency of micro-features could be easily extracted and compared with auto-routine.

A.2.2 Material and Image Scanning

In this work, we will study steel knives (SS-440C) under pre-defined loading conditions. The loading fixture is shown in Figure A.4. After the sample breaks, a scanning electric microscope was used to scan the fracture surface. Bending fracture surface is shown in Figure A.5(a) and twisting fracture surface is shown in Figure A.5(b). It is clear that they have different micro-features at large scale.

Figure A.4 Optical Images of the loading frame and knives samples

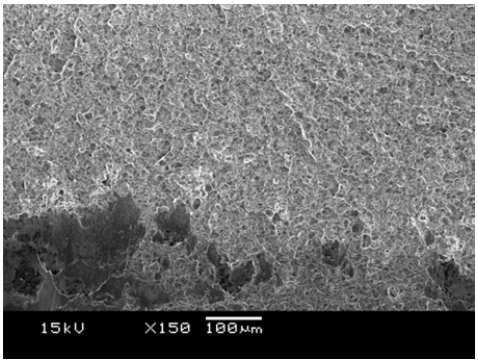

(a) The bending fracture surface

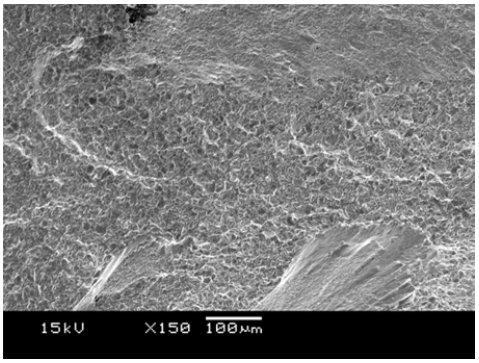

(b) The twisting fracture surface

Figure A.5 The SEM scanning of the fracture surface; (a) bending break; (b) twisting break.

A typical 3-D surface topography map of the fracture surface was taken by 3D optical interferometer (Zygo NewView 6300) as Figure A.6 and A.7.

There is a trade-off when we select the size of the imaging window. The size of the imaging window defines the maximum wavelength can be detected, which is the lowest cut-off frequency. In such case, the larger window size could detect larger micro-features. On the other hand, because the resolution is defined, the smallest feature size that can be detected is within 2-3 pixels, i.e. $2\frac{L}{r}$, where L is the window size and r is the resolution. So if we want to detect smaller feature, we need to shrink the imaging window size. Considering the mesoscopic fracture surface features ranges in 100-1000μm, the microstructure grain features ranges in 1-100μm, a selection of the detection range determines the proper window size to be used in examination. In the following work, we will use a 20X magnification and 0.55mm window size, which gives a balanced range for detecting useful micro-features. With such

configuration, the minimum and maximum distinguishable feature sizes are 1μm and 0.27mm.

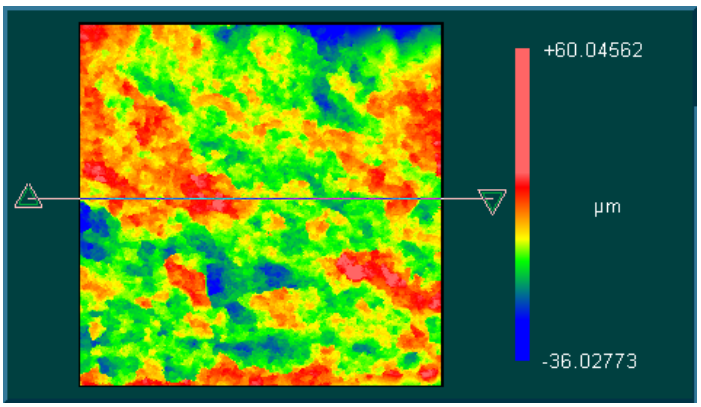

Figure A.6 Zygo scanned 3-D topography of the fracture surface

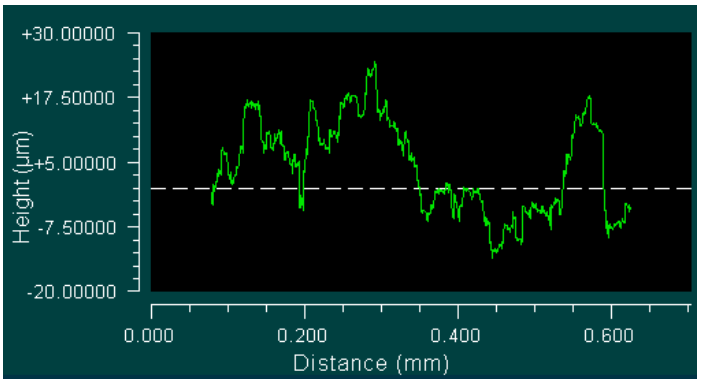

Figure A.7 The line profile of the Figure A.6

The fracture surface of the knives is not homogeneous, because the manufacture process. The tip side, which is called sector C, is narrower. And the base side, which is called sector A, is wider (Figure A.8). From the scanned surface profile, the horizontal line was extracted and compared in Figure A.9. It clearly shows the dominant wavelengths for the three sectors are different. This is because the stress state and the grain size are different for the three locations. The interplay of the material properties and the loading history makes the

difference of the micro-feature at different sectors. In our work, we only compare the fracture surface at sector A for all the samples.

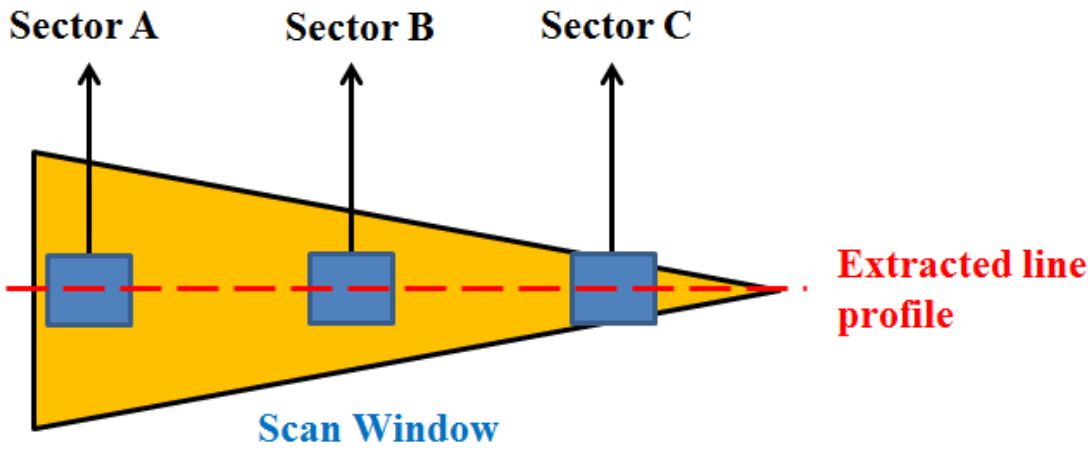

Figure A.8 The diagram of the location of scanning windows

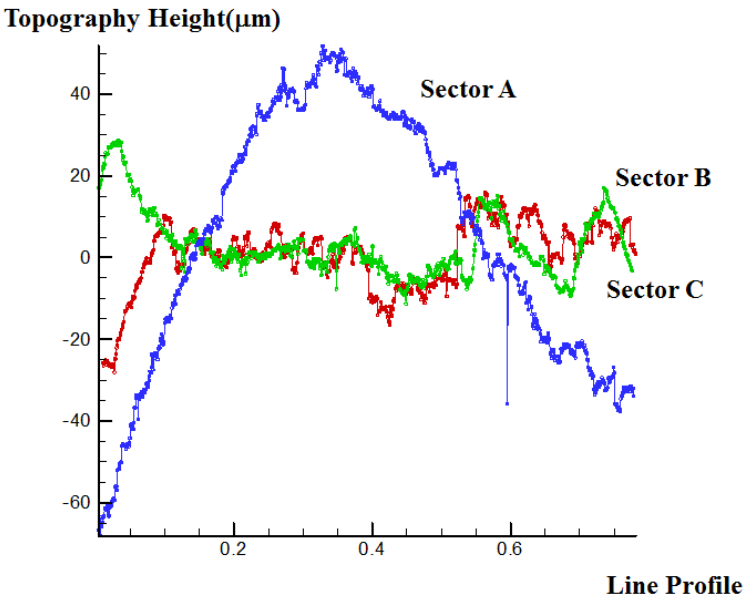

Figure A.9 The horizontal line profiles for different sectors of the fracture surface shown in Figure A.8

From the line, we can notice some large size features and small size features. The frequency spectrum can clearly show the feature characteristic frequency.

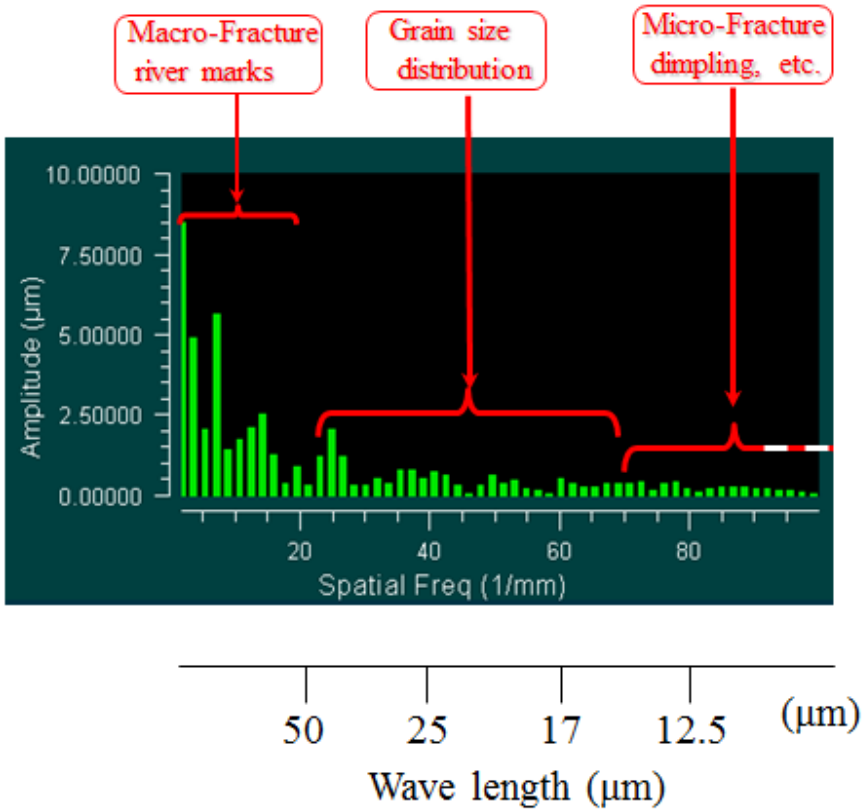

Figure A.10 1-D frequency spectrum description of the fracture surface

A.2.3 Image Enhancement

The image scanned by the Zygo interferometer has a lot of noise and black pixels. They will give significant noise in the frequent spectrum, because the noise in the real domain has very high amplitude. For objective analysis, the image enhancement is built in the program and has the same procedure for all of the images. In this work, we have three steps of image enhancement.

The first step is to fill the no-data points as shown in Figure A.11. The no-data points come from those points that have poor reflectivity. We will first use a 5X5 pixels window to scan the whole image pixel by pixel. Any no-data point is filled by the average of the valid data in this window. After this step, all of the pixels have a valid number.

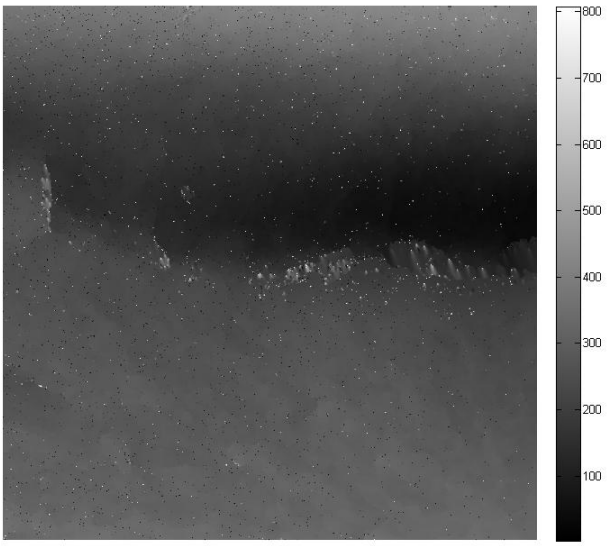

Figure A.11 The original scanning image shown in matlab with lots of no-data points

The second step is to clean out the noise data as shown in Figure A.12. The noise date was generated by reflectivity error of the surface. It usually appears around the cliff. A 19X19-pixels window is used to scan the whole image. Any point beyond 2-stdev of the whole window will be considered as noise data and will be replaced by the average of the 3X3 window around it.

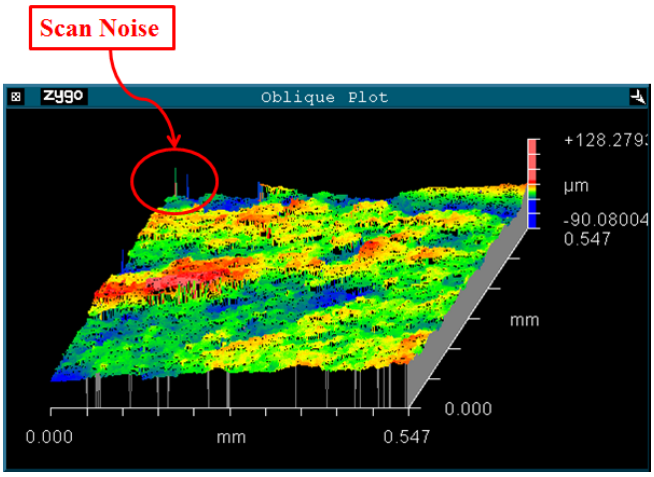

Figure A.12 The noise data in the scanned topography

The third step is mostly for the frequency spectrum quality. The average of the image is subtracted from the image to exclude the DC amplitude. The real domain image is a finite size image. However, in frequency transformation, it will be expanded periodically. And the periodical expansion will introduce cliff at the connection and strong noise in the frequency domain. Thus, the Hann filter could eliminate the discontinuity effect in the frequency spectrum. The filter and its effect are shown as Figure A.13–A.15. It has 10% tapering area at the edge.

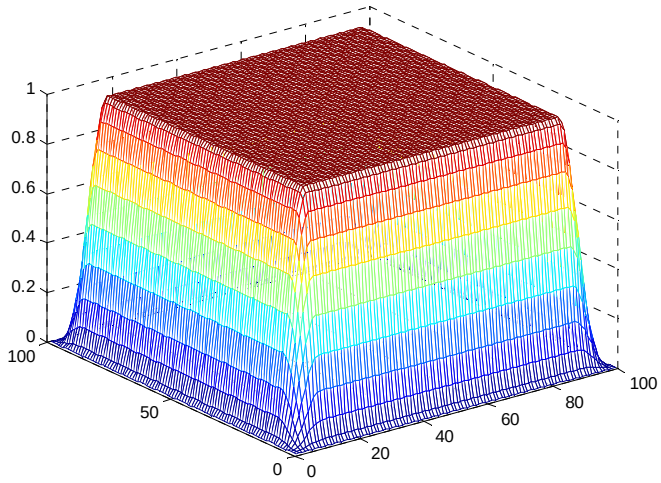

Figure A.13 Hann Filter with 10% taper

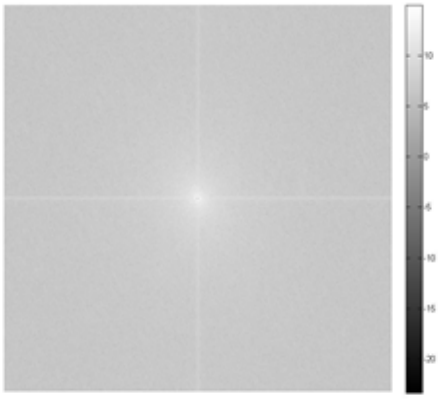

Figure A.14 Typical frequency spectrum without the Hann filter

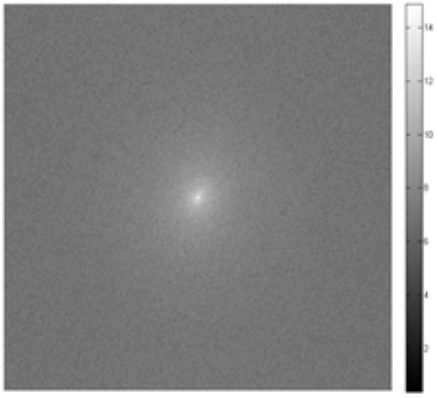

Figure A.15 The same frequency spectrum of Figure A.14 with the Hann filter

A.2.4 1-D Power Spectrum Density (PSD) Statistical Method

Even after the image enhancement, the noise signal can hardly be cleaned fully from the scanning. So the power spectrum density method is designed to further limit the noise effect. First, the image was transformed by 1-D Fast Fourier Transform (FFT) line by line. The horizontal line spectrum is p_x and the vertical line spectrum is p_y. Then all of the horizontal 1-D spectrums were summed up as P_x and all of the horizontal 1-D spectrums were summed up as P_y, where m is the number of horizontal line in image, n is the number of vertical line in image.

$$P_x(i) = \frac{1}{mn}\sum_{k=1}^{m}\sum_{j=1}^{n} x(k,j)(e^{(-2\pi i)/n})^{(j-1)(i-1)}$$
$$P_y(i) = \frac{1}{mn}\sum_{j=1}^{n}\sum_{k=1}^{m} x(k,j)(e^{(-2\pi i)/m})^{(j-1)(i-1)} \qquad \text{(A.2)}$$

The $P_x(i)$ represents the power carried by each frequency in x direction. And the $P_y(i)$ represents the power carried by each frequency in y direction. At a certain frequency, the

random noise has random power around zero, thus the sum of the power can decrease the noise effect in the PSD signal. To compare two images, one image's PSD was subtracted from another image's PSD. The difference was normalized by the first PSD. This normalized PSD is figure of merit and divided into three parts to show the comparison at different scales of micro-features.

To set the baseline, several images were scanned from the same surface, and then the PSD of these images is considered as reference. The reference PSD gives a characteristic PSD for the reference image, like fingerprints. If an unknown image has the PSD within the reference range, it means the unknown image has similar power level at a specific frequency and it matches the reference image. Otherwise, it has different characteristic PSD, which means non-match. The advantage of this method is the enhanced noise cancellation, but it is a 1-D analysis method.

A.2.5 2-D Frequency Spectrum Sectors Method

In this method, two images were first enhanced by the steps discussed above. Then the images were transformed into 2-D frequency spectrum. Because the 2-D frequency spectrum was symmetry about the center, only the top half frequency spectrum will be used for analysis further. The top half frequency spectrum then will be divided into multiple radial and angular sectors. The segmented angular sectors range from 0˚ to 180˚ with 45˚ interval. The angular sectors represent the characteristics of the orientation of the micro-features. For example, if a horizontal tool mark is dominant, the signal of characteristic frequency would be high at 90˚. The radial segments divide the spectrum from the center radially from 0 to

300 with 20 pixels interval. The radial sectors represent the characteristic frequency of the micro-feature. For example, if the grain size feature is 1/100 of the scanning window size, the signal would be high at radial 100. Figure A.16 is the diagram of the 2-D segmentation.

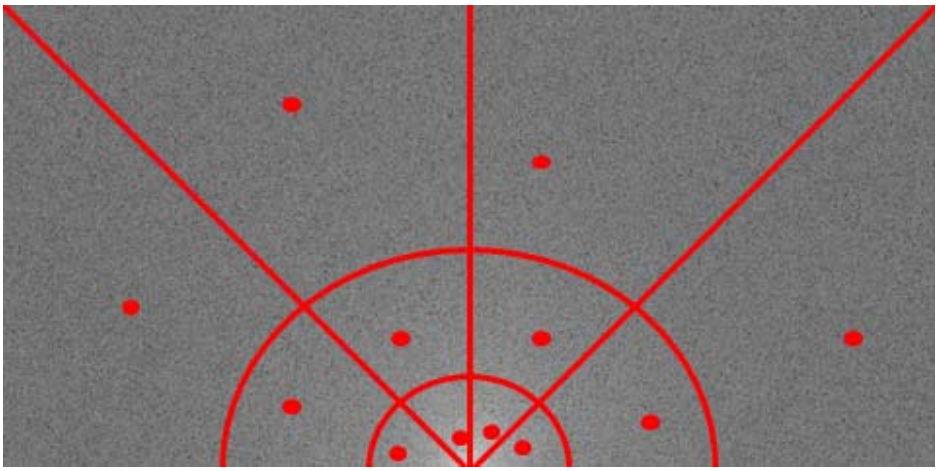

Figure A.16 Diagram of the segmentation method, the centroid of each segment is shown as dot

The segmentation is for finding the characteristic vector for each sector. The centroid for each sector is calculated and recorded as K(r, θ), r and θ are the index of sector.

Because the centroid vectors difference are proportional to the distance to the center, the vectors difference should be normalized by the distance. For paired images, we can get the correlation of these two images as

$$\Delta K(r) = \frac{1}{n}\sum_{\theta=1}^{n} \frac{K_1(r,\theta) - K_2(r,\theta)}{\frac{1}{2}(K_1(r,\theta) + K_2(r,\theta))} \tag{A.3}$$

The correlation vector *ΔK(r)* describe the correlation of two images on different levels of frequency or micro-feature. If the two images have similar large-size feature, the

correlation vector $\Delta K(r)$ at low frequency should be small, because the centroid should be close and vice versa. The correlation $\Delta K(r)$ was depicted versus r as figure of merit.

For determine the match or non-match of the pair images, we need to establish a base line or a threshold. Several pairs of images from the same fracture surface were recorded and analyzed by the algorithm. And the upper bound of the resulting correlation vectors $\Delta K(r)$ is considered as reference K_{ref}. The K_{ref} represents the characteristic distribution of the fracture surface. If the correlation vector of two images $\Delta K(r)$ has higher value than K_{ref}, these two images are considered as non-match. If the correlation vector of two images $\Delta K(r)$ is lower than K_{ref}, these two images are considered a match.

A.3 Results and Discussions

Two knives were bending-broken and two images were scanned from each fracture surface. The handle-side image was named as base side and the sharp-tip side of the fracture surface was tip side. The sample images were as Table A.1.

Knife 1 Base 1	Knife 4 Base 1
Knife 1 Base 2	Knife 4 Base 2
Knife 1 Tip 1	Knife 4 Tip 1
Knife 1 Tip 2	Knife 4 Tip 2

Table A.1 Knives samples

These images were cross-compared blindly. There should be 12 cases of match, which referred as true case and 16 cases of non-match as false case. If the program reports the pair of image match, then it is positive signal. If the program reports non-match, then it is negative signal. Ideally, the program should give 12 true positive and 16 false negative.

Considering the micro-feature size, the range of micro-feature size we interested is from the window size to 3μm, which is around the grain size. Thus, the figure of merit would be cut at frequency=300(1/mm).

A.3.1 1-D Power Spectra Density Results

The frequency spectrum was divided into three parts to differentiate the comparison at three scales of microfreature, which corresponds to large scale macro features, middle scale grain features and small scale fracture features. In this work, the baseline is at 0.1, if the average of the normalized PSD difference is above 0.1, the pair of images is considered as non-match and vice versa. The non-match case is shown as blue and match case is shown as red in Figure A.17. The statistic results are shown in Table A.2 and A.3. From the results, the precision of this method is around 97%.

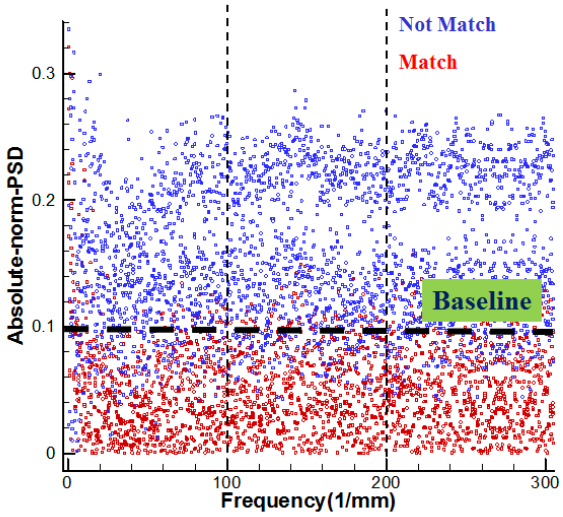

Figure A.17 The figure of merit of the PSD method. The dash line is base line analyzed from the same surface

PSD-X	Positive	Negative	Total
True	12(100%)	0(0%)	12
False	1(6%)	15(94%)	16

Table A.2 The accuracy of the PSD analysis in x-axis

PSD-Y	Positive	Negative	Total
True	12(100%)	0(0%)	12
False	1(6%)	15(94%)	16

Table A.3 The accuracy of the PSD analysis in y-axis

A.3.2 2-D Frequency Spectrum Sectors Results

The baseline was established with three pair of images scanned from the same surface. The figure of merit shows the match case as red and non-match case as blue in Figure A.18. Table A.4 summarizes the statistic results. The precision of this method is around 64%.

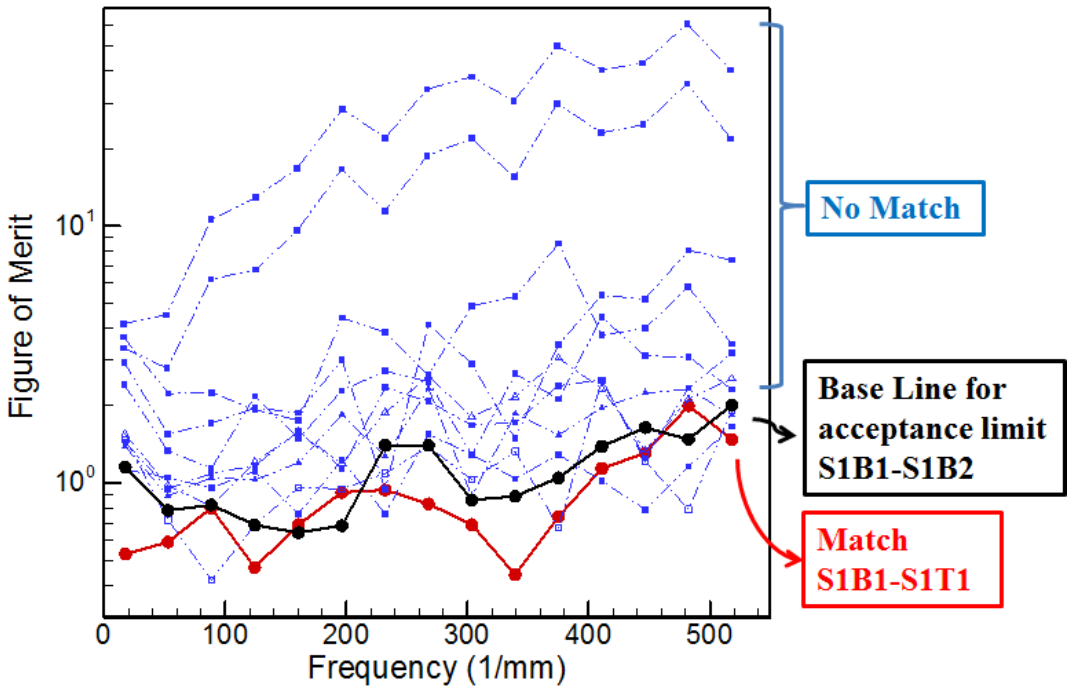

Figure A.18 The figure of merit for the sector segmentation method

Sectors	Positive	Negative	Total
True	5(42%)	7(58%)	12
False	3(19%)	13(81%)	16

Table A.4 The accuracy of the sector segment method for 28 cases

The results show that the automatic image processing is a promising method in the forensic evidence area. The PSD method could hit 97% accuracy in a blind test. And in the whole process, no subjective standard is involved. An additional point of interest is the high speed of auto-routine analysis. For the 28 cases, the total time to comparison is less than 15minutes. This is much faster than most of professional forensic analyst.

From the results, several challenges remained in the method development. First, the largest detectable feature is limited by the size of scanning window. For larger samples or larger fracture surface feature, larger scanning size or stitching multi-images are needed to analyze the correlation. Another restriction of this method is the orientation of scanning samples. The fracture surface is aligned with the same orientation while scanning samples. However, in a real case, the orientation of fracture surface maybe random. Then the anisotropic micro-feature will show low correlation. An additional optimization process is needed to make the surface image aligned to distinguish the anisotropic feature.

A.4 Conclusions

In this work, a preliminary fracture surface correlation method is proposed. Steel knives were bending to break. The fracture surface is scanned into digital images. Then from

the frequency spectrum of the digital images, different levels of micro-features (toolmark) are shown and correlated in figure of merit. Statistical algorithm is used to determine the correlation of the pair of images. The statistical algorithm is developed to compare the images based on forensic comparison process. The sectors method is a 2D method and has 70% accuracy. The PSD method is a 1D method and has 97% accuracy.

Although the PSD method works quite well with the knives in this work, more materials and more environmental effect (for example, different contaminates) need to be trialed. And additional optimization process is required to make the method more effective.

A.5 Reference

1. National Institute of Justice Report, High priority criminal justice technology needs. U.S. Department of Justice Office of Justice Programs, NCJ 225375, Washington, DC 202531, 2009.

2. M.S. Bonfanti, J.D. Kinder, The influence of manufacturing processes on the identification of bullets and cartridge cases. *Science & Justice*, **39**, 3-10, (1999).

3. C. Monturo, The effect of the machining process as it relates to toolmarks on surfaces, *AFTE Journal*, **42**, 264-266, (2010).

4. J. Miller, An Introduction to the forensic examination of toolmarks, *AFTE Journal*, **33**, 233-248, (2001).

5. H. Katterwe. Fracture Matching and repetitive experiemnts: a contribution of validation. *AFTE Journal*, 37, 229-241, (2005).

6. L. Ekstrand. Virtual tool mark generation for efficient striation analysis in forensic science. M.S. Thsis, Iowa State University 2012.

7. T. Grieve. Objective analysis of toolmarks in forensic. M.S. Thesis, Iowa State University 2013.

8. I.V. Alexanndrov et al. Modeling Simulations. *Material Science Engineering*, **3**, 149-159, (1995).

9. D. Baldwin, J. Birkett, O. Facey, G. Rabey. The forensic examination and interpretation of tool marks. Wiley Blackwell & Sons, UK, 2013.

10. D. Baldwin, M. Morris, S. Bajic, Z. Zhou, M.J. Kreiser. Statistical tools for forensic analysis of toolmarks. Ames Laboratory Technical Report, 2004; IS-5160.

11. F.A. McClintock, A. Argon, Mechanical behavior of materials, Addison-Wesley Publishing Company, Reading, MA, 1966.

12. L. David. Object Recognition from Local Scale-Invariant Features. *Proceeding of the international conference on computer vision*, IEEE Computer Society Press, California, 1999.

13. L. David. Distinctive Image Features from Scale-Invariant Keypoints. *International Journal of Computer Vision*, **60**, 91-110, (2004).